UNIVERSITY OF CALIFORNIA, SAN DIEGO

An Investigation of Deformation and Fluid Flow at Subduction Zones Using Newly Developed Instrumentation and Finite Element Modeling

A dissertation submitted in partial satisfaction of the

requirements for the degree Doctor of Philosophy

in

Oceanography

by

Alison Louise LaBonte

Committee in charge:

Professor Kevin M. Brown, Chair
Professor Scott Ashford
Professor Leroy Dorman
Professor Yuri Fialko
Professor David R. Hilton

2007

The Dissertation of Alison Louise LaBonte is approved, and it is acceptable in quality and form for publication on microfilm:

_____

_____

_____

_____

_____

Chair

University of California, San Diego

2007

TABLE OF CONTENTS

LIST OF SYMBOLS

κ ..... hydraulic conductivity

γ ..... one-dimensional loading efficiency

p ..... excess pore pressure

q ..... darcy flow velocity

h ..... fracture aperature

l ..... fracture length

μ ..... dynamic viscosity of fluid

ρg ..... weight density of fluid

d ..... depth to dislocation

L ..... length of dislocation

S ..... hydrogeologic storage coefficient

c ..... hydraulic diffusivity

v ..... Poisson's ratio

E ..... Young's modulus

K ..... frame bulk modulus

K_s ..... grain bulk modulus

K_f ..... fluid bulk modulus

α ..... Biot-Willis coefficient

B ..... Skempton's coefficient

η ..... poroelastic stress coefficient

e ..... void ratio

n ..... porosity

τ ..... dimensionless time

D ..... displacement distribution

b ..... maximum displacement

G ..... shear modulus

v_u ..... undrained Poisson's ratio

l_1, l_2 ..... material layer thicknesses

θ ..... dimensionless flow rate

V_r ..... speed of propagating rupture tip

x_i ..... rupture intitiation location

LIST OF FIGURES AND TABLES

ACKNOWLEDGEMENTS

My accomplishments as a doctoral student at the Scripps Institution of Oceanography (SIO) were in a large part possible due to the assistance and guidance of a great many people. I had little fear in asking mentors, peers, friends, and even people I've never met before, for answers to a variety of odd, mostly electrical engineering, questions. For their time and patience with me, I owe a great deal of thanks.

My advisor, Kevin Brown, provided me with the room I needed to work, demonstrating his confidence in my abilities. Kevin really pulled through in the final throws of my dissertation by carefully reading and revising the scientific arguments and conclusions of my final chapters. An optimist, Kevin convinced me that my intense hours during the last months of my dissertation were well worth my extra grey hairs and bulging eyeballs. I thank him for his remarks of appraisal and belief that my work is of novel scientific importance. Thank you Yuri Fialko for acting essentially as my primary advisor through the modeling component of my dissertation. I also appreciate the support of the remainder of my committee: Dave Hilton, Scott Ashford, and Leroy Dorman. I thank Deborah Kelley and John Delaney at UW for their career advising.

My labmates, Mike Tryon and Jill Weinberger, really kept me on my feet through the whole six-year ordeal. Their sympathetic ears, and sharing of experiences in the laboratory, on research ships, and in Kevin's office, gave me the strength to continue on, and the confidence that someday I would actually finish. Mike and Jill also coached me in writing publications and proposals. Of the most importance to me though is their friendship, and I look forward to continuing BBQ's and backpacking trips with

them in the future. I also enjoyed the company and entertainment of masters student Rodrigo Coppelli during days of monotonous coil cutting and fluid sampling.

My experience would not have been the same without the love and support of friends and family. My awesome officemates, Travis Smith and Flavia Nunes were truly wonderful. Thanks for the oceanview office Travis! Great stress relieving getaways with Flavia, and a dear group of adventurous and international friends with healthy appetites, to the outdoors and exotic countries were absolutely essential. I demand we continue these adventures, i.e. Whistler! My family has consistently reassured me that I could do whatever I set out to do as I changed fields three times before finishing school (thank you Lisa and Danny Stöckli for introducing me to the thrills of geology). My family's only demand of me is that I continue to travel fun places so they can come visit me there. I owe infinite thanks to my common law partner, Bob "Beub" Day, for his unconditional love and support through my periods of hair tearing and frustration.

Lastly, congratulations to fellow Scripps Community Outreach Program for Education leaders Lisa Munger and Fernando Gonzalez: we kept SCOPE alive!

Funding has been generously provided by the Achievement Rewards for College Scientists (ARCS) Foundation-San Diego Chapter, Scripps Institution of Oceanography Graduate Department, National Science Foundation, NOAA's Undersea Research Program, and the WM Keck Foundation Grant to the University of Washington.

Chapter 2, in full, is a reprint of the publication: LaBonte, A., K. Brown, and M. Tryon (2007), Monitoring periodic and episodic flow events at Monterey Bay seeps using a new optical flow meter, *Journal of Geophysical Research*, *112*, B02105, doi:10.1029/2006JB004410.

VITA

2000	B.S. University of California, Los Angeles
2000-2001	Our World-Underwater Scholarship Society North American Scholar
2001-2007	Graduate Research Assistant. Scripps Institution of Oceanography, University of California, San Diego
2003-2007	Graduate Teaching Assistant. University of California, San Diego
2007	Ph.D., University of California, San Diego

PUBLICATIONS

LaBonte, A.L., K.M. Brown, M.D. Tryon, Monitoring periodic and episodic flow events at Monterey Bay seeps using a new optical flow meter, *Journal of Geophysical Research*, 112, B02105, doi:10.1029/2006JB004410.

D. Frye, J. Ware, M. Grund, L. Freitag, J. Collins, R. Detrick, J. Delaney, D. Kelley, M. Lilley, W. Wilcock, K. Brown and A. LaBonte, An Acoustically-Linked Moored Buoy Ocean Observatory Successfully Tested for a Year in the Northeast Pacific, *Eos Trans. AGU*, 87(22), 213, 2006.

LaBonte, A., K.M. Brown, Y. Fialko, Consecutive Flow Events and Propagating Aseismic Slip at the Costa Rica Forearc: Matching Models to Measurements*, Eos Trans. AGU*, 86(52), Fall Meet. Suppl., Abstract T13B-0459, 2005.

Reif, C., A. LaBonte, Graduate Students Unite! Building an Outreach Program From Scratch, *Eos Trans. AGU*, 86(52), Fall Meet. Suppl., Abstract ED13F-05, 2005.

LaBonte, A.L., K.M. Brown, OTIS Flow Meter for Offshore Detection of Silent Earthquakes, *Eos Trans. AGU*, 85(47), Fall Meet. Suppl., Abstract S53A-0189, 2004.

Tryon, M.D., A.L. Labonte, E. Fueri, D.R. Hilton, K.M. Brown, Toward long-term geochemical sampling of gases and deep fluids in subduction zone fore-arcs: New instrument developments, *Eos Trans. AGU*, 85(47), Fall Meet. Suppl., Abstract V13A-1440, 2004.

LaBonte, A., K.M. Brown, A High Temporal Resolution Optical Flow Meter for Measuring Aqueous Flow in Active Plate Boundary Systems, *Proceedings of the Oceans 2003 Marine Technology and Ocean Science Conference*, San Diego, CA, 2003.

ABSTRACT OF THE DISSERTATION

An Investigation of Deformation and Fluid Flow at Subduction Zones Using Newly Developed Instrumentation and Finite Element Modeling

by

Alison Louise LaBonte

Doctor of Philosophy in Oceanography

University of California, San Diego, 2007

Professor Kevin M. Brown, Chair

Detecting seafloor deformation events in the offshore convergent margin environment is of particular importance considering the significant seismic hazard at subduction zones. Efforts to gain insight into the earthquake cycle have been made at the Cascadia and Costa Rica subduction margins through recent expansions of onshore GPS and seismic networks. While these studies have given scientists the ability to quantify and locate slip events in the seismogenic zone, there is little technology available for adequately measuring offshore aseismic slip. This dissertation introduces an improved flow meter for detecting seismic and aseismic deformation in submarine environments. The value of such hydrologic measurements for quantifying the geodetics at offshore margins is verified through a finite element modeling (FEM) study in which the character of deformation in the shallow subduction zone is determined

from previously recorded hydrologic events at the Costa Rica Pacific margin. Accurately sensing aseismic events is one key to determining the stress state in subduction zones as these slow-slip events act to load or unload the seismogenic zone during the interseismic period.

One method for detecting seismic and aseismic strain events is to monitor the hydrogeologic response to strain events using fluid flow meters. Previous instrumentation, the Chemical Aqueous Transport (CAT) meter which measures flow rates through the sediment-water interface, can detect transient events at very low flow-rates, down to 0.0001 m/yr. The CAT meter performs well in low flow rate environments and can capture gradual changes in flow rate, as might be expected during ultra slow slip events. However, it cannot accurately quantify high flow rates through fractures and conduits, nor does it have the temporal resolution and accuracy required for detecting transient flow events associated with rapid deformation. The Optical Tracer Injection System (OTIS) developed for this purpose is an electronic flow meter that can measure flow rates of 0.1 to >500 m/yr at a temporal resolution of 30 minutes to 0.5 minutes, respectively. Test deployments of the OTIS at cold seeps in the transpressional Monterey Bay demonstrated the OTIS functionality over this range of flow environments. Although no deformation events were detected during these test deployments, the OTIS's temporally accurate measurements at the vigorously flowing Monterey Bay cold seep rendered valuable insight into the plumbing of the seep system.

In addition to the capability to detect transient flow events, a primary functional requirement of the OTIS was the ability to communicate and transfer data for long-term real-time monitoring deployments. Real-time data transfer from the OTIS to the

desktop was successful during a test deployment of the Nootka Observatory, an acoustically-linked moored-buoy system. A small array of CAT meters was also deployed at the Nootka transform-Cascadia subduction zone triple junction. Four anomalous flow rate events were observed across all four meters during the yearlong deployment. Although the records have low temporal accuracy, a preliminary explanation for the regional changes in flow rate is made through comparison between flow rate records and seismic records. The flow events are thought to be a result of a tectonic deformation event, possibly with an aseismic component. Further constraints are not feasible given the unknown structure of faulting near the triple junction.

In a final proof of concept study, I find that use these hydrologic instruments, which capture unique aseismic flow rate patterns, is a valuable method for extracting information about deformation events on the decollement in the offshore subduction zone margin. Transient flow events observed in the frontal prism during a 1999-2000 deployment of CAT meters on the Costa Rica Pacific margin suggest episodic slow-slip deformation events may be occurring in the shallow subduction zone. The FEM study to infer the character of the hypothetical deformation event driving flow transients verify that indeed, a shallow slow-slip event can reproduce the unique flow rate patterns observed. Along (trench) strike variability in the rupture initiation location, and bidirectional propagation, is one way to explain the opposite sign of flow rate transients observed at different along-strike distances.

The larger question stimulated by this dissertation project, is: What are the controls on fault mechanics in offshore subduction zone environments? It appears the shallow subduction zone plate interface doesn't behave solely in response to frictional

properties of the sediment lining the decollement. Shallow episodic slip at the Costa Rica Pacific margin and further north off Nicaragua, where a slow earthquake broke through the shallow 'stable-sliding' zone and resulted in a tsunami, are potentially conceived through the normally faulted incoming basement topography. Scientists should seek to map out the controls of faulting mechanics, whatever they may be, at all temporal and spatial scales in order to understand these dynamic subduction zone systems. The quest to understanding these controls, in part, requires the characterization of aseismic and seismic strain occurring over time and space. The techniques presented in this dissertation advance scientists' capability for quantifying such strains. With the new instrumentation presented here, long-term real-time observatory networks on the seafloor, and modeling for characterization of deformation events, the pieces of the subduction zone earthquake cycle puzzle may start to come together.

Chapter 1

Introduction

Subduction zones are the source of the most destructive earthquakes and they have the potential to generate devastating tsunamis through shallow thrust faulting on the offshore plate interface. For these reasons, it is important to understand the dynamics of faulting and the earthquake cycle across the entire forearc of subduction zones. Open questions in the field include: What fraction of the stress accumulated during plate convergence is released through aseismic, also referred to as slow-slip, events, as compared to seismic events? How does the resulting change in stress distribution with seismic or aseismic events affect neighboring sections of the subduction thrust fault, i.e. do aseismic events trigger seismic events or visa versa?

This dissertation is an investigation of flow rates through the sediment-water interface (SWI) in the offshore subduction zone setting and the potential deformation events that could drive these flow rates. It includes the development, testing, and proof of concept of using new and existing SWI flow meter instruments in the offshore environment and their measurements to infer deformation. The Optical Tracer Injection System (OTIS) flow meter developed for this study is sensitive to transient flow events expected to accompany strain changes resulting from dislocation in the Earth's crust. The OTIS meter is also capable of long duration deployments and real time data transfer. Through finite element modeling (FEM) of flow rate time series from different locations along the subduction zone, together with measurements from seismometers and borehole instrumentation, the rupture size, location, and duration parameters can be constrained. With the development of the new high temporal resolution OTIS flow meter and its deployment in Monterey Bay, and FEM of previous data collected at the Costa Rica subduction zone, the work in this dissertation advances the technologic and

interpretive power available for addressing the above questions of earthquake and tsunami potential in subduction zone systems.

1. Subduction Zones

As tectonic plates come together at a subduction zone convergent margin, the incoming oceanic plate dives beneath, typically, a continental plate (Figure 1). The water-saturated hydrous sediments on the incoming ocean plate are either carried down on the oceanic plate, or are scraped off and accreted to the 'accretionary wedge' (in the case of an accetionary subduction zone like Cascadia), or frontal prism (the small section of accumulated sediment in the case of a non-accretionary subduction zone like off Costa Rica and Nicaragua). Much of the interstitial water is driven from the pore spaces at a shallow depth as sediments are compacted. At greater depths, dehydration reactions, such as opal diagenisis and the clay, smectite to illite, mineral transformation, occur as subducting hydrous sediments heat up to about 100-150℃ [*Hyndman et al.*, 1993; *Harris and Wang*, 2002; *Spinelli and Saffer*, 2004]. Both elevated fluid pressures and clay transformation have been proposed to affect the potential for interface locking and faulting [*Byrne et al.*, 1988; *Vrolijk et al.*, 1991; *Hyndman et al.*, 1993; *Hyndman et al.*, 1997; *Moore and Saffer*, 2001; *Brown et al.*, 2003], and the state of stress on the subduction thrust.

Typically the subduction plate interface is split into zones based on the dynamic character of the faulting behavior (Figure 1). Theoretically unstable sliding occurs where fault material is 'velocity weakening'. In other words, most of the time, the plates are fully-coupled, or locked to one another. However, when faulting initiates, the

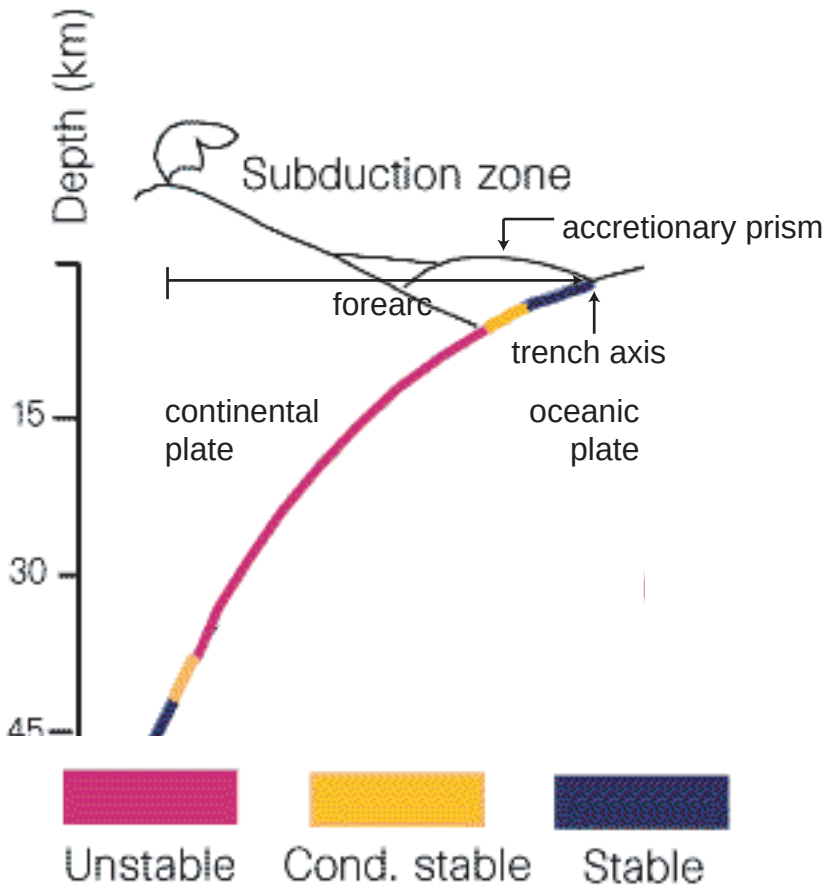

Figure 1-1. Schematic of an accretionary subduction zone. Non-accretionary subduction zones have a smaller 'frontal prism' at the trench axis rather than an accetionary prism. Zones of stability as proposed by Scholz [1998] are discretized as indicated by coloring on the 'decollement', or plate interface between the incoming oceanic plate and overriding continental plate. Unstable=locked plate interface undergoes brittle failure; Conditionally stable= stable sliding except when velocities exceed a threshhold velocity and brittle failure can occur; Stable=stable sliding at all times. Figure modified from Scholz [1998].

dynamic friction coefficient resisting sliding decreases as the velocity that the plates slide against one another increases, thus allowing for a runaway faulting event, or earthquake, to occur. The seismogenic zone is the zone over which large earthquakes rupture, and fault material is believed to be velocity weakening. Outside of this zone, strain from convergence of the plates is theoretically accommodated by stable-sliding. The cold hydrous sediments at shallower depths, and the hot ductilely deforming crust at deeper depths, are considered to be velocity strengthening.

While this simplified model explains location of initiation and extent of most earthquakes [*Scholz*, 1998; *Polet and Kanamori*, 2000], there are a significant number of inexplicable exceptions. High-resolution geodetic networks indicate existence of partially-locked zones where only a portion of strain from plate convergence accumulates, and the rest is accommodated in some unknown fashion. Large ruptures have also been observed to extend beyond the seismogenic zone into and through the 'stable-sliding' zone. These earthquakes are characteristically slower and radiate much of their energy at lower frequencies, and are particularly dangerous due to their tsunami generating capacity. It is still not clearly understood how the rupture could propagate through an otherwise velocity strengthening material. Finally, hydrologic borehole pressure and fluid flow measurements in conjunction with seismometer records at the frontal prism have recently indicated the presence of aseismic slip in the frontal prism.

These exceptions highlight that there are many remaining questions about faulting in subduction zones. The steady displacement of the partially-locked zone recorded by continuous GPS records suggests that heterogeneities in the fault surface resulting in spatial rather than temporal variation in fault mechanics and locking

behavior could produce the 'partially-locked' record. If so, are the heterogeneities topographic differences or another type, e.g. mineral or fluid pressure differences? Great tsunamis have been generated by slow earthquakes extending through the shallow section of subduction zones in non-accretionary subduction zone margins. A classic case is the great Sumatra earthquake of 2004 [*Stein and Okal*, 2007]. Is it therefore possible that aseismic, and hence undetected, slow-slip events could also initiate independently in the shallow 'stable-sliding' section of similar non-accretionary margins? Would aseismic slip in the shallow subduction zone relieve the potential of the tsunami generating capacity of a subduction zone earthquake?

These are some questions important in subduction zone systems, but before they can be addressed, a more complete record of deformation, including the offshore subduction zone is required. This study focuses on the use of hydrologic measurements that respond to deformation in the offshore, submarine, environment to help constrain deformation parameters using models of subduction zone systems.

2. Indications of Subduction Zone Processes via Hydrogeologic Measurements

Even with limited spatial coverage, offshore hydrologic measurements have contributed to the understanding of steady-state processes including chemical mass balance, overburden pressures, and long term sediment accumulation rates. Fluid pressure and flow rate measurements also respond to temporal variations, such as tidal oscillations from which material properties can be constrained, and episodic events, namely seismic and aseismic dislocation events.

2.1. Steady-State Hydrogeology

Conceptual models of fluids in subduction zones are built from hydrogeologic measurements, e.g. fluid chemistry, temperature, pressure, and flow rate, made at the seafloor and at depth in boreholes both arcward and landward of the subduction trench. Steady-state models assume there is no episodic deformation or transient fluid release in the system. They are developed to represent normal circumstances, i.e. the interseismic period between large rupture events, and are important for understanding the background fluid pressures, chemistries, and temperatures of a subduction zone system. One application of these models is to characterize the spatial variability of frictional properties at the plate interface during the interseismic period. For example, models of dewatering of the subducting sediments as a result of consolidation and dehydration reactions, constrained using empirical hydrogeologic measurements [*Moore and Vrolijk*, 1992; *Bekins et al.*, 1995; *Saffer and Screaton*, 2003], provide a more accurate map of where the plate interface behaves in a velocity-weakening manner and may undergo episodic slip in specific subduction zone systems. These background numbers are also important for global mass balance calculations.

Studies investigating steady-state fluid circulation in the crust at subduction zones use thermal and chemical analyses. For example, Cl, K, Na, Mg, Li, Sr, B contents, and temperature are measured to determine the fluid sources, the mechanism for fluid generation [e.g. *Silver et al.*, 2000; *Brown et al.*, 2001; *Mottl et al.*, 2004], and the degree of reaction with surrounding rock over the fluid's journey to the SWI [*Wheat and Mottl*, 1994; *Saffer and Screaton*, 2003]. Noble gas measurements such as 3/4He

ratio is a means by which to distinguish a deep, mantle derived, fluid source related to areas of tectonic faulting [*Kennedy et al.*, 1997; *Kulongoski et al.*, 2003].

Borehole pressure measurements constrain fluid pressures at depth and in different formations, e.g. oceanic basement, sediment prism, prism backstop, and the decollement. Additional techniques for understanding fluid pressures and movement at margins include simply observing distribution of biological indicators of seepage at the SWI [*Kulm et al.*, 1986; *Sakai et al.*, 1992; *Olu et al.*, 1997; *Henry et al.*, 2002]; indirectly determining flow rate at the SWI from thermal and chemical profiles [*Wheat and McDuff*, 1995]; and directly measuring flow rate using benthic chamber flow meters [*Carson et al.*, 1990; *Linke et al.*, 1994; *Tryon et al.*, 2001]. Methods for determining flow rate at the SWI are varied in the range of flow rates measured, and the duration and resolution of the temporal record collected [see *Linke et al.*, 1994; *Wheat and McDuff*, 1995; *Tryon et al.*, 2001; *Fisher*, 2005 and references therein]. Long-term mass balance calculations are feasible once a quantitative volume estimate can be incorporated in the steady-state models.

Ultimately, a model of fluid circulation in the crust is hypothesized using this knowledge of the source, pathway, and volume of fluids from these thermal, chemical, and flux measurements [*Vrolijk et al.*, 1991; *Silver et al.*, 2000; *Brown et al.*, 2001; *Saffer and Screaton*, 2003; *Hensen et al.*, 2004; *Mottl et al.*, 2004]. Essentially, the model of steady-state fluid circulation in subduction systems is as follows. The compacting sediments on the oceanic plate thin with subduction, and seawater from the intergranular pores is displaced. Fresh water fluids also originate during the dehydration reactions that occur as sediment temperatures increase during subduction. These

overpressured fluids preferentially escape along permeable pathways, for example, major thrusts faults and perhaps the ‘decollement’ (the detachment interface between the downgoing and overriding plate), as well as fractures in the overriding and subducting oceanic plates.

2.2. Periodic Fluid Pressure and Flow, and Material Property Determination

Loading of the crust results in a change in the pressure of the fluids filling the intergranular pores, the pore fluid pressure. This transfer of stress to the interstitial water occurs because the crustal material is compressible, and undergoes a change in volume with an applied load. There are both instantaneous and diffusive components of fluid pressure change when a saturated material is subjected to loading. The instantaneous pressure change is that of the pore fluids at the time of the applied load, before any pore fluid diffusion has occurred, or ‘undrained’ state. Diffusive pressure change occurs as over- and under-pressured fluids diffuse with time to obtain an equilibrium, or ‘drained’, state. Scientists are able to take advantage of non steady-state, periodic forcing, such as earth and ocean tides, to calculate material properties [*Bredehoeft*, 1967; *Rojstaczer and Agnew*, 1989; *Wang and Davis*, 1996]. Determination of material properties, including the compressibility of the material and hydraulic diffusivity, are key to the interpretation of hydrogeologic pressure and flow rate measurements as described in section 2.3, Episodic Fluid Pressure and Flow.

Borehole studies consist of physically extracting a core to measure material properties, spatial and temporal pressure gradients, and chemical compositions. After the borehole is sealed, records of pore pressure response to tidal forcing [*Wang and*

Davis, 1996; *Davis et al.*, 2000; *Schultz and Ruppel*, 2002] provide a means to determine formation scale material properties. Similarly, the response of flow rate and temperature measurements at the SWI to tides can constrain permeability estimates of the crust. Borehole slug, packer, and wire line tests [*Fisher et al.*, 1997; *Becker and Davis*, 2004], also reveal local material properties. Calculating material compressibility from formation pressure response requires that the porosity of the saturated material be known. This parameter is estimated through geotechnical studies performed in the laboratory on the extracted core material. Decay due to hydraulic diffusion after an episodic loading event can also give estimates of hydraulic diffusivity, and thus permeability, of the material [*Davis et al.*, 2000; *Davis et al.*, 2001; *Davis et al.*, 2004].

2.3. Episodic Fluid Pressure and Flow

Although other submarine episodic events (such as dynamic gas venting, hydrate formation, and landslides) can cause anomalous fluid pressure and flow, I only discuss the relationship between pore pressure and fluid flow to tectonic deformation events here. Spatial and temporal variations in fluid pressure in subduction zone systems are not as simple as steady-state models imply. Fluid flow rates are sensitive to both permeability and pore pressure gradients. Tectonic events, whether seismic or aseismic, can result in perturbations of flow rate through changes in either or both of these variables. Fault widening/narrowing and crack generation/sealing associated with tectonic processes are possible mechanisms for changes in permeability. Volumetric strain from episodic deformation clearly results in pore pressure changes much like periodic tidal loading affects pore pressures and flow rates. Finally, coseismic shaking,

or dynamic strain, can cause an increase in pore pressure and fluid flow via liquefaction or consolidation of near surface sediments.

While tectonic activity at plate boundaries is primarily in submerged offshore environments, a good number of onshore observations of well height, groundwater level, spring flow, stream flow, and geochemistry [see *Roeloffs*, 1996; *Toutain and Baubron*, 1999 and references therein], demonstrate both preseismic and coseismic variation associated with earthquake events. It is not always possible to decipher which mechanisms coincident with faulting and deformation are the cause of observed hydrogeologic transience. However, a few onshore studies illustrate instances where a single mechanism appears to dominate the pressure response. A study in Iceland reported striking coseismic changes of 2-16 m in heights at wells up to 20km distant from the epicenter during two magnitude 6.5 strike-slip earthquakes [*Jonsson et al.*, 2003]. Using a homogenous half space model to calculate total volumetric strain, Jonsson [2003] shows the predicted sign of pressure change coincides with coseismic rise or fall in well height.

While some onshore studies suggest the mechanism for preseismic hydrologic changes is static volumetric strain [*Linde et al.*, 1988; *Chadha et al.*, 2003; *Jonsson et al.*, 2003], several studies indicate coseismic changes in flow rate and well water level are due to dynamic strain, i.e. seismic wave induced ground motion causing liquefaction and/or consolidation [*Roeloffs*, 1998; *Manga*, 2001; *Manga et al.*, 2003; *Matsumoto and Roeloffs*, 2003; *Montgomery et al.*, 2003], or enhanced permeability [*Rojstaczer and Wolf*, 1992; *Rojstaczer et al.*, 1995]. Changes in water level in wells [*King et al.*, 1995; *Koizumi et al.*, 1996] and spring and river flow [*Sato et al.*, 2000] associated with the

1995 magnitude 6.9 Kobe earthquake are thought to be a combination of volumetric strain change and permeability enhancement as increased outflow occurred even in extensional quadrants of the modeled strain field.

Records of fluid chemistry also vary at the time of the Kobe earthquake. Ion concentrations in bottled spring water [*Tsunogai and Wakita*, 1995; *Johansen et al.*, 1996] show preseismic oscillation. Release of volatiles is a possible earthquake precursor. Measurements of radon spiked before the Kobe earthquake [*Igarashi et al.*, 1995]. He and Ar content [*Sugisaki and Sugiura*, 1985; *Areshidze et al.*, 1992; *Biagi et al.*, 2004], and $^{3}He/^{4}He$ [*Sano et al.*, 1998; *Italiano and Martinelli*, 2001; *Zmazek et al.*, 2002; *Matsumoto et al.*, 2003] records at other earthquake locations also show preseismic anomalies. Monitoring the chemical make up of fluids might help answer the question of whether flow rate variability is related to volumetric strain, dynamic strain, or permeability changes. These onland observations of episodic changes in fluid chemistry highlights the necessity of collecting and analyzing fluid chemistry in addition to collecting spatial and temporal records of flow rate.

2.3.1. Deformation and Hydrogeologic Response in the Marine Environment

In cases where measured hydrologic response at the SWI to deformation can be assumed to be a result of volumetric strain, and enough measurements are made in different locations, the size and location of the deformation can be determined through modeling. A clear example is a three-year borehole pressure study on the Juan de Fuca plate [*Davis et al.*, 2001]. Fluid pressure transients were measured in a number of boreholes extending away from the Endeavor Ridge segment of the East Pacific Rise

(EPR) during a period of seismicity on the spreading ridge. Davis et al. [2001] first rule out that the transients observed in the borehole pressure records are due to either: 1) dynamic strain related pressure changes, or 2) permeability changes, through the following reasoning. No response was detected to much larger ground displacements and accelerations expected to have occurred at the borehole monitoring sites following distant magnitude 8.8 and 8.3 earthquakes. Therefore consolidation of the formation due to shaking with wave train passage is not expected to be the cause of the hydrologic response observed during the smaller magnitude swarm events at the nearby EPR. Permeability changes are ruled out as the observed pressure response to the swarm at all sites is positive, but the background pressure states at the borehole sites vary. The sites that are superhydrostatic would have experienced a negative pore pressure response if the permeability of the formation increased with shaking, and subhydrostatic sites a positive pressure response.

The pore pressure changes in response to the magnitude 4.6 earthquake on the Endeavor segment on June 1999 [*Davis et al.*, 2001] are therefore deemed to be a result of volumetric strain. The largest pressure changes, 2-3kPa, were observed at the two boreholes closest to the epicenter, ~30 km. At the borehole site 100 km distant, a 0.2 kPa change in pressure was observed. Davis et al. [2001] use Okada's model [*Okada*, 1992] for shear and tensile dislocations in a homogeneous half-space, and material properties constrained via tidal response calculations to model the deformation event. In using Okada's model, they assume that the crust is homogeneous and the coseismic pressure response to tectonic loading is the undrained response, i.e. no pore fluid diffusion occurs during the time when stress and strains are changing. A finite element

Darcy flow model is then applied to model drainage of the fluids as pore pressures return to the equilibrium state. During this diffusion period, it is assumed there are no stress and strain changes. This uncoupled approach is common for modeling poroelastic response to seismic deformation, as the diffusive component has essentially no effect at the short seismic timescale.

Davis et al. find the rupture dimensions necessary to produce the observed changes in instantaneous fluid pressures must be much greater than that of the concurrent 4.6 earthquake. They conclude that a large portion of energy was released aseismically. This combination of empirical hydrogeologic measurements, and modeling techniques is a method of comprehending the partitioning of stress release through seismic and aseismic deformation events. Long term monitoring of such events is crucial to understanding earthquake cycles. The same techniques can be applied to subduction zone settings. Although the diffusive time constant in the young oceanic basement at this divergent margin is long (1-100 days) compared to the duration of seismic events (seconds), this uncoupled modeling approach would not accurately represent slow-slip aseismic events occurring over a period of several days. It is suspected that such events do occur in the shallow subduction zone setting (next section), therefore new fully coupled models need to be developed for these scenarios.

2.3.2. Episodic Hydrogeologic Event at a Subduction Zone

In a study at the Costa Rica margin in 2000, fourteen Chemical Aqueous Transport (CAT) flow meters with 15 km grid spacing were deployed to constrain the flow field over an approximate 50 by 70 km section of the forearc [*Brown et al.*, 2005].

The three CAT meters located on the frontal prism simultaneously recorded three flow events. With no seismic activity detected by co-deployed Ocean Bottom Seismometers (OBS), but rather a seismic noise record that correlates with fluid pulses, fluid events are hypothesized to result from a strain imposed by aseismic deformation [*Brown et al.*, 2005]. Brown et al. suggest that the dislocations would have to slowly propagate under the instruments along the decollement.

The presence of flow rate transients illustrates the potential existence of episodic events in shallow 'stable-sliding' regions of the subduction zone and is evidence that our understanding of temporal and spatial characterization of the plate interface in subduction zones is not well understood. As was done by Davis et al. [2001], estimates of the amount of seismic and aseismic dislocation that occurred from recorded hydrologic signals and modeling would improve knowledge of subduction zone faulting dynamics. However, the 2-3 week duration of these Costa Rica flow transients suggests the need for a fully-coupled model rather than commonly used uncoupled models to account for the significant amount of fluid diffusion occurring during the period of deformation.

3. Hydrogeologic Measurements

In order to understand the role aseismic events play in building and releasing strain in the earthquake cycle in subduction systems through modeling, it is first necessary to obtain good empirical measurements in the offshore environment to help constrain the model, i.e. spatial coverage and temporal resolution and accuracy. Both pore pressure gradient measurements at boreholes, and flow rate measurements with

CAT meters have successfully captured transient hydrogeologic response to tectonic events. However, to obtain the density of spatial and temporal data required, new instrument technology is desired.

New instrumentation for determining deformation should still be aimed at capturing hydrogeologic response. There are many advantages to making hydrologic measurements as opposed to measuring other proxies for deformation. For example, geodetic surveys, and interferometry, are very direct measurements of seismic and aseismic deformation, however, they are only available for the onshore environment. Offshore seismometer measurements have been made, but they are sensitive only to seismic events. Slow-slip events don't behave in a brittle, stick-slip, fashion and thus produce no seismic energy, i.e. they are aseismic. Borehole strain meter measurements, while they pick up both seismic and aseismic events, respond only to local strain, whereas the fluid pressure that is measured in the borehole is a response to the average volumetric strain over a large region of the permeable crust formation.

Numerous onshore studies and few offshore hydrogeologic measurements have demonstrated the capacity of flow rate and pressure measurements as proxies for seismic and aseismic deformation events. The aim is to increase the density and quality of offshore hydrogeologic measurements. While borehole pressure measurements [*Fisher et al.*, 1997; *Davis et al.*, 2000; *Fisher and Becker*, 2000; *Davis et al.*, 2001] give essential knowledge of material properties in addition to the pressure response to deformation events, they are difficult to execute and costly, hence limited in number. Davis et al. [2001] were fortunate to have a number of measured borehole pressure responses to the same event. Without a number of borehole records, the size and

location of deformation cannot be constrained [*Davis and Villinger*, 2006] and the assumption that the pressure response is due to volumetric strain as opposed to dynamic strain or permeability changes is difficult to verify. On the other hand, monitoring fluid flux at the seafloor as an indicator of strain is a novel cost-efficient alternative. With the ease of deploying an array of flow meters, a more spatially complete data set can be collected allowing for better constraint and interpretation of the data through modeling.

4. Previous Methods for Flow Rate Measurement at the SWI

SWI methods for flow rate determination typically concern measuring the flux of water, solute, or heat, all of which are strongly interrelated [see *Wheat and McDuff*, 1995; *Tryon et al.*, 2001; *Fisher*, 2005 and references therein]. These methods are varied in the range of flow rates measured, and the duration and resolution of the temporal record collected. Measuring profiles of temperature or chemistry with depth provides a single approximation of flow rate with each probe or core sample, respectively, that is an integrated result of flow over a rate dependent amount of time. Hence these profiling techniques are good for constraining relatively steady state conditions.

Direct measurements of fluid flow or pore pressure gradient are better suited for environments where rates may vary temporally. Absolute flow rates measured at seeps (see Section 5) can vary by several orders of magnitude. Even across an individual seep or on the same lineament of seeps, an order of magnitude difference in flow rates of adjacent seeps has been recorded. The highly heterogeneous nature of cold seeps makes absolute flow rate measurements at these seeps second to relative flow rate

measurements. The degree of accuracy of absolute measurements necessary is such that processes for the forcing fluid flows can be constrained.

Early examples of this method were unable to extend the temporal record beyond a few hours to days [*Suess*, 1985; *Carson et al.*, 1990; *Linke et al.*, 1994], making them inadequate for examining the relationship between flow and tectonics. Temporal records of flow rate up to one year in duration can be collected using an improved variation on the benthic chamber concept. The CAT meter monitors fluxes ranging from 0.0001-50 m/yr and fluid chemistry [*Tryon et al.*, 1999; *Tryon et al.*, 2002; *Brown et al.*, 2005]. The CAT meter functions to measure flux by continuously injecting a Rb-Sc tracer into the flow line, then pulling a sample into a coil after being diluted by the ambient flow of fluid [*Tryon et al.*, 2001]. While this sampling technique is ideal for resolving extremely low flow rates, the temporal resolution is low, 6-24 hours depending on the duration of the deployment.

5. SWI Flow Meter Instrument Placement: Seep or Ambient Seabed Environment

CAT meters have been deployed both at seeps in the seafloor and the ambient seabed (Figure 2). A seep is a relatively permeable pathway along which fluids from some source depth are concentrated. The flow rate measured at the seafloor seep is driven by the pressure gradient between the fluid at the source depth and the seafloor. The fluid escaping from depth is typically overpressured because it is contained in a confined aquifer. A confined aquifer is a saturated porous layer that is more permeable that the layer that caps it. At the seafloor, the lower permeability sediment layer restricts fluids from passing from the higher permeability fractured oceanic basement at depth,

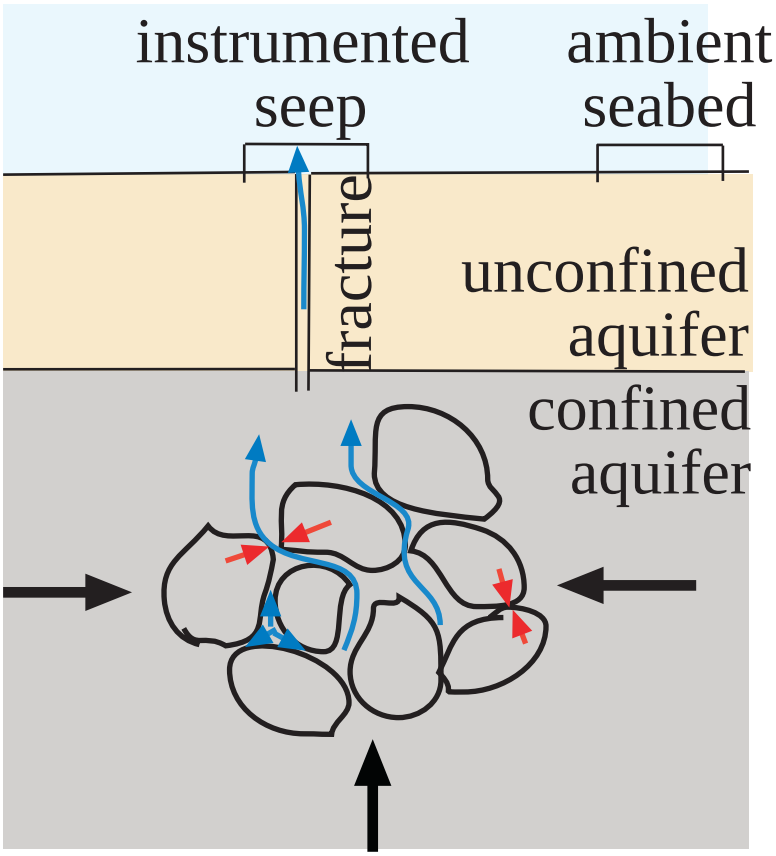

Figure 1-2. Schematic of sediment-water interface (SWI) flow meter sampling environments. A volumetric strain results in changes in the grain to grain contact pressure, as well as the interstitial pore fluid pressure. Measurements made at the ambient seabed are simply a response to the near SWI pressure gradient. Seep sites respond to pressure changes in the confined aquifer at depth. A confined aquifer is capped by a lower permeability layer, and overpressured fluids preferentially drain through focused high permeable pathways through the confining layer.

through to the seafloor. The seep conduit is analogous to a well tapping a confined aquifer in the onshore environment.

Flow rates measured at the ambient seabed environment, however, are driven by the fluid pressure gradient very near the seafloor. The change in flow rate through the SWI at the ambient seabed is analogous to the change in water table height of an unconfined aquifer. The permeability in the ambient seabed is likely much less than at a seep, so even if the driving pressure gradient is the same in the two environments, the measured flow rate through the ambient seabed environment will be significantly lower. The CAT meter is designed to measure these very low flow rates, down to 0.0001 m/yr, through the ambient seabed. It can also measure moderate flow rates at seeps, up to 50 m/yr. However, the tracer-dilution method used to determine flow rates with the CAT meter does not allow for flow rate determination at higher flow rate seeps.

Like onshore records of both an unconfined aquifer's water table height and well height or spring flow from a confined aquifer change with tectonic events, flow rate at the ambient seabed and from a seep are expected to respond to tectonic events. The expected pattern of the flow rate response measured at a seep is different from that measured at the ambient seabed. For example, deformation at depth causes deformation of the free boundary surface, the seafloor [*Okada*, 1985]. The ambient seabed measurement, responding to the near seafloor pressure gradient, is much more sensitive to this surface deformation than the seep measurement. Another difference is that the flow rate measurement from a seep tapping a confined aquifer likely has a delayed maximum some time after a tectonic event, as is observed in borehole pressure records [*Davis et al.*, 2001; *Davis et al.*, 2004], and the ambient seabed measurement does not.

The peak pressure signal arrives after the tectonic deformation event because it takes time for the pressure wave originating at the location of the rupture to diffuse laterally in the confined aquifer. This delayed peak is not observed in an unconfined aquifer [e.g. *Ge and Stover*, 2000], because the pressure anomaly isn't confined and thus decays as it diffuses away from its source. The peak pressure at any distance from the source is always the instantaneous component to the pressure change (Section 2.2).

The difference in fluid chemical concentrations measured at a seep verses the ambient seabed is also significant. The fluids focused along a seep are potentially a combination of the confined aquifer fluid source and the overlying sediment layer. Fluid chemistry measured at the ambient seabed is strictly derived from the unconfined aquifer sediment layer. A change in seep fluid chemistry in response to a tectonic event does not necessarily imply a change in processes occurring at depth. Rather, the change could be a result of a change in the ratio of confined aquifer to unconfined aquifer source contribution to the fluid mixture expelled from the seep.

5.1. Interpretation of Seep vs. Ambient Seabed Flow

Interpretation of a hydrologic excursion recorded at either the seep or ambient seabed environments first requires determination of whether the observed change in flow rate is due to a deformation event or an oceanographic effect. This entails checking the flow rate time series against the record of bottom water currents, and bottom pressure changes that potentially result from oceanographic effects, for a lack of correlation. Before designing a FEM to attempt to determine deformation parameters that could produce the hydrologic event, it is also necessary to constrain the

deformation related mechanism that results in a flow rate change, e.g. permeability changes, dynamic strain, or volumetric strain (Section 2.3.1). The FEM designed in this dissertation assumes volumetric strain is solely responsible for deformation related changes in flow rate.

When using a FEM to infer the type and size of the deformation event that generated a hydrologic transient, it is important to consider that flow rates at a seep and ambient seabed respond differently to the deformation event. It is far more convenient to interpret ambient seabed measurements because I know the length scale of the pressure gradient to which the flow rate is responding, simply the depth of the CAT meter fluid collection chamber. However, in trying to compare the flow rate from a seep to the FEM flow rate prediction, I would have to constrain the source depth of the fluid, i.e. the depth of the confined aquifer. This additional degree of freedom makes determining the magnitude of displacement one degree more difficult. Perhaps one should just rely on hydrogeologic measurements at seeps to constrain rupture location, extent, and propagation direction, and leave the magnitude constraints to borehole pressure measurements, where the depth is clearly known. Still, it might be conceivable to constrain the depth of the aquifer with accurate fluid chemistry and temperature measurements.

6. This Work

The needs outlined in this introduction that are addressed in the following three chapters are: 1) to improve offshore flow meter instrumentation allowing for high-temporal resolution and accuracy, 2) provide long-term real-time monitoring capability,

and 3) develop a fully-coupled poro-elastic model to interpret flow meter data collected at the ambient seabed environment ultimately demonstrating that SWI hydrologic data can give invaluable constraints on the geodetics of marine tectonic systems.

A new instrument, the Optical Tracer Injection System (OTIS) flow meter, was developed to detect a large range of flow rates, 0.1 to >500 m/yr, through the SWI at a high temporal resolution of 0.5-30 minutes. The OTIS is deployable in all types of margin environments, as long as the seafloor substrate is soft sediment and the instrument is placed on a moderately flowing, >0.1 m/yr, seep. It is not designed to sense changes in the low flow rate ambient seabed environment. Chapter 2 of this dissertation covers the development and testing of the OTIS meter. I also present results from the first deployment of the OTIS meter in Monterey Bay, a transpressional margin, i.e. strike-slip with a degree of convergence as well, in Chapter 2. Chapter 3 is a real time test of the OTIS meter at the Nootka-Cascadia triple junction, where the Nootka transform fault meets with the Cascadia subduction zone, off the coast of Vancouver Island, BC, CA. FEM of expected flow rates at the ambient seabed SWI for comparison with CAT meter measurements made at the ambient seabed in the Costa Rica shallow subduction zone are presented in Chapter 4.

6.1. Chapter 2

Fault and slip related fluid events are of a rapid transient nature. Test deployments of the OTIS flow meter in a range of flow rate environments demonstrate its capability to capture transient flow events. Furthermore, the accuracy of the timing in the flow rate record allows for interpretations of the geologic structure to be made

through phase analysis of the flow response to tidal forcing. In future studies that employ temporally accurate OTIS meters, a comparison between timing of transient flow events recorded on OTIS meters can help to locate deformation events. A comparison of flow rate records with seismometer records can validate if flow rate transients are indeed correlated with seismic events. This is a significant improvement upon the previous generation CAT meters.

Like the CAT meter, the OTIS has the capacity to sample fluid chemistry as well by using an osmotic pump to draw fluids into a sample coil. The mantle helium isotopic signature recorded during the test deployment in Monterey Bay confirmed our interpretation from phase analysis, that the fluid seep is connected via a highly permeable fracture to a deep fault system. With fluid chemistry and temperature records, a bound of the depth to which a fluid seep taps, 110 - 500 m, is determined. Periodic changes in flow rate are clearly a result of volumetric strain from tidal overburden pressures. The cause for observed longer-term variation in flow rate could be related to longer-term changes in aquifer pressure or permeability changes. An investigation of temperature and chemistry records may help to sort out the cause for longer-term changes. For example, it is clear that since the temperature pattern does not match the flow rate pattern in the longer-term, like it does at tidal periods, it is possible the change is not simply a change in volumetric strain and aquifer pressure. Instead, a change in the ratio of contribution from a shallow cool source to a deep warm source, perhaps due to permeability changes, could result in the longer-term changes in flow rate.

6.2. Chapter 3

The OTIS meter optically senses, and electronically logs, the concentration of an injected fluorescent rhodamine tracer from which the rate of fluids flowing through the SWI can be determined. An electronic data set has many benefits. More commonly recognized are the accurate time stamp and the ease of data processing. A study at the Nootka transform fault- Cascadia subduction zone triple junction presented in Chapter 3 illustrates the primary benefits of electronically logging flow rate data: the potential for real-time data transfer. This is an extremely important feature for studies in offshore environments where weather conditions are harsh and ship operations are costly. Flow rate transients were detected during the year-long study by CAT meters deployed at the triple junction. A comparison between flow rate records and activity recorded by onshore and offshore seismometer networks in Chapter 3, once again demonstrates the need for accurate timing of flow rate instrumentation in order to adequately determine the relationship of flow rate response and tectonic events. Furthermore, accurate focal mechanisms of local events could help validate that flow rate response is indeed due to deformation related volumetric strain.

6.3. Chapter 4

The final modeling chapter is intended to numerically prove the concept that SWI flux measurements, along with borehole pressure and offshore geodetic measurements, can be used to constrain the dynamics of plate boundaries, in particular, at the frontal prism of the Costa Rica subduction zone. The study is motivated by three flow rate events with unusual patterns observed simultaneously on three instruments at

the frontal prism of the non-accretionary Costa Rica subduction zone during a six-month period [*Brown et al.*, 2005]. The instruments were spaced along 30km of the deformation front suggesting a regionally significant process was involved. The cause of the events and associated seismic noise was hypothesized to be propagating aseismic creep events in the shallow subduction thrust. The unusual flow rate pattern for each of the three flow events consisted of closely spaced doublets in accelerated inflow and outflow spaced over approximately three weeks.

The fully-coupled FEM investigation in Chapter 4 predicts that remarkably similar doublets in flow transience are generated by a propagating dislocation along the decollement. These are novel and significant results, and give a first quantitative look at the types and sizes of deformation that could be occurring to generate the flow rate patterns observed by offshore hydrologic instrumentation monitoring in the nominally 'stable-sliding' sections of the subduction zone. Through future studies to deploy newly developed flow meters with seismometers, and the use of modeling to interpret hydrogeologic responses to deformation events, I hope to further understanding of the distribution and character of stress dissipation in the earthquake cycle, and the role that potential episodic deformation in 'stable-sliding' sections of the subduction zone may have in earthquake nucleation and tsunami generation.

References

Areshidze, G., F. Bella, P.F. Biagi, M. Caputo, V. Chkuaseli, G. Dellamonica, A. Ermini, P. Mandjgaladze, G. Melikadze, V. Sgrigna, L. Slavina, and D. Zilpimiani (1992), Anomalies in Geophysical and Geochemical Parameters Revealed on the Occasion of the Paravani (M = 5.6) and Spitak (M = 6.9) Earthquakes (Caucasus), *Tectonophysics*, *202*, 23-41.

Becker, K., and E.E. Davis (2004), In situ determinations of the permeability of the igneous oceanic crust, in *Hydrogeology of the Oceanic Lithosphere*, edited by E.E. Davis, and H. Elderfield, pp. 189-224, University Press, Cambridge.

Bekins, B.A., A.M. McCaffrey, and S.J. Dreiss (1995), Episodic and constant flow models for the origin of low-chloride waters in a modern accretionary complex, *Water Resour Res*, *31*, 3205-3215.

Biagi, P.F., R. Piccolo, A. Minafra, T. Maggipinto, L. Castellana, O. Molchanov, A. Ermini, V. Capozzi, G. Perna, Y.M. Khatkevich, and E.I. Gordeev (2004), Retrospective analysis for detecting seismic precursors in groundwater argon content, *Natural Hazards and Earth System Sciences*, *4*, 9-15.

Bredehoeft, J.D. (1967), Response of Well-Aquifer Systems to Earth Tides, *Journal of Geophysical Research*, *72*, 3076-3087.

Brown, K.M., A. Kopf, M.B. Underwook, and J.L. Weinberger (2003), Compositional and fluid pressure controls on the state of stress on the Nankai subduction thrust: A weak plate boundary, *Earth and Planetary Science Letters*, *214*, 589-603.

Brown, K.M., D.M. Saffer, and B.A. Bekins (2001), Smectite diagenesis, pore-water freshening, and fluid flow at the toe of the Nankai wedge, *Earth and Planetary Science Letters*, *194*, 97-109.

Brown, K.M., M.D. Tryon, H.R. DeShon, L.M. Dorman, and S.Y. Schwartz (2005), Correlated transient fluid pulsing and seismic tremor in the Costa Rica subduction zone, *Earth and Planetary Science Letters*, *238*, 189-203.

Byrne, D.E., D.M. Davis, and L.R. Sykes (1988), Loci and Maximum Size of Thrust Earthquakes and the Mechanics of the Shallow Region of Subduction Zones, *Tectonics*, *7*, 833-857.

Carson, B., E. Suess, and J.C. Strasser (1990), Fluid-Flow and Mass Flux Determinations at Vent Sites on the Cascadia Margin Accretionary Prism, *Journal of Geophysical Research-Solid Earth and Planets*, *95*, 8891-8897.

Chadha, R.K., A.P. Pandey, and H.J. Kuempel (2003), Search for earthquake precursors in well water levels in a localized seismically active area of Reservoir Triggered Earthquakes in India, *Geophysical Research Letters*, *30*, 1416, doi:10.1029/2002GL016694.

Davis, E., K. Becker, R. Dziak, J. Cassidy, K. Wang, and M. Lilley (2004), Hydrological response to a seafloor spreading episode on the Juan de Fuca ridge, *Nature*, *430*, 335-338.

Davis, E.E., and H.W. Villinger (2006), Transient formation fluid pressures and temperatures in the Costa Rica forearc prism and subducting oceanic basement: CORK monitoring at ODP Sites 1253 and 1255, *Earth and Planetary Science Letters*, *245*, 232-244.

Davis, E.E., K. Wang, K. Becker, and R.E. Thomson (2000), Formation-scale hydraulic and mechanical properties of oceanic crust inferred from pore pressure response to periodic seafloor loading, *Journal of Geophysical Research-Solid Earth*, *105*, 13423-13435.

Davis, E.E., K. Wang, R.E. Thomson, K. Becker, and J.F. Cassidy (2001), An episode of seafloor spreading and associated plate deformation inferred from crustal fluid pressure transients, *Journal of Geophysical Research-Solid Earth*, *106*, 21953-21963.

Fisher, A.T. (2005), Marine hydrogeology: recent accomplishments and future opportunities, *Hydrogeology Journal*, *13*, 69-97.

Fisher, A.T., and K. Becker (2000), Channelized fluid flow in oceanic crust reconciles heat-flow and permeability data, *Nature*, *403*, 71-74.

Fisher, A.T., K. Becker, and E.E. Davis (1997), The permeability of young oceanic crust east of Juan de Fuca Ridge determined using borehole thermal measurements, *Geophysical Research Letters*, *24*, 1311-1314.

Ge, S.M., and S.C. Stover (2000), Hydrodynamic response to strike- and dip-slip faulting in a half-space, *Journal of Geophysical Research-Solid Earth*, *105*, 25513-25524.

Harris, R.N., and K. Wang (2002), Thermal models of the middle America trench at the Nicoya Peninsula, Costa Rica, *Geophysical Research Letters*, *29*.

Henry, P., S. Lallemant, K. Nakamura, U. Tsunogai, S. Mazzotti, and K. Kobayashi (2002), Surface expression of fluid venting at the toe of the Nankai wedge and implications for flow paths, *Marine Geology*, *187*, 119-143.

Hensen, C., K. Wallmann, M. Schmidt, C.R. Ranero, and E. Suess (2004), Fluid expulsion related to mud extrusion off Costa Rica - A window to the subducting slab, *Geology*, *32*, 201-204.

Hyndman, R.D., K. Wang, T. Yuan, and G.D. Spence (1993), Tectonic Sediment Thickening, Fluid Expulsion, and the Thermal Regime of Subduction Zone Accretionary Prisms - the Cascadia Margin Off Vancouver-Island, *Journal of Geophysical Research-Solid Earth*, *98*, 21865-21876.

Hyndman, R.D., M. Yamano, and D.A. Oleskevich (1997), The seismogenic zone of subduction thrust faults, *Island Arc*, *6*, 244-260.

Igarashi, G., S. Saeki, N. Takahata, K. Sumikawa, S. Tasaka, Y. Sasaki, M. Takahashi, and Y. Sano (1995), Groundwater Radon Anomaly before the Kobe Earthquake in Japan, *Science*, *269*, 60-61.

Italiano, F., and G. Martinelli (2001), Anomalies of mantle-derived helium during the 1997-1998 seismic swarm of Umbria-Marche, Italy, *Geophysical Research Letters*, *28*, 839-842.

Johansen, A., D. Sornette, H. Wakita, U. Tsunogai, W.I. Newman, and H. Saleur (1996), Discrete scaling in earthquake precursory phenomena: Evidence in the Kobe earthquake, Japan, *Journal De Physique I*, *6*, 1391-1402.

Jonsson, S., P. Segall, R. Pedersen, and G. Bjornsson (2003), Post-earthquake ground movements correlated to pore-pressure transients, *Nature*, *424*, 179-183.

Kennedy, B.M., Y.K. Kharaka, W.C. Evans, A. Ellwood, D.J. DePaolo, J. Thordsen, G. Ambats, and R.H. Mariner (1997), Mantle fluids in the San Andreas fault system, California, *Science*, *278*, 1278-1281.

King, C.Y., N. Koizumi, and Y. Kitagawa (1995), Hydrogeochemical Anomalies and the 1995 Kobe Earthquake, *Science*, *269*, 38-39.

Koizumi, N., Y. Kano, Y. Kitagawa, T. Sato, M. Takahashi, S. Nishimura, and R. Nishida (1996), Groundwater anomalies associated with the 1995 Hyogo-ken Nanbu earthquake, *Journal of Physics of the Earth*, *44*, 373-380.

Kulm, L.D., E. Suess, J.C. Moore, B. Carson, B.T. Lewis, S.D. Ritger, D.C. Kadko, T.M. Thornburg, R.W. Embley, W.D. Rugh, G.J. Massoth, M.G. Langseth, G.R. Cochrane, and R.L. Scamman (1986), Oregon Subduction Zone - Venting, Fauna, and Carbonates, *Science*, *231*, 561-566.

Kulongoski, J.T., D.R. Hilton, and J.A. Izbicki (2003), Helium isotope studies in the Mojave Desert, California: implications for groundwater chronology and regional seismicity, *Chemical Geology*, *202*, 95-113.

Linde, A.T., K. Suyehiro, S. Miura, I.S. Sacks, and A. Takagi (1988), Episodic Aseismic Earthquake Precursors, *Nature*, *334*, 513-515.

Linke, P., E. Suess, M. Torres, V. Martens, W.D. Rugh, W. Ziebis, and L.D. Kulm (1994), In-Situ Measurement of Fluid-Flow from Cold Seeps at Active Continental Margins, *Deep-Sea Research Part I-Oceanographic Research Papers*, *41*, 721-739.

Manga, M. (2001), Origin of postseismic streamflow changes inferred from baseflow recession and magnitude-distance relations, *Geophysical Research Letters*, *28*, 2133-2136.

Manga, M., E.E. Brodsky, and M. Boone (2003), Response of streamflow to multiple earthquakes, *Geophysical Research Letters*, *30*, 1214, doi:10.1029/2002GL016618.

Matsumoto, N., and E.A. Roeloffs (2003), Hydrological response to earthquakes in the Haibara well, central Japan - II. Possible mechanism inferred from time-varying hydraulic properties, *Geophysical Journal International*, *155*, 899-913.

Matsumoto, T., T. Kawabata, J. Matsuda, K. Yamamoto, and K. Mimura (2003), He-3/He-4 ratios in well gases in the Kinki district, SW Japan: surface appearance of slab-derived fluids in a non-volcanic area in Kii Peninsula, *Earth and Planetary Science Letters*, *216*, 221-230.

Montgomery, D.R., H.M. Greenberg, and D.T. Smith (2003), Streamflow response to the Nisqually earthquake, *Earth and Planetary Science Letters*, *209*, 19-28.

Moore, J.C., and D. Saffer (2001), Updip limit of the seismogenic zone beneath the accretionary prism of southwest Japan: An effect of diagenetic to low-grade metamorphic processes and increasing effective stress, *Geology*, *29*, 183-186.

Moore, J.C., and P. Vrolijk (1992), Fluids in Accretionary Prisms, *Reviews of Geophysics*, *30*, 113-135.

Mottl, M.J., C.G. Wheat, P. Fryer, J. Gharib, and J.B. Martin (2004), Chemistry of springs across the Mariana forearc shows progressive devolatilization of the subducting plate, *Geochimica Et Cosmochimica Acta*, *68*, 4915-4933.

Okada, Y. (1985), Surface Deformation Due to Shear and Tensile Faults in a Half-Space, *Bulletin of the Seismological Society of America*, *75*, 1135-1154.

Okada, Y. (1992), Internal Deformation Due to Shear and Tensile Faults in a Half-Space, *Bulletin of the Seismological Society of America*, *82*, 1018-1040.

Olu, K., S. Lance, M. Sibuet, P. Henry, A. FialaMedioni, and A. Dinet (1997), Cold seep communities as indicators of fluid expulsion patterns through mud volcanoes seaward of the Barbados accretionary prism, *Deep-Sea Research Part I-Oceanographic Research Papers*, *44*, 811-&.

Polet, J., and H. Kanamori (2000), Shallow subduction zone earthquakes and their tsunamigenic potential, *Geophysical Journal International*, *142*, 684-702.

Roeloffs, E. (1996), Poroelastic techniques in the study of earthquake-related hydrologic phenomena, in *Advances in Geophysics, Vol 37*, *37*, pp. 135-195.

Roeloffs, E.A. (1998), Persistent water level changes in a well near Parkfield, California, due to local and distant earthquakes, *Journal of Geophysical Research-Solid Earth*, *103*, 869-889.

Rojstaczer, S., and D.C. Agnew (1989), The Influence of Formation Material Properties on the Response of Water Levels in Wells to Earth Tides and Atmospheric Loading, *Journal of Geophysical Research-Solid Earth and Planets*, *94*, 12403-12411.

Rojstaczer, S., and S. Wolf (1992), Permeability Changes Associated with Large Earthquakes - an Example from Loma-Prieta, California, *Geology*, *20*, 211-214.

Rojstaczer, S., S. Wolf, and R. Michel (1995), Permeability Enhancement in the Shallow Crust as a Cause of Earthquake-Induced Hydrological Changes, *Nature*, *373*, 237-239.

Saffer, D.M., and E.J. Screaton (2003), Fluid flow at the toe of convergent margins: interpretation of sharp pore-water geochemical gradients, *Earth and Planetary Science Letters*, *213*, 261-270.

Sakai, H., T. Gamo, Y. Ogawa, and J. Boulegue (1992), Stable Isotopic-Ratios and Origins of the Carbonates Associated with Cold Seepage at the Eastern Nankai Trough, *Earth and Planetary Science Letters*, *109*, 391-404.

Sano, Y., N. Takahata, G. Igarashi, N. Koizumi, and N.C. Sturchio (1998), Helium degassing related to the Kobe earthquake, *Chemical Geology*, *150*, 171-179.

Sato, T., R. Sakai, K. Furuya, and T. Kodama (2000), Coseismic spring flow changes associated with the 1995 Kobe earthquake, *Geophysical Research Letters*, *27*, 1219-1222.

Scholz, C.H. (1998), Earthquakes and friction laws, *Nature*, *391*, 37-42.

Schultz, G., and C. Ruppel (2002), Constraints on hydraulic parameters and implications for groundwater flux across the upland-estuary interface, *Journal of Hydrology*, *260*, 255-269.

Silver, E., M. Kastner, A. Fisher, J. Morris, K. McIntosh, and D. Saffer (2000), Fluid flow paths in the Middle America Trench and Costa Rica margin, *Geology*, *28*, 679-682.

Spinelli, G.A., and D.M. Saffer (2004), Along-strike variations in underthrust sediment dewatering on the Nicoya margin, Costa Rica related to the updip limit of seismicity, *Geophysical Research Letters*, *31*.

Stein, S., and E.A. Okal (2007), Ultralong period seismic study of the December 2004 Indian Ocean earthquake and implications for regional tectonics and the subduction process, *Bulletin of the Seismological Society of America*, *97*, S279-S295.

Suess, E. (1985), Biological communities at vent sites along the subduction zone off Oregon, Bulletin of the Biological Society of Washington, in *Hydrothermal vents of the eastern Pacific : an overview*, edited by M.L. Jones, *6*, pp. 475-484, Vienna, Va.

Sugisaki, R., and T. Sugiura (1985), Geochemical Indicator of Tectonic Stress Resulting in an Earthquake in Central Japan, 1984, *Science*, *229*, 1261-1262.

Toutain, J.P., and J.C. Baubron (1999), Gas geochemistry and seismotectonics: a review, *Tectonophysics*, *304*, 1-27.

Tryon, M., K. Brown, L.R. Dorman, and A. Sauter (2001), A new benthic aqueous flux meter for very low to moderate discharge rates, *Deep-Sea Research Part I-Oceanographic Research Papers*, *48*, 2121-2146.

Tryon, M.D., K.M. Brown, and M.E. Torres (2002), Fluid and chemical flux in and out of sediments hosting methane hydrate deposits on Hydrate Ridge, OR, II: Hydrological processes, *Earth and Planetary Science Letters*, *201*, 541-557.

Tryon, M.D., K.M. Brown, M.E. Torres, A.M. Trehu, J. McManus, and R.W. Collier (1999), Measurements of transience and downward fluid flow near episodic methane gas vents, Hydrate Ridge, Cascadia, *Geology*, *27*, 1075-1078.

Tsunogai, U., and H. Wakita (1995), Precursory Chemical-Changes in-Ground Water - Kobe Earthquake, Japan, *Science*, *269*, 61-63.

Vrolijk, P., A. Fisher, and J. Gieskes (1991), Geochemical and Geothermal Evidence for Fluid Migration in the Barbados Accretionary Prism (Odp Leg 110), *Geophysical Research Letters*, *18*, 947-950.

Wang, K.L., and E.E. Davis (1996), Theory for the propagation of tidally induced pore pressure variations in layered subseafloor formations, *Journal of Geophysical Research-Solid Earth*, *101*, 11483-11495.

Wheat, C.G., and R.E. McDuff (1995), Mapping the Fluid-Flow of the Mariana Mounds Ridge Flank Hydrothermal System - Pore-Water Chemical Tracers, *Journal of Geophysical Research-Solid Earth*, *100*, 8115-8131.

Wheat, C.G., and M.J. Mottl (1994), Hydrothermal Circulation, Juan-De-Fuca Ridge Eastern Flank - Factors Controlling Basement Water Composition, *Journal of Geophysical Research-Solid Earth*, *99*, 3067-3080.

Zmazek, B., F. Italiano, M. Zivcic, J. Vaupotic, I. Kobal, and G. Martinelli (2002), Geochemical monitoring of thermal waters in Slovenia: relationships to seismic activity, *Applied Radiation and Isotopes*, *57*, 919-930.

Chapter 2

Monitoring periodic and episodic flow events at Monterey Bay seeps using a new optical flow meter

Abstract

To enable testing of the hypothesis that fluid flow from cold seeps responds to episodic tectonic events, we have developed a flow meter with a temporal resolution on the order of minutes. The Optical Tracer Injection System (OTIS) measures flow rates through the sediment-water interface (SWI) of 0.1 to >500 m/yr ± 10%, samples fluid for post-recovery chemical analysis, and is adaptable for use as a long-term real-time monitoring station. Laboratory and in situ testing demonstrate that the instrument meets temporal accuracy and resolution requirements necessary to detect transient flow events. In a deployment at an active seep site in Monterey Bay, the OTIS measured flow rates with tidal period variability. Time series analysis indicates flow rate and tide height records are in phase. This flow rate response to tides, together with seep fluid temperatures measured at the SWI of greater than 9°C, suggests the seep is connected via a highly permeable fracture or other conduit to an overpressured aquifer at a depth of at least 110 m. We infer the hydrogeology of this well-like system is further complicated by additional fluid sources since: $^{3}He/^{4}He$ ratios are elevated, and there is a lack of correlation between flow rate and temperature records at frequencies lower than tidal frequencies. This short-duration deployment demonstrates the OTIS's potential to capture flow and chemistry transients associated with earthquakes and creep in the offshore environment.

1. Introduction

Subseafloor hydrogeologic systems offer a means to understand a wide variety of physical, chemical, and thermal processes in the Earth's crust. Studies of flow rate,

pore pressure, fluid chemistry, and temperature, particularly when extended through modeling studies, have contributed to our understanding of these crustal processes at margins and plate boundaries [e.g. *Vrolijk et al.*, 1991; *Wheat and McDuff*, 1995; *Bekins et al.*, 1995; *Saffer and Screaton*, 2003; *Jupp and Schultz*, 2004]. Hydrologic studies have primarily contributed to our understanding of long-term, relatively steady-state processes including chemical mass balance, geopressure production and relief, and lithospheric cooling rates [e.g. *Han and Suess*, 1989; *Davis et al.*, 1992; *Moore and Vrolijk*, 1992; *Linke et al.*, 1994; *Silver et al.*, 2000; *Brown et al.*, 2001]. Seafloor hydrologic systems also respond to short period variations such as tidal oscillations and waves, and episodic events such as tsunamis, gas discharge, and seismic and aseismic strain [e.g *Wang and Davis*, 1996; *Schultz et. al*., 1996; *Davis et al.*, 2001; *Tryon et al.*, 2002; *Tivey et. al.*, 2002; *Ge and Screaton*, 2005; *Brown et al.*, 2005]. These processes affect stress, and stress can change permeability, pore pressure, and fluid flow rate because the crust is compliant and deforms under pressure.

In order to establish the relationship between transients in fluid flow and tectonic events recorded via seismic and/or GPS stations, a high level of temporal accuracy and resolution is desired at the flow-measuring device. This desire led to the development of the Optical Tracer Injection System (OTIS), a high-resolution electronic flow meter for measuring flow rate across the sediment-water interface (SWI) while collecting fluids for later shore-based chemical analysis. The OTIS is capable of logging fluid flow rates, and relaying the data in real time. This instrument will help to constrain models of, and further our understanding of, the tectono-hydrologic system at

convergent plate margins where the earthquake cycle and hydrologic system are intimately related.

The study of hydrologic phenomena related to tectonic activity is an active area of research. For example, well height, groundwater level, spring flow, stream flow [see *Roeloffs*, 1996 and references therein], and fluid geochemistry [see *Toutain and Baubron*, 1999 and references therein] demonstrate both preseismic and coseismic variation associated with earthquake events. A study in Iceland reported striking coseismic changes of 2 to 16 m in well heights within a 20 km distance from the epicenter during two magnitude 6.5 strike-slip earthquakes [*Jonsson et al.*, 2003]. Additional onshore studies suggest the mechanism for coseismic [*Wakita*, 1975; *Muir-Wood and King*, 1993] and preseismic [*Linde et al.*, 1988; *Chadha et al.*, 2003] hydrologic change is static volumetric strain. However, there are several studies indicating that coseismic changes in flow rate and well height are due to dynamic strain, i.e. seismic wave induced ground motion causing liquefaction and/or consolidation [*Roeloffs*, 1998; *Manga et al.*, 2003; *Montgomery et al.*, 2003], or enhanced permeability [*Rojstaczer and Wolf*, 1992]. Changes in well height [*King et al.*, 1995], spring, and river flow [*Sato et al.*, 2000] associated with the 1995 magnitude 6.9 Kobe earthquake are thought to be a combination of volumetric strain change and permeability enhancement as increased outflow occurred even in extensional quadrants of the modeled strain field.

Measurements of temperature [e.g. *Langseth and Silver*, 1996; *Johnson et al.*, 2000; *Pruis and Johnson*, 2004; *Jupp and Schultz*, 2004], major ion composition, isotopic ratios, trace elements and gas content aid in determination of the fluid sources

and mechanisms for fluid generation [*Vrolijk et al.*, 1991; *Bekins et al.*, 1995; *Silver et al.*, 2000; *Brown et al.*, 2001; *Saffer and Screaton*, 2003; *Mottl et al.*, 2004], e.g. measurement of $^{3}He/^{4}He$ ratios is a means by which to distinguish a deep, mantle-derived fluid source [*Kennedy et al.*, 1997; *Kulongoski et al.*, 2003]. Records of temperature [*Davis and Villinger*, 2006] and fluid chemistry also change during earthquake events. Preseismic anomalies in fluid chemistry associated with earthquakes include increases in He and Ar content [*Sugisaki and Sugiura*, 1985] and $^{3}He/^{4}He$ [*Sano et al.*, 1998; *Italiano and Martinelli*, 2001]. Monitoring the chemical composition of fluids can help to constrain whether changes in flow rate are related to dynamic strain or permeability changes [*Rojstaczer and Wolf*, 1992; *Tsunogai and Wakita*, 1995; *Sano et al.*, 1998; *Toutain and Baubron*, 1999; *Italiano and Martinelli*, 2001].

Of the limited number of fluid studies with adequate temporal resolution performed in the submarine environment, a few record evidence of coseismic or aseismic changes in pore pressures and flow rates [*Johnson et al.*, 2000; *Davis et al.*, 2001; *Brown et al.*, 2005; *Davis et al.*, 2006; *Davis and Villinger*, 2006]. In a three-year borehole study at the Juan de Fuca ridge, flank pressure changes of 2 to 3 kPa were recorded at two boreholes about 30 km from a magnitude 4.6 earthquake [*Davis et al.*, 2001]. In a study at the Costa Rica Pacific margin, three flow meters located in the out-of-sequence thrust zone simultaneously recorded three separate flow events during the six-month deployment [*Brown et al.*, 2005; *LaBonte et al.*, 2005]. Because no seismic activity, but rather a tremor-like noise was concurrent with the flow pulses, the hypothesized source of flow events is aseismic deformation.

We present the results of three test deployments of the OTIS: one at the Scripps pier in La Jolla, CA, where waves force high frequency fluctuations in flow rate; and two at cold seeps in Monterey Bay, which is a transpressional tectonic regime [*DeMets*, 1990] where tidal forcing overprints moderate to high background flow rates.

2. Instrumentation

2.1 Functional Requirements

Our primary motivation for a new fluid flow meter is to measure the response of hydrologic systems to tectonic deformation. A 90% precision in flow rate measurement, and a temporal accuracy and resolution of minutes to tens of minutes, is required for detecting relative changes in the hydrologic system. Absolute flow rate determination is of secondary importance, especially since flow rates at adjacent seep sites can vary by several orders of magnitude [*Tryon et. al.,* 2002]. We aim to measure absolute flow rates of centimeters to hundreds of meters per year, the range of values observed in cold seep environments, with an order of magnitude accuracy. Other functional requirements include: suitability for deployments of at least one year in duration; digital data collection to allow for ease of data transfer and potential for real-time monitoring; time-series fluid sampling; suitability of deployment up to 6000 m deep by a remotely operated vehicle (ROV) or manned submersible; and cost efficiency.

2.2 Design

Based on the Chemical and Aqueous Transport (CAT) meter design [*Tryon et. al.*, 2001], the OTIS measures fluid flux at the seafloor by channeling the flow from an

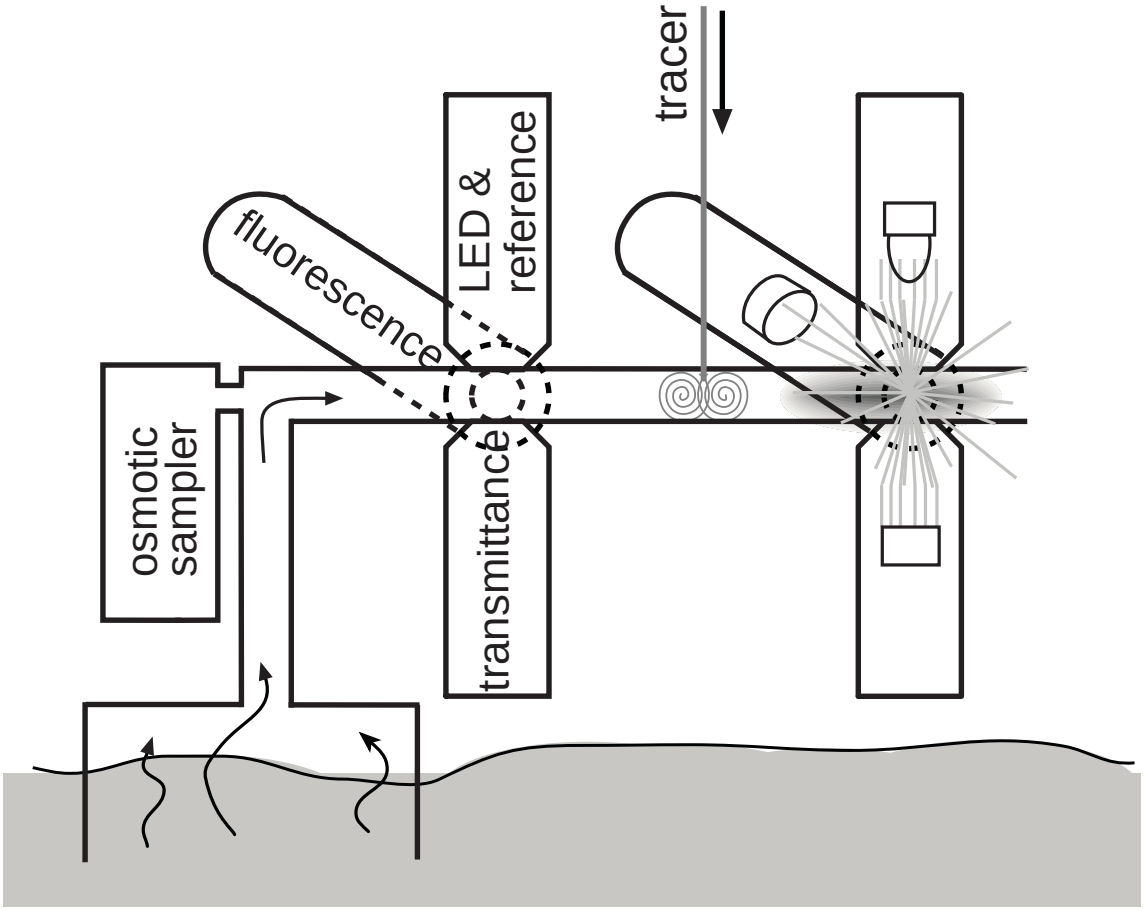

Figure 2-1. Schematic of the Optical Tracer Injection System. The external chamber placed on sedimented seafloor focuses flow through an outlet tube. Fluorescent rhodamine tracer is injected into the flow detection cell and travels with the velocity of seep fluids past either detection station. At the detection stations, an LED shines through the flow detection cell and photodiodes record transmitted light, fluorescence, and LED intensity for reference.

external collection chamber, which is sealed to the sediment surface, through the instrument via an outlet tube (Figure 1). The OTIS uses the osmotic pump from the CAT meter design to collect a time-series of seep fluid from the outlet tubing for later chemical analysis. However, an outlet tubing diameter twice that of the CAT meter is used to minimize backpressure and allow fluids to flow through the instrument at higher flow rates associated with high permeability sediments. The OTIS meter also differs in its method for flow rate determination by using an electronic “time of flight” method to meet temporal resolution requirements. A pulse of fluorescent rhodamine dye tracer is injected into the outlet tubing. The pulse of tracer travels with the velocity of the ambient flow through the outlet tube. Because the collection area is approximately 650 times greater than the inner diameter (ID) of the outlet tube the fluid velocity through the OTIS flow meter is approximately 650 times greater than the in situ flow rate. Optical electronics are used to sample transmittance and fluorescence through the outlet tubing at “detection stations” located both upstream and downstream of the injection to determine the direction and rate of flow (Figure 1). A trough in the transmittance signal and peak in the fluorescence signal mark the passing of the injected tracer pulse. For each pulse, a flow rate measurement can be calculated from the time of arrival of the tracer pulse.

The external chamber is a 28.5 cm ID cylinder 7.6 cm high, from 1/8” thick PVC sheet welded to a 3/4” thick PVC disk cap. The fine grain silts and clays create a seal with the chamber wall when inserted to its 7.6 cm height. Fluids are allowed passage out of the chamber and into the outlet tubing through a 3/4” NPT port in the cap. The outlet tubing is comprised of two sections of three meter length, 3/8” ID,

polyurethane tubing, and the “flow detection cell” in-between. The three meter long hose connecting the chamber to the flow detection cell mounted in the OTIS frame allows for maneuverability in placing the chamber as well as adequate distance from possible pressure changes associated with bottom currents flowing around the instrument frame. The flow detection cell is a 15.2 cm length of borosilicate glass of fused 1/4” ID cylindrical and 1 cm by 1 cm internal area square sections. The square glass sections allow the detection stations to be mounted flush with the glass for greater sensitivity. The fluid sample coil, 3/32” ID polypropylene tubing, branches from the outlet tube at a ‘T’ joint between the chamber and the flow detection cell. In kind with the tubing selection, material type for the tube fittings was chosen in order to not contaminate the chemistry of the fluid samples.

Green LEDs, and 565 nm and 600 nm photodiodes, were used to measure transmittance and fluorescence respectively. These optical electronics and in-line convex lenses were adjusted in the design of the detection stations to optimize photodiode sensitivity to tracer concentration. Transmittance measurements were found to have a better signal-to-noise ratio than fluorescence measurements. To save power and disk space fluorescence photodiodes were later eliminated from the OTIS design. We will hereafter discuss only the transmittance pulse shape.

Figure 2 (inset) graphically displays the digital signal, the recorded transmittance time-series, of the arrival of a pulse of tracer at a detection station sometime after injection of the pulse. Design of the flow detection cell dimensions, method of injection of the pulse of tracer, and tracer concentration demanded that within the flow rate detection range specified in the functional requirements: 1) the

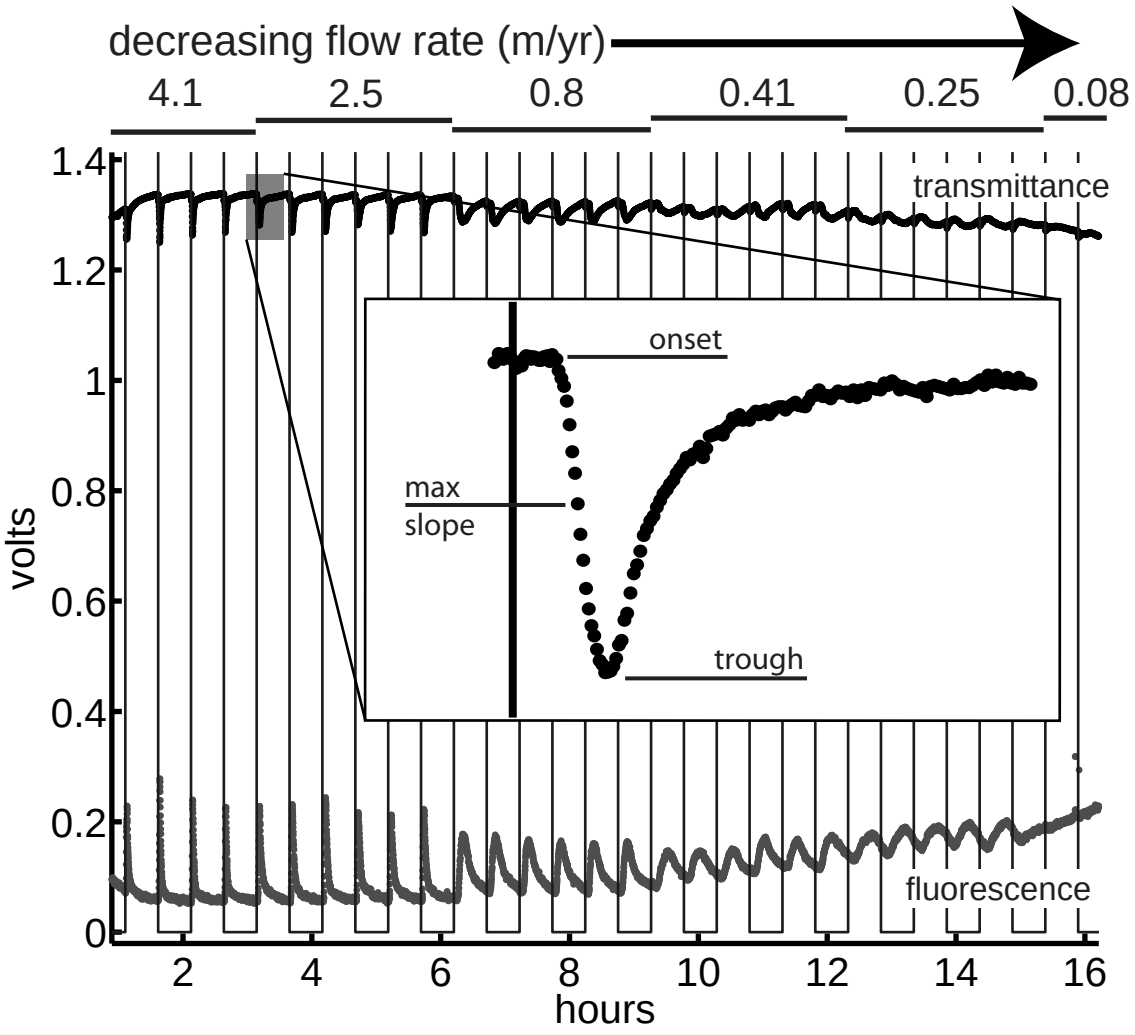

Figure 2-2. Time series of amplified fluorescence (grey) and transmittance (black) photodiode output for pump-driven, decreasing, flow rates. Vertical lines indicate the tracer pulse injections every 30 minutes. A trough in transmittance and spike in fluorescence signify the arrival of the tracer pulse at the detection station. Inset: Exploded view of a single pulse in the transmittance record. The three potential markers of tracer pulse arrival are labeled.

resulting digital signal has a pulse shape, 2) the pulse shape is distinguishable from adjacent pulses, and 3) the delay before pulse detection is repeatable for any given flow rate. We tested injecting pulses of tracer with density matching seawater density, of concentrations of 5000 ppb and 250,000 ppb, at different speeds, through micro-bore tubing and a linear slot, into a continuous square section of clear plastic tubing and glass flow cells blown with varying sizes of fused square and cylindrical sections. The optimal pulse shape resulted from a rapid 0.3 second injection of a 50 μL pulse of 5000 ppb tracer, through a section of micro-bore tubing, directly into the center cylindrical section of the glass flow detection cell between square glass sections for optical sensing 2.9 cm distant from the injection location.

In a final test of this design, we observed that the physical shape and the digital representation of the tracer pulse differ with flow rate (Figure 2). In high flow regimes, the tracer injected remains intact and passes by the detection station as a tear drop. At the front end a sharp decrease in transmittance corresponds to a high concentration gradient, and after a sharp trough, the pulse signal fades as the tail of tracer pulse clears the detection station (Figure 2). As flow rate slows, the tracer pulse arrives later, and is more spread out with a broader trough. The difference in pulse shape allows flow rates to be recorded at higher temporal resolution in fast flow environments because when the tracer pulse clears from the flow detection cell quickly, injections can be made more frequently without the worry of overlapping tracer pulses and confusing trough signals.

The resolution and accuracy of the OTIS meter's temporal record, and the digitization and storage of the optical electronics signals, are achieved through the software design of a Persistor CF1 computer with a R212 RecipeCard, a baseboard with

a 12-bit analog to digital converter. The CF1 is programmed to trigger a solenoid pump to inject the 50 μL pulses of tracer into the flow detection cell. Pulse injection rate is readily modified in the computer code to optimize for the conditions of each deployment, e.g. a temporal resolution of 0.5 minutes for flow rates >100 m/yr, 1 minute for >10 m/yr, 5 minutes for >1 m/yr, and 30 minutes for >0.1 m/yr can be obtained. Digital data is transferred from the OTIS for processing and real-time monitoring via a serial connection. After each pulse injection, the computer controls the switching on and off of the green LEDs that shine through the flow detection cell at the detection stations for photodiode measurements. In order to adequately capture the trough of the passing tracer pulse at high flow rates, the frequency of photodiode sampling is high (20 Hz) immediately after injection, and linearly slows to 0.03 Hz over 500 s to save power. Power consumption is also reduced for long term deployment capability by storing photodiode measurements and their corresponding time stamps in a memory buffer; and only when the buffer fills, the entire block of data in the buffer is saved to the CompactFlash card. At the default 30 minute injection frequency, the OTIS consumes 300 mW of power and 3 kB of data are gathered for every pulse or flow rate measurement. With its 512 MB card, the OTIS can gather data for flow rate determination for almost 10 years, far longer than the 18 months the alkaline power supply will last. Ultimately, the data logged on the CompactFlash card, or transmitted via serial communication in the case of a real-time connection to the OTIS, is processed using an algorithm that searches for the time of pulse arrival within the “detection window”, the window of time after an injection that a tracer pulse is expected to pass the detection station before the next injection. Using a calibration coefficient, a flow

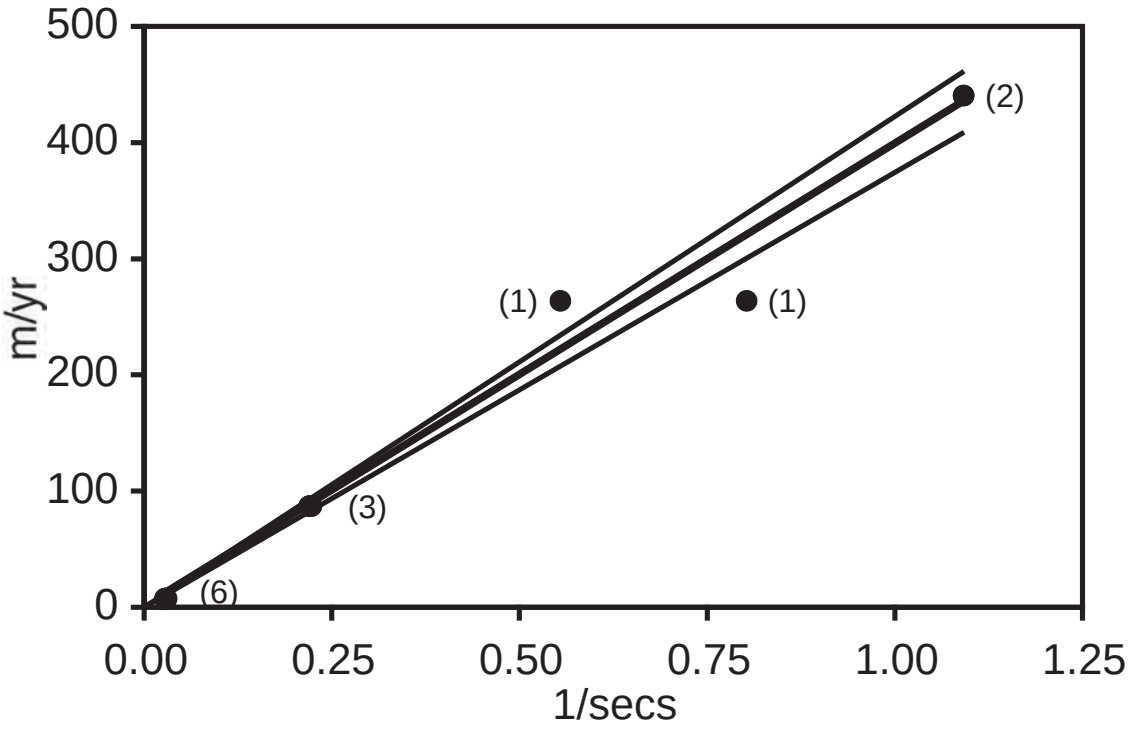

Figure 2-3. Calibration of the OTIS time of flight method for flow rate determination. Thirteen data points are plotted. The calibration coefficient relating flow rate vs. inverse time of flight to transmittance trough is calculated from the linear regression through the datum and origin. Upper and lower 95% confidence limits translate to a ±10% precision of flow rate determinations.

rate time series is obtained from the measurement of delay time after each pulse injection. The coefficient relating flow rate and the inverse of time of flight is essentially the distance between injection and detection locations, however, an instrument calibration is performed in the laboratory to account for offsets due to the nature of flow through a tube.

2.3 Determination of Flow Rate

To calibrate the OTIS and determine its range of sensitivity, we use a digitally controlled syringe pump to drive fluids at known flow rates through the flow detection cell. A marker in the digital signal had to be chosen to represent the time of tracer pulse arrival. Potential markers included onset, max slope, and trough of the pulse signal (Figure 2 inset). In order to determine which marker behaves most linearly and with the least scatter, we measured the time of flight from injection to the three markers during a test run of six different flow rates, corresponding to in-situ Darcy flow rates of 0.08 to 4.1 m/yr. As expected, arrival of the trough, corresponding to the center of the tracer pulse, behaved in a linear fashion. More scatter was observed at the front end of the pulse due to deviations during the initial injection of the pulse and diffusion. In another experiment, we set the digital pump to drive flow at four different rates, from 1 to 440 m/yr (Figure 3), to find the calibration coefficient of the simple rate law governing the relationship between Darcy flow rate and the inverse of time from pulse injection to our chosen detection marker, the trough of the transmittance signal.

2.4 OTIS Performance

The upper and lower limits of flow rate determination are based on the capability of accurately picking the trough in the digital signal. At seeps faster than the upper limit of 500 m/yr, the pulse passes by almost instantaneously relative to the time (0.3 s) for the pump to dispense the 50 μL volume of tracer, which becomes the limiting factor. A maximum lithostatic pressure gradient will not generate flows much above this upper limit at a seafloor seep environment with porous flow through the most permeable substrate we'd expect to encounter, sands. At low flow rates, less than 0.1 m/yr, injected pulses diffuse and don't completely travel past the detection station within the detection window, even with an injection rate of once every 45 minutes. At these low flow rates, tracer concentration gradually builds until an equilibrium concentration is reached. In this "mixed" case the transmittance value at equilibrium is directly related to the dilution factor and thus is a proxy for flow rate. The complications and drawbacks of using this method to determine absolute flow rates are: 1) the time for concentration to come to an equilibrium value is tens of hours due to infrequent pulse injections into a large volume flow cell, 2) the calibration curve is non-linear, 3) and photodiode voltages shift with temperature and light intensity. Still we can determine relative changes and make a qualitative analysis of flow rate by looking at changes in the average transmittance over each detection window.

Flow rate measurements in this 0.1 m/yr to 500 m/yr detection range are precise to ± 10%. Accuracy of determination of flow rate largely depends on the substrate in which the external collection chamber is placed, e.g. whether it is a porous matrix, and if so, whether its hydraulic conductivity is less than the effective conductivity of the OTIS meter. Generally, as long as the OTIS chamber is inserted into a porous sediment

matrix of equal or lesser permeability, there will be little to no deflection around the instrument. An analogy between Darcy's law and Poiseulle's law relates hydraulic conductivity to the square of the tubing radius [*Domenico and Schwartz*, 1998]. This suggests that the doubling of the OTIS meter's outlet tubing diameter should result in the quadrupling of the conductivity, i.e. 0.004 cm/sec, over the CAT meter conductivity of 0.001 cm/sec [*Tryon et. al.*, 2001]. As the OTIS outlet tube is in three sections, with constricting bulkhead connectors and right angles, it was necessary to perform empirical tests. Fourteen measurements to determine the OTIS meter's effective hydraulic conductivity, κ_e, were made using falling head and constant head tests [*Domenico and Schwartz*, 1998]. The resulting κ_e of 0.005 ± 0.002 cm/sec is equivalent to the conductivity of a silty to well sorted sand [*Freeze and Cherry*, 1979]. We deem that the deflection of flow around the instrument will not be significant on the clay to silt substrates typical of cold seep environments (Figure 4).

In the unusual case of a cold seep fed by flow through a fracture that extends completely through to the surface, the assumption of flow through a porous media is no longer valid and the permeability of that fracture is most certainly higher than that of the instrument. In this situation flow is impeded and there is deflection around the instrument and order of magnitude accuracy is not achieved. However, because backpressure varies linearly with flow rate, the magnitude of change in measured flow rate is a function of the magnitude of change in the unimpeded hydrologic flow. Furthermore, deflection of flow around the instrument doesn't affect the phase of flow rate responses. Therefore in a fracture environment, the relative flow rate measurements

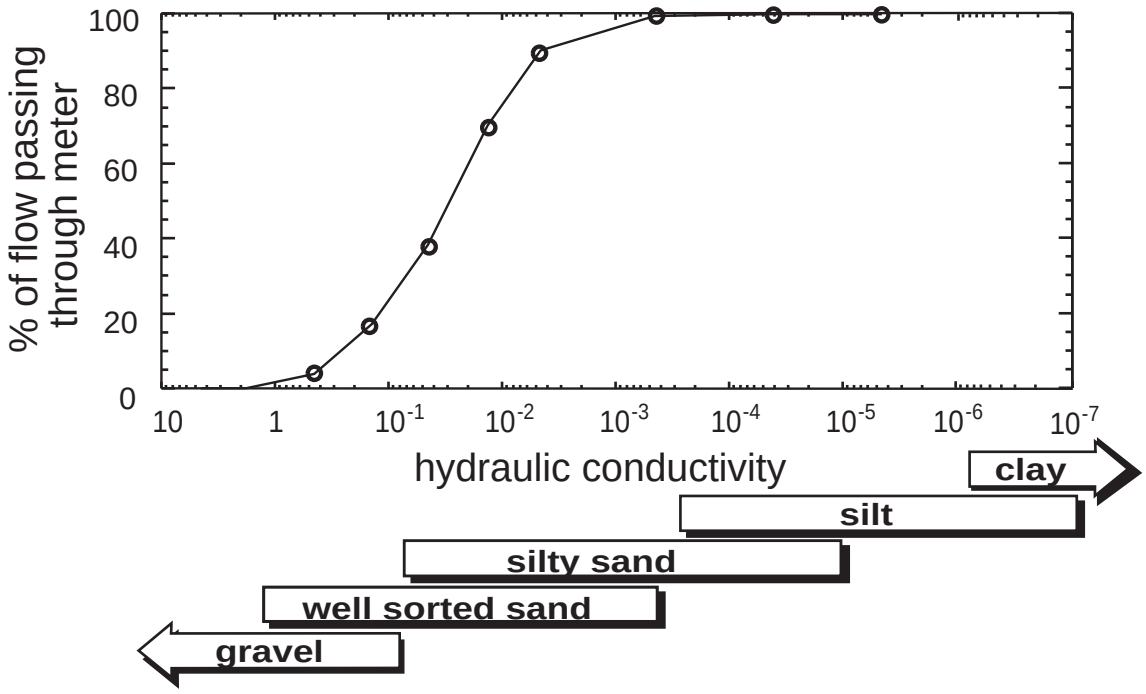

Figure 2-4. Numerical model results of flow through the meter/seafloor system adapted from Tryon et. al. [2001]. The percentage of flow through the OTIS meter is a function of the hydraulic conductivity of porous matrix substrates in which the OTIS meter external collection chamber is inserted. Conductivity ranges for sediment types [Freeze and Cherry, 1979] are graphically depicted.

that the OTIS records allow us to study our primary interest, variation of flow rate in response to tectonic driving forces.

A field test of the OTIS meter in an extreme environment demonstrates its improvement over previous flow meters for measuring rapid changes in flow rate. The OTIS was deployed for a 15 minute test in the beach sand just beyond the surf zone off the Scripps Pier (La Jolla, CA) to measure short-period oscillation and rapid flow rates from wave induced flow through the highly permeable sands. As the design goal of the OTIS is to detect transient events related to seismic activity, successful detection of flow rate in this environment with high frequency oscillations would render the instrument's capabilities more than adequate.

In order to capture oscillatory flow of wave periods around 8 to 20 s, a tracer pulse was injected every 2 s. This high injection frequency increases the risk of tracer building up in the system if flow velocities aren't high enough to flush the tracer. Using SCUBA, we deployed the OTIS in 8 m water depth, within the surge zone, and pushed the external chamber into the sandy substrate. A pressure sensor simultaneously recorded wave heights at a 2 Hz sample rate.

Upon recovery the downloaded record of transmittance shows that a build up of tracer occurred over the 15 minute deployment. This is evidence that injected pulses flow up, and down, past detection stations more than once in this oscillating flow environment. In this situation, teasing out the trough associated with each tracer injection to determine flow rates is impractical. Even if times of flight were measured, the result wouldn't be representative of the true flow rate because of rapidly varying flow rate in this oscillatory regime with a 14 second period (Figure 5a,b). Instead, we

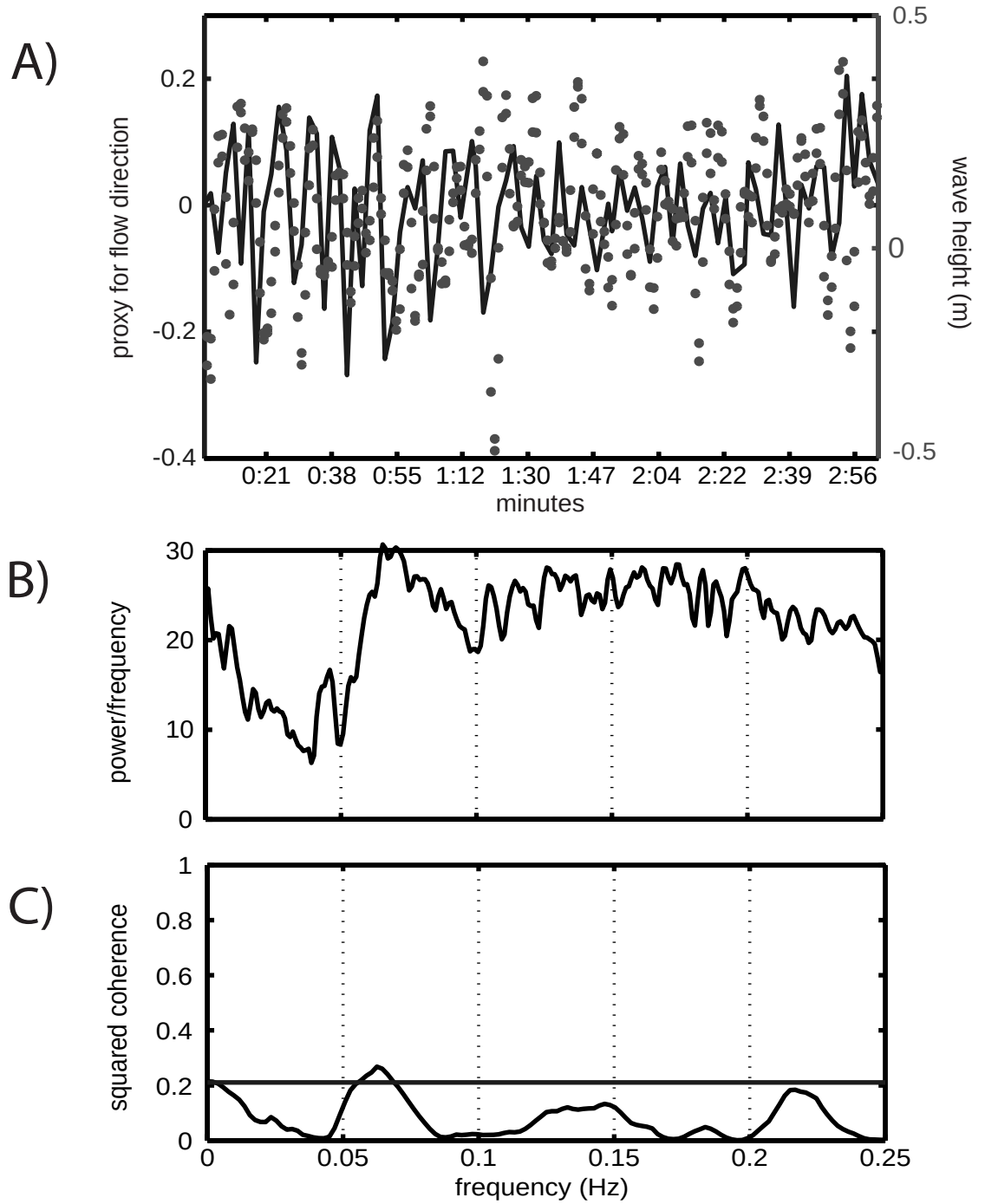

Figure 2-5. Wave pumping in a sandy offshore environment. A) A 3 minute segment of variability in fluorescence at the upstream detection station less that at the downstream detection station calculated over each 2 second detection window, a proxy for flow direction (black line); and measured wave height (grey circles). B) Power spectrum of the full 15 minute wave height record using Welch's method. C) Squared coherence between wave heights and proxy for flow direction. Horizontal line represents 95% confidence limit.

define a proxy for the direction of flow (Figure 5a). This proxy for flow direction is positive when first motion is in the outflow direction and negative for inflow first motion. This proxy is not calibrated and is only used to determine direction of flow. A cross-correlation analysis between wave height and the proxy for flow direction gives a coherence value above the 95% confidence limit at wave frequencies. This is a remarkable performance for such an extreme flow environment.

3. Monterey Bay

Monterey Bay, a well explored section of seafloor in central California with documented active cold seeps in a tectonic zone [e.g. *Martin et al.*, 1997; *Stakes et al.*, 1999; *Greene et al.*, 1999; *Paull et al.*, 2005], was chosen for the first scientific investigation using the OTIS. Located in a broad zone that is the boundary between the Pacific and North American plates, tectonic activity in the Monterey Bay region is transpressional [*DeMets*, 1990]. The Monterey and the San Gregorio Fault Zones cut the bay with a NNW-SSE trend (Figure 6).

Extrovert Cliff, at N36° 46.6’ W122° 05.1’, is a lineament of about a half dozen cold seeps in Monterey Bay lying at a 220° trend along the 950 m contour. Visual flow activity is evidenced at some seeps by "blow out" holes indicating fluid conduits and surrounding bacterial mat and clams. The vigorous outflow at these seeps is reportedly a recent development [*Plant et. al.,* 2001; *Girguis*, personal correspondence, 2004; *Martin et al.*, 2004]. Activity at other seeps in the lineament, as indicated by bacterial mat and surrounding clam beds, is more diffuse [*Kulm et al.*, 1986; *Rathburn et al.*, 2003]. Clearly active, the Extrovert Cliff seeps provide the potential to measure

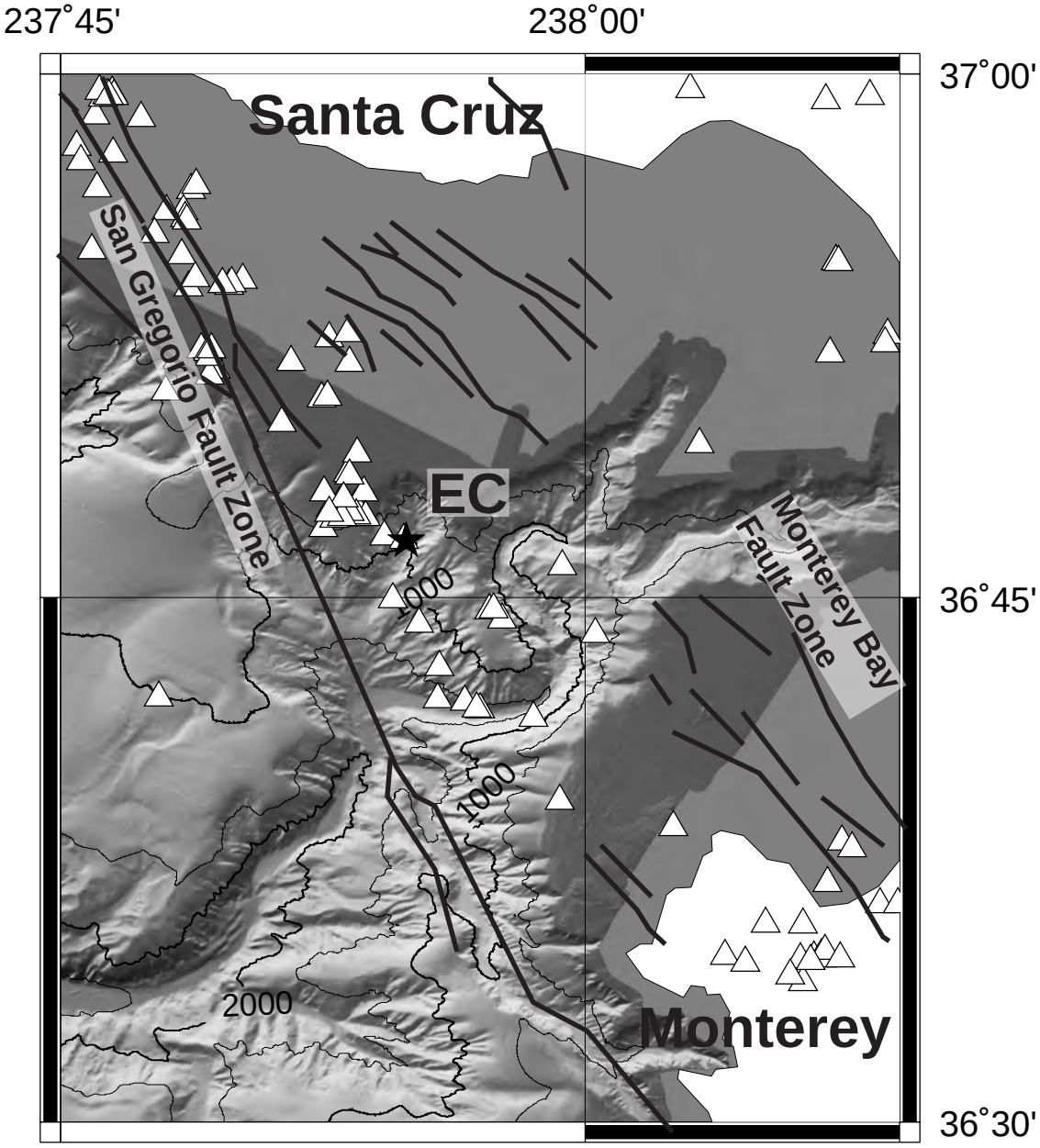

Figure 2-6. Location of Extrovert Cliff (EC) seep site (star) in relation to Monterey Bay faults [Greene, 1977] and seismicity (triangles- NCEDC epicenters of earthquakes with magnitude ≥2 earthquakes after 1967).

transience in flow rate and fluid chemistry resulting from tidal oscillations and possibly tectonic events. Specific seeps within the lineament were chosen for the two OTIS deployments in Monterey Bay to investigate the OTIS meter performance at different flow rates within the OTIS's sensitivity range. Seep A is the furthest northeast site in the lineation of seep sites. The bacterial mat was surrounded on the down-slope side by a large, 10-meter diameter, bed of clams (Figure 7a). Seep site B, 15 m southwest of site A, is clearly a more vigorous seep with fluids visibly flowing out of a small 1 to 3 cm diameter area (Figure 7b). Macrobiological communities at this site consist of a 2 to 3-meter-long clam bed extending down slope from a one-meter diameter area that is devoid of clams. To ensure a clean OTIS record for accurate flow rate determination at both seep sites, a conservative approach was taken and the OTIS computer was programmed to inject a pulse of tracer every 30 minutes for a total of 48 flow rate measurements per day. A companion CAT meter was linked in series with the OTIS to check flow rate calibration and to collect pore fluid. To sample gas chemistry during the August deployment, the CAT meter upstream coil was a gas tight copper coil with shut off valves to collect seep fluids uncontaminated by CAT tracer injection.

On 15 March 2004, the OTIS package was deployed with MBARI's ROV *Ventana* on seep site A. The ROV *Ventana* set the OTIS frame adjacent to the seep and the flow collection chamber was pushed down to seal into the soft silty-clay sediments over the focus of the seep, the bacterial mat. A Sontek Argonaut Acoustic Doppler Current Profiler was deployed at the site to confirm whether flow rates are independent of bottom currents. The OTIS and current meter were recovered on 29 March 2004.

A)

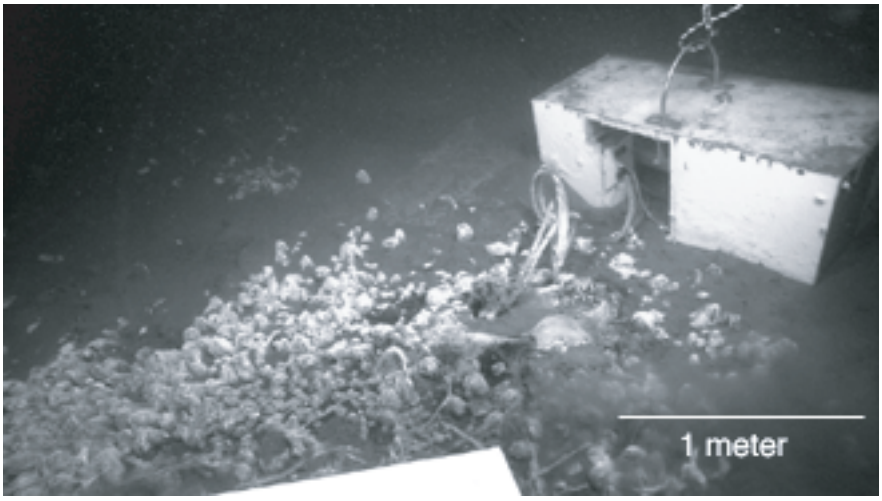

B)

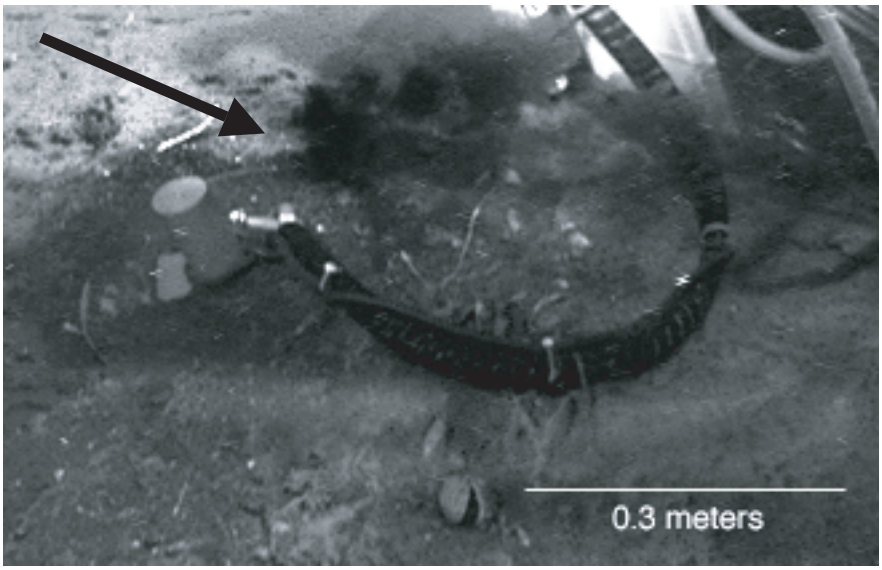

Figure 2-7. OTIS deployed at Extrovert Cliff seep sites in Monterey Bay. A) Seep site A. B) Seep site B, arrow points to visible expelled fluids around chamber before it was sealed into the sediment (images provided courtesy of MBARI, all rights reserved).

On 8 August 2004, the OTIS was deployed at seep B. The ROV pushed the collection chamber, with a temperature sensor mounted inside, into a 0.3 m diameter, clam free, bacterial mat zone including the blow out hole (Figure 7b). Chamber placement was adjusted until seep fluids could no longer be seen escaping around the edges of the chamber. The OTIS meter was recovered on 27 August 2004.

Upon recovery the clams were still healthy and grey bacterial mat fibers had grown over the chamber and on the tubing and sides of the instrument frame at both seeps A and B. The abundant growth on the instrument indicates high growth rate and presumably significant outflow rates. Temperature and current meter records, and flow rate data from the OTIS, were downloaded and processed. CAT meter sample coils were sub-sampled at appropriate intervals, and samples were diluted 1 to 100 and analyzed for tracer content and major seawater chemistry using an ICP-OES, Inductively Coupled Plasma Optical Emission Spectrometer. The copper sample coil from the August deployment was given to our collaborators, *Fueri et. al*. [2005] for helium analysis.

3.1 Monterey Results

The OTIS transmittance record, and CAT data, indicated outflow at both seep sites A and B. Flow rates at seep site A during the March deployment were at the low end of the OTIS's detection range using the time of flight method. Flow rates of 0.4 ± 0.1 m/yr were calculated. The larger scatter in the OTIS measurements at this low flow rate site compared to CAT meter flow rate measurements averaging 0.23 m/yr with daily variability of up to 0.03 m/yr is due to tracer build up in the flow detection cell.

Despite uncertainty of the time of flight analysis, relative changes in flow rate can be determined using the OTIS meter's mixed mode analysis. The proxy for flow rate, average transmittance over the detection window, does a good job at relative flow rate determination once the tracer adequately mixes and the system comes to equilibrium. Note the OTIS flow detection cell, designed for higher flow rates measurable with the time of flight method, has a much larger diameter tube as compared to the CAT meter, hence a longer equilibration time (Figure 8a). At the end of the time series, the OTIS average transmittance mimics the shape of the CAT meter flux record.

Flow rates at the vigorous seep site B during the August deployment were within the optimal range for the OTIS time of flight method at 20 to 60 m/yr (Figure 9a). CAT meter flow rates measured comparably at 10 to 60 m/yr confirming the accuracy of the OTIS calibration. We expect deflection around the instrument occurred due to the lower effective permeability of the instrument in comparison to the permeability of this seep with a visible hole through which fluids were expelled.

With the improved resolution and temporal accuracy of the OTIS's time series as compared to the CAT meter, it is possible to determine lag times and phase shifts between flow rate variations and forcing processes. In this record tidal forcing appears to drive flow rate variations (Figure 9). There are two potential processes that could cause a variation in the flow rate record at tidal frequencies: changes in bottom water currents flowing around the instrument package creating localized pressure perturbations, and tidal loading. Using cross-correlation analyses [*Parker*, personal correspondence, 2004] between flow rates and tides, and flow rates and current, we show an insignificant correlation between tides and currents, but a coherency of 0.99

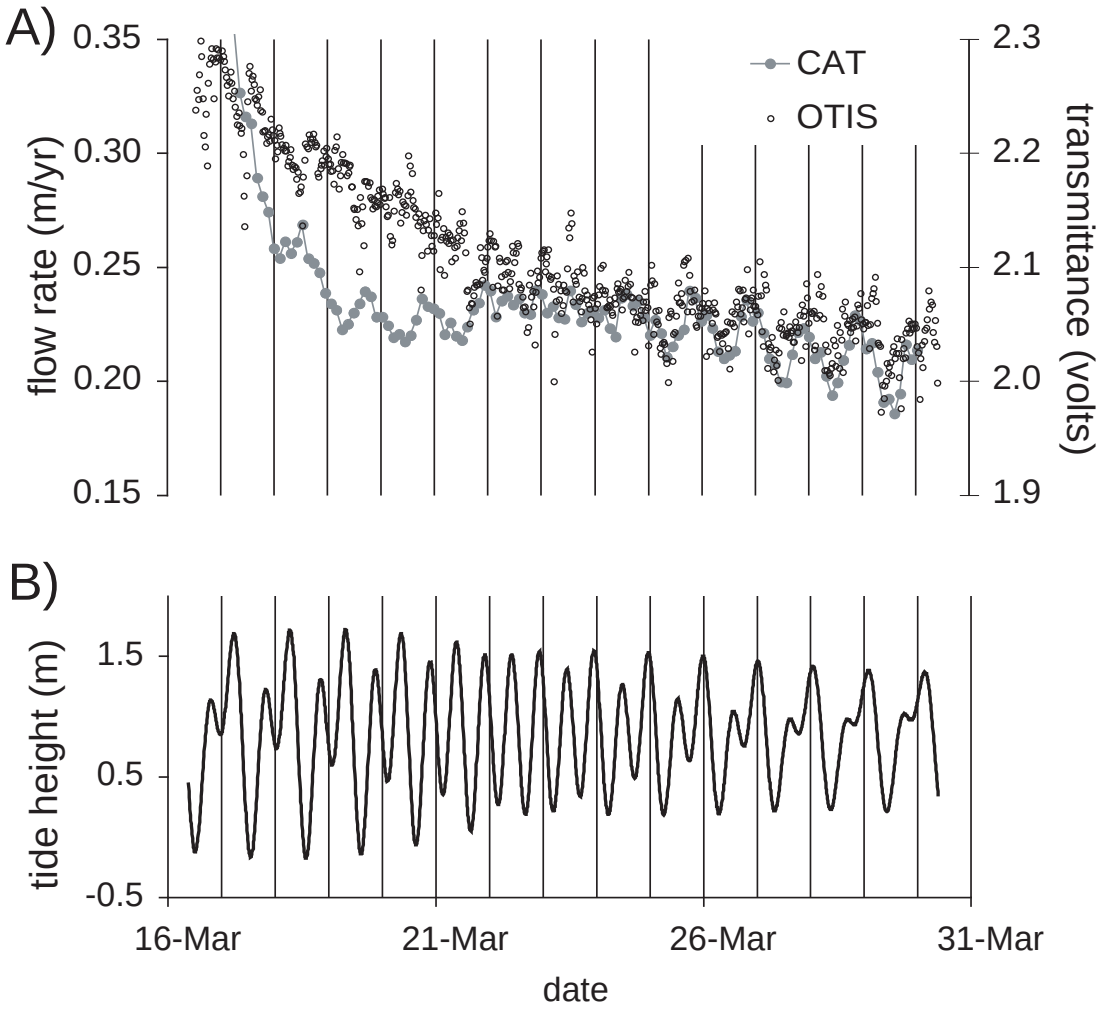

Figure 2-8. Time series of March, 2004 deployment at seep A: A) CAT meter temporal record of in-situ Darcy flow rate assuming uniform distribution of flow through the SWI over the collection chamber area and OTIS mixed method flow rate proxy: average transmittance over 30 minute detection window. B) Tidal height in meters recorded at Moss Landing NOAA buoy.

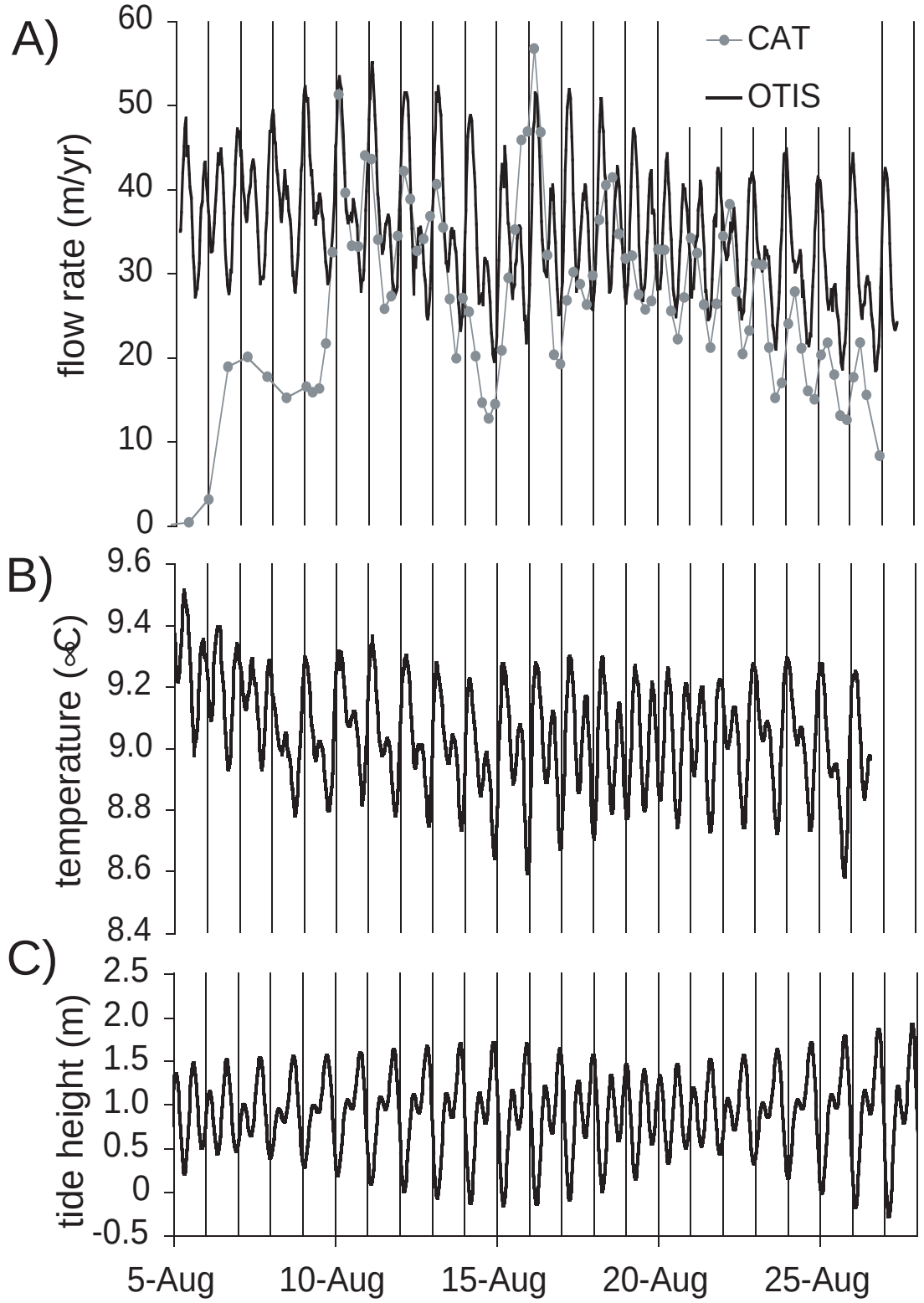

Figure 2-9. Time series of August, 2004 deployment at seep B. A) CAT (grey dotted line) and OTIS in-situ Darcy flow rate measurements, B) temperature measured in collection chamber and C) tidal height.

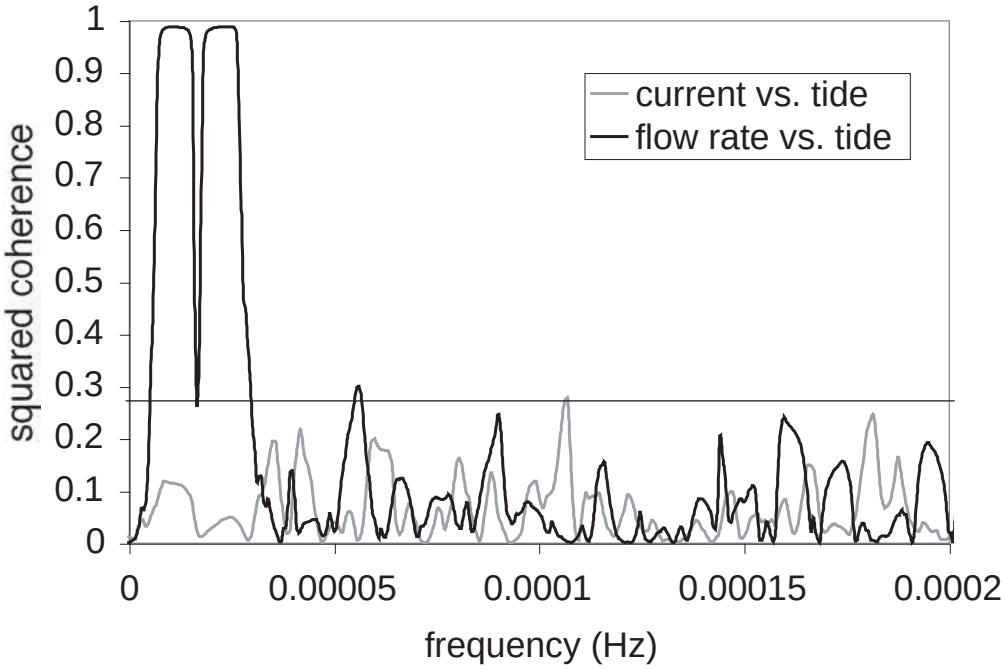

Figure 2-10. Cross-correlation of the OTIS flow rate record and tide (black line) and current meter record and tide (grey line). Horizontal line is 95% confidence limit.

between tides and flow rates (Figure 10). This implies that the tidal overburden pressures, not bottom currents, are driving flow rates.

The August temperature record measured an average of 9°C, which is 5°C above normal seafloor temperature (Figure 9b). A chemical analysis of fluids from the CAT meter shows the average concentration of major ions are highly altered relative to bottom standard concentrations (Table 1). Preliminary analysis of dissolved gas extracted from the end of the copper sample coil resulted in a He content of ~7 x 10^{-8} cm^3STP/gH_2O [*Fueri et al.*, 2005] which is 75% greater than that of ambient seawater at 4°C [*Ozima and Podosek*, 1983]. The $^3He/^4He$ ratio of this sample is 1.9 Ra.

Table 2-1. Chemical content of Extrovert Cliff seep site B effluent and IAPSO standard.

	B (μM)	Ca (mM)	K (mM)	Li (μM)	Mg (mM)	Na (mM)	S (mM)	Sr (μM)
seep	695	15.7	6.1	50	30	559	4.5	406
seawater	416	10.5	10.4	27	54	480	28.9	87

4. Discussion

Data from the Extrovert Cliff deployments allow us to clarify the nature of the hydrologic system driving these seeps. We observed sustained net outflow of fluid from the seep site and a strong tidal overprint in the flow rate and temperature records. Possible mechanisms driving outflow are thermal buoyancy, overburden and/or tectonic stresses at depth. Although we cannot conclude the source of overpressure, our observations suggest that the fluids coming from depth are focused along a fault or fracture. This conclusion is based on the site's proximity to a line of seismicity striking parallel to, and in-between the San Gregorio and Monterey Bay Fault Zones (Figure 6,

[*Paull et al.*, 2005]), and the nature of the hydrogeologic system inferred from flow rate and temperature response to tidal forcing.

Changes in tidal height load and unload the seafloor. The fraction of the load borne by the pore fluids is known as the loading efficiency, γ, and $0 < \gamma < 1$ [*Wang and Davis*, 1996; *Jupp and Schultz*, 2004]. The changes in pore fluid pressure drive fluid flow. There are two endmember models for periodic flow at the seafloor in response to periodic loading: an unconfined aquifer and a confined aquifer [*Bredehoeft*, 1967]. An unconfined aquifer is simply a saturated porous layer that continues up to the SWI. Fluids are able to diffuse from high to low pressure through the SWI. A confined aquifer is a saturated porous layer at depth, confined by an overlying, less permeable layer. Pressure changes with loading and unloading of tides are not able to equilibrate through diffusion out of the porous layer.

The timing of pore pressure response to a periodic load is different for these two endmembers. Pore pressure response is the sum of the undrained and drained response to a load [*Rice and Cleary*, 1976; *Roeloffs*, 1996; *Wang*, 2000]. The undrained response is the instantaneous change in pore pressure resulting from the load, γdp, and is in-phase with load. The drained response is a subsequent change in pore pressure with time as fluids diffuse to obtain equilibrium with hydrostatic pressures and lags the loading.

The unconfined aquifer endmember exhibits both undrained and drained responses. Under periodic loading pore pressure decays with depth as fluid diffusion only penetrates to a depth dependent on the frequency of periodic loading and hydraulic diffusivity of the porous layer, the penetration depth [*Vanderkamp and Maathuis*, 1991]. This diffusive pore pressure signal, the drained response, lags the tidal loading

signal [*Wang and Davis*, 1996] and the resulting flow velocity through the SWI lags the tide with a phase angle of -90° to -135° depending on the penetration depth relative to the thickness of the unconfined porous layer [*Jupp and Schultz*, 2004].

The confined aquifer endmember, solely responding to loading in an undrained manner, has a pore pressure response that is in-phase with periodic loading. Like well height response to barometric pressure changes, flow rates from a well-like seep at the seafloor connected to an overpressured confined aquifer are highest under minimum tidal load and lowest under maximum tidal load [*Jacob*, 1940; *Wang*, 2000; *Matsumoto et al.*, 2003]. This negative relationship is because the change in aquifer pressure, $dp_{aquifer,}$ is equal to the increased pressure in the aquifer due to the tidal load, γdp_{tide}, minus the pressure of the tidal load pressing down directly on the well-like orifice, dp_{tide}:

$$dp_{aquifer} = -(1-\gamma)dp_{tide}, \quad (1)$$

where dp_{tide} is the change in overburden pressure due to tide height changes.

A cross-correlation analysis to calculate the phase lag between flow rate and tidal records shows the flow rate is approximately in phase with diurnal (-4.5° ± 7.5°) and semidiurnal (3.8° ± 15°) tidal forcing and the highest outflow occurs at low tide (Figure 9a,c). We conclude that fluids at seep site B are primarily sourced from a confined aquifer at depth. The phase shift of less than the 30 minute temporal resolution requires that the fluid contribution from the overlying unconfined aquifer layer is small

relative to the confined aquifer contribution. Furthermore, the hydrogeologic system must be a well-like system in that an extremely permeable pathway must exist that allows for unimpeded flow between the confined aquifer and the seep. A fracture is a probable structure connecting the confined aquifer to the surface.

Fluid temperatures of up to 9.5°C, and averaging 9.0°C, suggest the confined aquifer source is at a minimum depth, assuming no conductive heat loss, of 110 m, assuming a geotherm in this active seep environment at a continental border is similar to the 50°C/km geotherm at Hydrate Ridge [*Shipboard Scientific Party*, 1994]. A maximum source water temperature of around 25°C, calculated using the Li-Mg geothermometer (Kharaka and Mariner, 1989) and measured ion concentrations (Table 1), suggests a maximum source depth of 500 m. We estimate the background overpressure of the aquifer, $p_{aquifer}$, using the parallel plate model for flow through a fracture [*Snow*, 1968] which relates average flow velocity, q, to pressure, p, in the following manner:

$$q = -\frac{h^2}{12\mu}\frac{dp}{dl}. \tag{2}$$

Holding constant the dynamic viscosity of the fluid, μ, the fracture aperture, h, and length, dl, we equate ratios of driving pressure to flow rate:

$$p_{aquifer} = \frac{q}{dq} dp_{aquifer}, \tag{3}$$

where q, the background (average) outflow rate, measures 40 m/yr, and dq, the flow rate change that results from the change in aquifer pressure, $dp_{aquifer}$, coinciding with the 1.5 meter tidal oscillation (dp_{tide} = 15 kPa), measures 30 m/yr (Figure 9). Substituting these values and equation (1) into equation (3) gives:

$$p_{aquifer} = \frac{4}{3}(1-\gamma)(15\text{kPa}). \quad (4)$$

Using loading efficiency values for underlying Purisima sandstone and Salinian granite units [*Greene,* 1990; *Stakes et al.,* 1999] of 0.27 for fractured sandstone [*Wang,* 2000] to 0.4 for fractured granite [*Lee and Lee,* 2000], aquifer overpressure is approximately 12 to 15 kPa. For the confined aquifer constrained at a minimum (maximum) depth of 110 (500) m, this is less than 0.2% (0.05%) of lithostatic pressure. The proposed combination of a confined aquifer and a high permeability fracture connecting the source of deepwater to the surface explains how a minimally overpressured fluid could drive the fluids at rates high enough that we can visually observe them seeping from the blowout hole.

In addition to flow rate, temperature of outflowing fluids varies with tidal forcing with a similar negative relationship. The cross-correlation analysis between temperature and tide height records shows the temperature lags the inverse of diurnal (semidiurnal) tide, and flow rate record in-phase with the tides, by 10° ± 0.1° (14° ± 0.2°). The cause for temperature variation that lags the tide could be 1) solely heat loss

by conduction through the fracture walls, or 2) a combination of conductive cooling and cooling through mixing with a cold, shallow fluid source. Consider the first possibility: with a variable flow rate, fluids spend a variable length of time traveling from depth to the surface and are thus not equally subjected to heat loss through conductive cooling. The hottest fluid expelled from the cold seep must have spent a period of time in the fracture pathway centered around the time of peak outflow rate in order to undergo minimal heat loss. The travel time of this packet of fluid is then twice the lag of the temperature record behind the flow rate record. If heat loss is the sole reason for the measured 28 minute (semidiurnal) to 40 minute (diurnal) lag in the temperature record, we can infer a travel time of 56 to 80 minutes. From a source depth of 110 to 500 m, we conclude the fluids are flowing through the fracture at a linear velocity of centimeters per second. The second potential cause of the observed temperature variability is a variable input from the shallow, cold water in the unconfined aquifer. Tidal pumping driving flow into and out of the overlying unconfined surface sediments drives peak colder water outflow at falling tide. Adding the maximum volume of cool fluid into the mix at falling tide (90° to 135° after peak tide) will shift the temperature low from being in phase with the tide high, to lagging the tide high. As both of these hypotheses generate similar phase shifts, we aren't able to distinguish the degree of fluid contribution from the shallow source. However, the lack of phase shift in the flow rate response allows us to assume the contribution from this unconfined shallow source is negligible.

A second fluid source, not necessarily a shallow source, is still required to explain long-term patterns in flow rate and temperature records. Long-term variation in

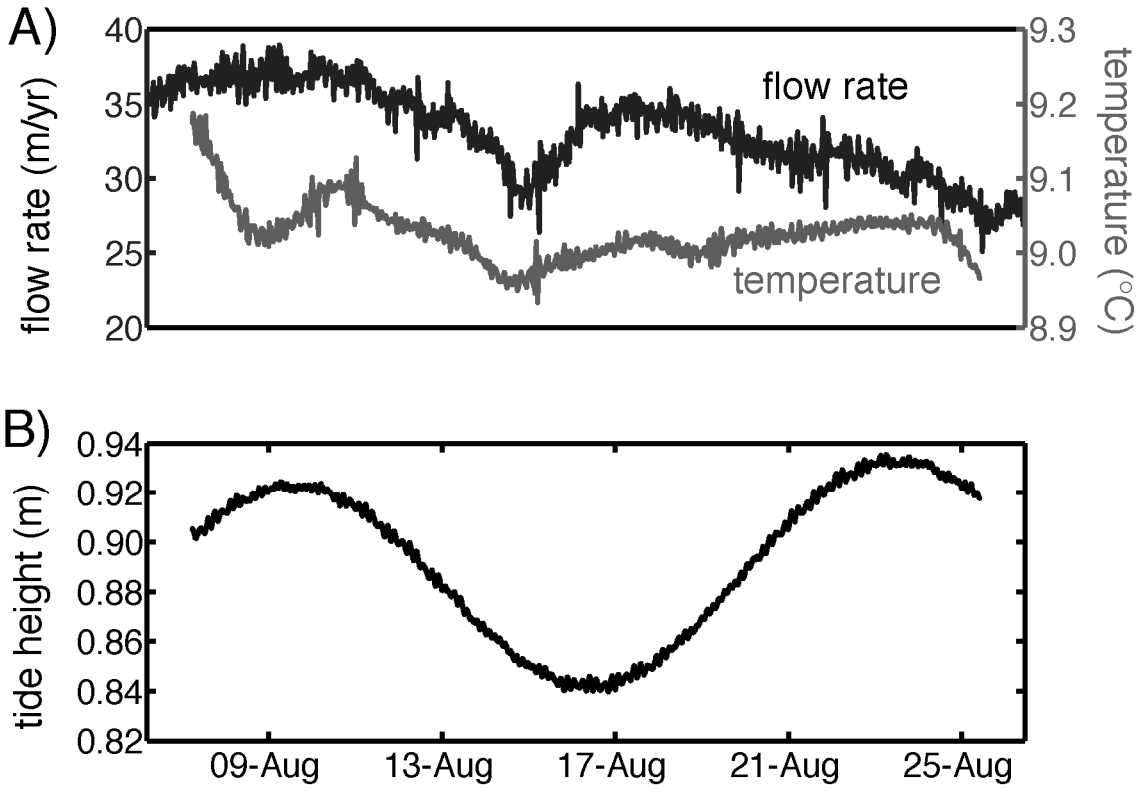

Figure 2-11. August data filtered with a 5x10-6 to 5x10-5 Hz band-stop FIR filter: A) filtered temperature (grey) and flow rate (black) record, B) filtered tidal record.

temperature and flow rate is evident after filtering out tidal frequencies with a $5x10^{-6}$ to $5x10^{-5}$ Hz band-stop FIR filter (Figure 11). If the hydrologic system has simply one source, one would expect a positive relationship between changes in temperature and flow at low frequencies as was observed at higher tidal frequencies. Some portions of the record do indeed show a positive correlation between temperature and flow rate, however, others do not, for example, the beginning of the record. Here, an increase in the ratio of high temperature source to cool source must be occurring since a drop in flow rate is not causing the drop in temperature.

The measured $^{3}He/^{4}He$ ratio of up to 1.9 Ra [*Fueri et al.*, 2005] implies that an additional source beneath the confined aquifer contributes to the hydrogeologic system. A small component of mantle helium measuring 8 Ra [*Graham*, 2002] leaking from a much greater depth into the confined aquifer driving outflow at the Extrovert Cliff seeps could result in this elevated $^{3}He/^{4}He$ ratio in the expelled fluids. Better temporal resolution gas analyses to investigate the nature of the variability of helium are underway and will help to further constrain the hydrogeologic system and relative source contributions.

High frequency variations are evident in the flow rate and temperature records after we filter out the tidal signal (Figure 11). A cross-correlation analysis revealed that SWI temperature measured within the external chamber has a three-hour period and coheres with measured changes in ambient bottom water temperature. The change in the SWI temperature data resulting from heat transfer from the bottom water through the instrument collection chamber is insignificant, measuring a maximum change of 0.05°C ± 0.001°C, one tenth of the change in bottom water temperature. Larger temperature

transients in the record therefore reflect a true change in temperature of the seeping fluid at the SWI. Transients observed in the flow rate record are also partially due to actual changes in the rate of seeping fluid, and the remainder is due to system error inherent to the time of flight method. Using the high frequency variation to estimate an upper bound on the error, we conclude flow rate observations are precise to ±2.5%. The system is more accurate than confidence limits obtained during laboratory calibration suggest.

5. Conclusion

Laboratory calibration and sensitivity studies demonstrate that the OTIS meter can measure flow rates of 0.1 m/yr to >500 m/yr and achieve a high temporal accuracy and resolution with its optical/electronic method for flow rate determination. The success of the OTIS meter in its intended seep environment is demonstrated through field tests. The improved capability of the OTIS to log high frequency and high amplitude flow rate changes accurately makes correlation analysis of flow rate record with potential driving forces possible.

Future directions for this instrument include an intelligent software upgrade and a merged OTIS-CAT instrument for low flow rate environments. For the OTIS user to set frequency of the tracer injection to record flow rates at optimal temporal resolution, the flow rates at a site need to be known pre-deployment. For example, with the high outflow at Extrovert Cliff seep B a temporal record with at least twice the resolution could have been obtained had we known the background flow rate in advance. Since the OTIS software is easily modified, a desired improvement would be to program an

intelligent algorithm for determining flow rates in situ so the tracer injection rate can be automatically modified accordingly. For seeps that are known to have low flow rates (less than 0.20 m/yr) the CAT meters are currently the best technology for long-term monitoring. However, CAT meters lack high temporal accuracy, resolution, and the ability to interface with underwater networks. We intend to develop a CAT meter with the optics and electronics of the OTIS for these types of environments.

Acknowledgements

We would like to thank MBARI, the R/V Point Lobos and ROV Ventana crew, and Dr. Peter Girguis for seep site location information and enabling instrument deployments and recoveries in Monterey Bay. Evelyn Fueri and Dr. Dave Hilton provided results from helium analyses completed in the Fluids and Volatiles Lab at Scripps Institution of Oceanography. Reviewers Dr. Geoffrey Wheat and Dr. Earl Davis contributed significant insight in the review process. Funding has been generously provided by the National Science Foundation (OCE02-41998), NOAA's Undersea Research Program (UAF04-0034), and the WM Keck Foundation Grant to the University of Washington.

This chapter, in full, is a reprint of the publication: LaBonte, A., K. Brown, and M. Tryon (2007), Monitoring periodic and episodic flow events at Monterey Bay seeps using a new optical flow meter, *Journal of Geophysical Research*, *112*, B02105, doi:10.1029/2006JB004410.

References

Bekins, B.A., A.M. McCaffrey, and S.J. Dreiss, (1995), Episodic and constant flow models for the origin of low-chloride waters in a modern accretionary complex, *Water Resour Res*, *31*, 3205-3215.

Bredehoeft, J.D., (1967), Response of Well-Aquifer Systems to Earth Tides, *Journal of Geophysical Research*, *72*, 3076-3087.

Brown, K.M., D.M. Saffer, and B.A. Bekins, (2001), Smectite diagenesis, pore-water freshening, and fluid flow at the toe of the Nankai wedge, *Earth and Planetary Science Letters*, *194*, 97-109.

Brown, K.M., M.D. Tryon, H.R. DeShon, L.M. Dorman, and S.Y. Schwartz, (2005), Correlated transient fluid pulsing and seismic tremor in the Costa Rica subduction zone, *Earth and Planetary Science Letters*, *238*, 189-203.

Chadha, R.K., A.P. Pandey, and H.J. Kuempel, (2003), Search for earthquake precursors in well water levels in a localized seismically active area of Reservoir Triggered Earthquakes in India, *Geophysical Research Letters*, *30*(7), 1416, doi:10.1029/2002GL016694.

Davis, E.E., K. Becker, K.L. Wang, K. Obara, Y. Ito, and M. Kinoshita, (2006), A discrete episode of seismic and aseismic deformation of the Nankai trough subduction zone accretionary prism and incoming Philippine Sea plate, *Earth and Planetary Science Letters*, *242*, 73-84.

Davis, E.E., D.S. Chapman, M.J. Mottl, W.J. Bentkowski, K. Dadey, C. Forster, R. Harris, S. Nagihara, K. Rohr, G. Wheat, and M. Whiticar, (1992), Flankflux - an Experiment to Study the Nature of Hydrothermal Circulation in Young Oceanic-Crust, *Canadian Journal of Earth Sciences*, *29*, 925-952.

Davis, E.E., and H.W. Villinger, (2006), Transient formation fluid pressures and temperatures in the Costa Rica forearc prism and subducting oceanic basement: CORK monitoring at ODP Sites 1253 and 1255, *Earth and Planetary Science Letters*, *245*, 232-244.

Davis, E.E., K. Wang, R.E. Thomson, K. Becker, and J.F. Cassidy, (2001), An episode of seafloor spreading and associated plate deformation inferred from crustal fluid pressure transients, *Journal of Geophysical Research-Solid Earth*, *106*, 21953-21963.

DeMets, C., (1990), Current plate motions, *Geophysical Journal International*, *101*, 425-478.

Domenico, P.A., and F.W. Schwartz, (1998), *Physical and Chemical Hydrogeology*, 2nd ed., 506 pp., John Wiley & Sons, New York.

Freeze, R.A., and J.A. Cherry, (1979), *Groundwater*, 604 pp., Prentice Hall, Englewood Cliff, NJ.

Fueri, E., D.R. Hilton, K.M. Brown, and M.D. Tryon, (2005), Helium and Carbon Isotope Systematics of Cold Seep Fluids at Monterey Bay (California, USA), *Eos Trans. AGU*, *86*(52), Fall Meet. Suppl., Abstract V13C-0563.

Ge, S., and E. Screaton, (2005), Modeling seismically induced deformation and fluid flow in the Nankai subduction zone, *Geophysical Research Letters*, *32*, L17301, doi:10.1029/2005GL023473.

Graham, D.W., (2002), Noble gas isotope geochemistry of mid-ocean ridge and ocean island basalts: characterization of mantle source reservoirs, in *Noble gases in geochemistry and cosmochemistry*, edited by D. Porcelli, C.J. Ballentine, and R. Wieler, pp. 247-317, United States (USA).

Greene, H.G., (1977), Geology of the Monterey Bay region, *Open-File Report*, *77-718*, 347 pp., U.S. Geological Survey.

Greene, H.G., (1990), Regional tectonics and structural evolution of the Monterey Bay region, central California., in *Geology and Tectonics of the central California Coast Region, San Francisco to Monterey, Pacific Section. American Association of Petroleum Geologists, Volume and Guidebook*, edited by R.E. Garrison, H.G. Greene, K.R. Hicks, G.E. Weber, and T.L. Wright, pp. 31-56, Pac. Sect. Am. Assoc. of Pet. Geol., Bakersfield, Calif.

Greene, H.G., N. Maher, T.H. Naehr, and D.L. Orange, (1999), Fluid flow in the offshore Monterey Bay region, in *Late Cenozoic Fluid Seeps and Tectonics Along the San Gregorio Fault Zone in the Monterey Bay Region, California. American Association of Petroleum Geologists, Pacific Section, Volume and Guidebook*, edited by R.E. Garrison, I.W. Aiello, and J.C. Moore, pp. 1-19, Pac. Sect. Am. Assoc. of Pet. Geol., Bakersfield, Calif.

Han, M.W., and E. Suess, (1989), Subduction-Induced Pore Fluid Venting and the Formation of Authigenic Carbonates Along the Cascadia Continental-Margin - Implications for the Global Ca-Cycle, *Palaeogeography Palaeoclimatology Palaeoecology*, *71*, 97-118.

Italiano, F., and G. Martinelli, (2001), Anomalies of mantle-derived helium during the 1997-1998 seismic swarm of Umbria-Marche, Italy, *Geophysical Research Letters*, *28*, 839-842.

Jacob, C.E., (1940), On the flow of water in an elastic artesian aquifer, *Transactions-American Geophysical Union*, *22*, 783-787.

Johnson, H.P., M. Hutnak, R.P. Dziak, C.G. Fox, I. Urcuyo, J.P. Cowen, J. Nabelek, and C. Fisher, (2000), Earthquake-induced changes in a hydrothermal system on the Juan de Fuca mid-ocean ridge, *Nature*, *407*, 174-177.

Jonsson, S., P. Segall, R. Pedersen, and G. Bjornsson, (2003), Post-earthquake ground movements correlated to pore-pressure transients, *Nature*, *424*, 179-183.

Jupp, T.E., and A. Schultz, (2004), A poroelastic model for the tidal modulation of seafloor hydrothermal systems, *Journal of Geophysical Research-Solid Earth*, *109*, B03105, doi:10.1029/2003JB002583.

Kennedy, B.M., Y.K. Kharaka, W.C. Evans, A. Ellwood, D.J. DePaolo, J. Thordsen, G. Ambats, and R.H. Mariner, (1997), Mantle fluids in the San Andreas fault system, California, *Science*, *278*, 1278-1281.

Kharaka, Y.K., and R.H. Mariner, (1989), Chemical geothermometers and their applications to formation waters from sedimentary basins, in *Thermal history of sedimentary basins : methods and case histories*, edited by N.D. Naesser, and T.H. McCulloh, pp. 99-117, Springer-Verlag, New York.

King, C.Y., N. Koizumi, and Y. Kitagawa, (1995), Hydrogeochemical Anomalies and the 1995 Kobe Earthquake, *Science*, *269*, 38-39.

Kulm, L.D., E. Suess, J.C. Moore, B. Carson, B.T. Lewis, S.D. Ritger, D.C. Kadko, T.M. Thornburg, R.W. Embley, W.D. Rugh, G.J. Massoth, M.G. Langseth, G.R. Cochrane, and R.L. Scamman, (1986), Oregon Subduction Zone - Venting, Fauna, and Carbonates, *Science*, *231*, 561-566.

Kulongoski, J.T., D.R. Hilton, and J.A. Izbicki, (2003), Helium isotope studies in the Mojave Desert, California: implications for groundwater chronology and regional seismicity, *Chemical Geology*, *202*, 95-113.

LaBonte, A.L., K.M. Brown, and Y. Fialko, (2005), Consecutive Flow Events and Propagating Aseismic Slip at the Costa Rica Forearc: Matching Models to Measurements, *Eos Trans. AGU*, *86*(52), Fall Meet. Suppl., Abstract T13B-0459.

Langseth, M.G., and E.A. Silver, (1996), The Nicoya convergent margin - A region of exceptionally low heat flow, *Geophysical Research Letters*, *23*, 891-894.

Lee, J.Y., and K.K. Lee, (2000), Use of hydrologic time series data for identification of recharge mechanism in a fractured bedrock aquifer system, *Journal of Hydrology*, *229*, 190-201.

Linde, A.T., K. Suyehiro, S. Miura, I.S. Sacks, and A. Takagi, (1988), Episodic Aseismic Earthquake Precursors, *Nature*, *334*, 513-515.

Linke, P., E. Suess, M. Torres, V. Martens, W.D. Rugh, W. Ziebis, and L.D. Kulm, (1994), In-Situ Measurement of Fluid-Flow from Cold Seeps at Active Continental Margins, *Deep-Sea Research Part I-Oceanographic Research Papers*, *41*, 721-739.

Manga, M., E.E. Brodsky, and M. Boone, (2003), Response of streamflow to multiple earthquakes, *Geophysical Research Letters*, *30*(5), 1214, doi:10.1029/2002GL016618.

Martin, J.B., S.A. Day, A.E. Rathburn, M.E. Perez, C. Mahn, and J. Gieskes, (2004), Relationships between the stable isotopic signatures of living and fossil foraminifera in Monterey Bay, California, *Geochemistry Geophysics Geosystems*, *5*, Q04004, doi:10.1029/2003GC000629.

Martin, J.B., D.L. Orange, T.D. Lorenson, and K.A. Kvenvolden, (1997), Chemical and isotopic evidence of gas-influenced flow at a transform plate boundary: Monterey Bay, California, *Journal of Geophysical Research-Solid Earth*, *102*, 24903-24915.

Matsumoto, N., G. Kitagawa, and E.A. Roeloffs, (2003), Hydrological response to earthquakes in the Haibara well, central Japan - I. Groundwater level changes revealed using state space decomposition of atmospheric pressure, rainfall and tidal responses, *Geophysical Journal International*, *155*, 885-898.

Montgomery, D.R., H.M. Greenberg, and D.T. Smith, (2003), Streamflow response to the Nisqually earthquake, *Earth and Planetary Science Letters*, *209*, 19-28.

Moore, J.C., and P. Vrolijk, (1992), Fluids in Accretionary Prisms, *Reviews of Geophysics*, *30*, 113-135.

Mottl, M.J., C.G. Wheat, P. Fryer, J. Gharib, and J.B. Martin, (2004), Chemistry of springs across the Mariana forearc shows progressive devolatilization of the subducting plate, *Geochimica Et Cosmochimica Acta*, *68*, 4915-4933.

Muir-Wood, R., and G.C.P. King, (1993), Hydrological Signatures of Earthquake Strain, *Journal of Geophysical Research-Solid Earth*, *98*, 22035-22068.

Ozima, M., and F.A. Podosek, (1983), *Noble gas geochemistry*, Cambridge University Press, Cambridge.

Paull, C.K., B. Schlining, W. Ussler, J.B. Paduan, D. Caress, and H.G. Greene, (2005), Distribution of chemosynthetic biological communities in Monterey Bay, California, *Geology*, *33*, 85-88.

Plant, J.N., C. G. Wheat, and H. Jannasch, (2001), A peek at fluid flow in Monterey Bay cold seeps using peepers, *EOS Trans. AGU*, *82*(47), Fall Meet. Suppl., Abstract OS42A-0468.

Pruis, M.J., and H.P. Johnson, (2004), Tapping into the sub-seafloor: examining diffuse flow and temperature from an active seamount on the Juan de Fuca Ridge, *Earth and Planetary Science Letters*, *217*, 379-388.

Rathburn, A.E., M.E. Perez, J.B. Martin, S.A. Day, C. Mahn, J. Gieskes, W. Ziebis, D. Williams, and A. Bahls, (2003), Relationships between the distribution and stable isotopic composition of living benthic foraminifera and cold methane seep biogeochemistry in Monterey Bay, California, *Geochemistry Geophysics Geosystems*, *4*(12), 1106, doi:10.1029/2003GC000595.

Rice, J.R., and M.P. Cleary, (1976), Some Basic Stress Diffusion Solutions for Fluid-Saturated Elastic Porous-Media with Compressible Constituents, *Reviews of Geophysics*, *14*, 227-241.

Roeloffs, E., (1996), Poroelastic techniques in the study of earthquake-related hydrologic phenomena, in *Advances in Geophysics, Vol 37*, pp. 135-195.

Roeloffs, E.A., (1998), Persistent water level changes in a well near Parkfield, California, due to local and distant earthquakes, *Journal of Geophysical Research-Solid Earth*, *103*, 869-889.

Rojstaczer, S., and S. Wolf, (1992), Permeability Changes Associated with Large Earthquakes - an Example from Loma-Prieta, California, *Geology*, *20*, 211-214.

Saffer, D.M., and E.J. Screaton, (2003), Fluid flow at the toe of convergent margins: interpretation of sharp pore-water geochemical gradients, *Earth and Planetary Science Letters*, *213*, 261-270.

Sano, Y., N. Takahata, G. Igarashi, N. Koizumi, and N.C. Sturchio, (1998), Helium degassing related to the Kobe earthquake, *Chemical Geology*, *150*, 171-179.

Sato, T., R. Sakai, K. Furuya, and T. Kodama, (2000), Coseismic spring flow changes associated with the 1995 Kobe earthquake, *Geophysical Research Letters*, *27*, 1219-1222.

Schultz, A., P. Dickson, and H. Elderfield, (1996), Temporal variations in diffuse hydrothermal flow at TAG, *Geophysical Research Letters*, *23*, 3471-3474.

Shipboard Scientific Party, (1994), Site 892, in *Proc. ODP, Init. Repts.*, edited by G.K. Westbrook, B. Carson, R.J. Musgrave, and e. al., pp. 301-388, Ocean Drilling Program, College Station, TX.

Silver, E., M. Kastner, A. Fisher, J. Morris, K. McIntosh, and D. Saffer, (2000), Fluid flow paths in the Middle America Trench and Costa Rica margin, *Geology*, *28*, 679-682.

Snow, D.T. (1968), Rock fracture spacings, openings, and porosities, *J. Soil Mech. Found. Div., Proc. Amer. Soc. Civil Engrs*., *94*, 73-91.

Stakes, D.S., D. Orange, J.B. Paduan, K.A. Salamy, and N. Maher, (1999), Cold-seeps and authigenic carbonate formation in Monterey Bay, California, *Marine Geology*, *159*, 93-109.

Sugisaki, R., and T. Sugiura, (1985), Geochemical Indicator of Tectonic Stress Resulting in an Earthquake in Central Japan, 1984, *Science*, *229*, 1261-1262.

Tivey, M.K., A.M. Bradley, T.M. Joyce, and D. Kadko, (2002), Insights into tide-related variability at seafloor hydrothermal vents from time-series temperature measurements, *Earth and Planetary Science Letters*, *202*, 693-707.

Toutain, J.P., and J.C. Baubron, (1999), Gas geochemistry and seismotectonics: a review, *Tectonophysics*, *304*, 1-27.

Tryon, M., K. Brown, L.R. Dorman, and A. Sauter, (2001), A new benthic aqueous flux meter for very low to moderate discharge rates, *Deep-Sea Research Part I-Oceanographic Research Papers*, *48*, 2121-2146.

Tryon, M.D., K.M. Brown, and M.E. Torres, (2002), Fluid and chemical flux in and out of sediments hosting methane hydrate deposits on Hydrate Ridge, OR, II: Hydrological processes, *Earth and Planetary Science Letters*, *201*, 541-557.

Tsunogai, U., and H. Wakita, (1995), Precursory Chemical-Changes in-Ground Water - Kobe Earthquake, Japan, *Science*, *269*, 61-63.

Vanderkamp, G., and H. Maathuis, (1991), Annual Fluctuations of Groundwater Levels as a Result of Loading by Surface Moisture, *Journal of Hydrology*, *127*, 137-152.

Vrolijk, P., A. Fisher, and J. Gieskes, (1991), Geochemical and Geothermal Evidence for Fluid Migration in the Barbados Accretionary Prism (ODP Leg 110), *Geophysical Research Letters*, *18*, 947-950.

Wakita, H., (1975), Water Wells as Possible Indicators of Tectonic Strain, *Science*, *189*, 553-555.

Wang, H.F., (2000), *Theory of linear poroelasticity with applications to geomechanics and hydrogeology*, 287 pp., Princeton University Press, Princeton, NJ, United States (USA).

Wang, K.L., and E.E. Davis, (1996), Theory for the propagation of tidally induced pore pressure variations in layered subseafloor formations, *Journal of Geophysical Research-Solid Earth*, *101*, 11483-11495.

Wheat, C.G., and R.E. McDuff, (1995), Mapping the Fluid-Flow of the Mariana Mounds Ridge Flank Hydrothermal System - Pore-Water Chemical Tracers, *Journal of Geophysical Research-Solid Earth*, *100*, 8115-8131.

Chapter 3

A Yearlong Hydro-tectonic Study at the Nootka Transform-Cascadia Subduction Triple Junction

Abstract

A recently developed electronic flow meter was integrated into a real-time observatory at the triple junction where the Nootka transform fault meets the Cascadia subduction zone. Measurements from the flow meter, other hydrologic sensors, and an ocean bottom seismometer were transmitted via acoustic modem to a surface buoy, and via satellite to an onshore receiving station. Although the technical aspects of the real-time test were a success, scientific results were minimal. A simultaneous deployment of a suite of osmotic flow meters, however, yielded four yearlong time-series of rates of flow through the sediment-water interface at seep sites in the vicinity of the Nootka-Cascadia junction. Patterns of flow on all four instruments are similar from January through March of 2005. Deformation from seismic events registered in the CNSN catalogue possibly explain the later two of the four flow events during this period of regional flow events. Additional local seismic events were detected by the three MBARI seismometers deployed at the study site and nearby on the North American and Explorer plates. The first of these events approximately coincides with the two earlier events in the flow rate time series. With a temporal accuracy of ± 7 days, we are unable to link the timing of flow events with recorded seismic deformation and aseismic deformation is also a potential cause for part or all of the observed regional flow events.

1. Introduction

Subduction zones accumulate stress during tectonic compression. This stress is periodically released in the form of great earthquakes. The coseismic vertical displacement of the seafloor generates tsunamis and the shaking triggers turbidite flows,

or submarine landslides. The most recent great earthquake at the Cascadia subduction zone, located off Northwestern US and Southwestern Canada, occurred on 26 January 1700 according to the written record of a tsunami wave hitting Japan [*Satake et al.*, 1996]. The periodicity of these large magnitude events as evidenced by turbidite flow deposits [*Goldfinger et al.*, 2003] averages ~600 years with the shortest interval measuring 215 years and the longest 1488 years. Because of these seismic hazards, it is important to study subduction zones and particularly deformation events that occur during the interseismic period between large subduction zone earthquakes.

The seismogenic zone is where the subducting plate is locked to the overlying continental plate and accumulating stress during the interseismic period. Stable sliding occurs landward of the downdip limit of the seismogenic zone where rocks at higher temperatures deform in a plastic, rather than brittle, fashion [*Hyndman et al.*, 1993; *Hyndman et al.*, 1997]. Stable sliding also occurs seaward of the updip limit where overlying sediments are unconsolidated. The transition between aseismic and stick-slip deformation at the updip limit coincides with strengthening of the boundary through thermally controlled diagenetic to low grade metamorphic processes and/or lower pore pressures landward of the updip limit [*Byrne et al.*, 1988; *Davis et al.*, 1989; *Vrolijk et al.*, 1991; *Hyndman et al.*, 1993; *Hyndman et al.*, 1997; *Moore and Saffer*, 2001; *Brown et al.*, 2003]. Using geodetic and thermal models the updip limit to downdip limit "width" of the Cascadia seismogenic zone was estimated at ~60km [*Hyndman and Wang*, 1995]. Although narrow for subduction zones, a rupture over this distance is liable to produce a magnitude 8 earthquake.

The aseismic sections of the fault updip and downdip of the seismogenic zone episodically creep to relieve the small amounts of stress that accumulate. These creeping events may play a role in loading the seismogenic zone, possibly even triggering fault rupture [*Dragert et al.*, 2001; *Dragert et al.*, 2004]. To monitor the interseismic deformation, a growing number of land-based studies have used Global Positioning System (GPS) instrumentation [*Mazzotti et al.*, 2002; *Mazzotti et al.*, 2003; *Miyazaki et al.*, 2003; *Wang et al.*, 2003; *Zhao et al.*, 2003]. In Cascadia, aseismic slips downdip of the seismogenic zone and associated seismic noise have recently been recorded with continuous GPS instrumentation and seismic networks [*Rogers and Dragert*, 2003; *Dragert et al.*, 2004; *Kao et al.*, 2005]. However, scientists know little about the dynamics updip of the seismogenic zone because the deformation front lies offshore and only a few offshore geodetic measurements have been made at convergent margins [*Spiess et al.*, 1998; *Gagnon et al.*, 2005; *Fujita et al.*, 2006; *Tadokoro et al.*, 2006].

Recent offshore hydrogeologic observations demonstrate potential occurrences of aseismic activity seaward of the updip limit during the interseismic period [e.g. *Brown et al.*, 2005; *Davis et al.*, 2006]. Brown et al. [2005] used flow meters to measure the resulting fluid flow through the sediment-water interface from pore pressure changes concurrent with deformation events, seismic or aseismic, in the Costa Rica accretionary wedge. The pattern of outflow pulses, and low frequency "tremor" in the co-deployed OBS seismometer record, lead the authors to hypothesize an aseismic event occurred and propagated seaward from seismogenic updip limit. Davis et al. [2006] used borehole pressure measurements near the toe of the accretionary prism to

study interseismic deformation at the Nankai subduction zone. Like the flow rate measurements, direct measurements of pore pressure are sensitive to aseismic deformation. A comparison of the timing of a pore pressure transient observed on the accretionary wedge with that on the incoming plate, and seismicity records from a dense onshore seismic array network, together lead the authors to believe an aseismic slip initiated at the updip limit of the seismogenic zone and propagated seaward.

The study presented here was designed to build on this base of knowledge of subduction zone dynamics seaward of the updip limit by making long term observations at the toe of the Cascadia accretionary wedge using submersible instrumentation sensitive to both seismic and aseismic signals. Scientists and engineers from the Woods Hole Oceanographic Institution (WHOI), Monterey Bay Aquarium Research Institute (MBARI), University of Washington (UW) and Scripps Institution of Oceanography (SIO) were afforded the opportunity to make simultaneous hydrologic and tectonic observations using flow meters and seismometer arrays and transfer the data real-time. Much like the previously mentioned hydrologic studies, the capability to compare flow rate records with seismic events helps to identify which flow events may be resulting from aseismic deformation, or be amplified due to a concurrent aseismic event [e.g. *Davis et al.*, 2001]. Even if every flow event is accompanied by a seismic event, a comparison of the deformation state, dilational or compressional as determined from the focal mechanism, to the sense of flow can further our understanding of whether the hydro-tectonic response is due to permeability changes, dynamic or static deformation.

The real time observatory component of the Keck project entailed installing an acoustically linked moored-buoy system. This experiment was a test and proof of

concept before the planned implementation of a real-time cabled observatory, the North-East Pacific Time-Series Undersea Networked Experiments (NEPTUNE), which will provide power and communication for plate scale observations. Gathering data real-time has many advantages. There is no need to recover instruments for data download or to swap out batteries and create a gap in the continuous record. With real-time, the user, or a server onshore processing the incoming data with higher processing power than is practical on the seafloor, has a potential capability to respond to an event detected real-time, e.g. by sending out a tsunami warning, or bumping up the data collection rate to improve instrument resolution for the duration of the event. The NEPTUNE cabled observatory will improve the database of empirical measurements by an order of magnitude. This will allow scientists to address questions of the dynamics of faulting in a quantitative manner using long-term records with better temporal and spatial resolution to constrain their model analyses.

The flow meter instruments used in this study were placed on seeps on the tectonically active Juan de Fuca plate. Like terrestrial springs, seeps are focused channels that connect to larger submarine aquifers. By monitoring flow rates at seeps, pore pressure changes resulting from tectonic strain can be sensed, and clues about the nature of the seep structure and underlying aquifer can be gathered [*LaBonte et al.*, 2007]. In this chapter, we will discuss the engineering aspects and results of the real-time monitoring Nootka Buoy observatory test. The primary emphasis of this chapter, however, is the hydro-tectonic experiment also conducted at the Nootka-Cascadia junction.

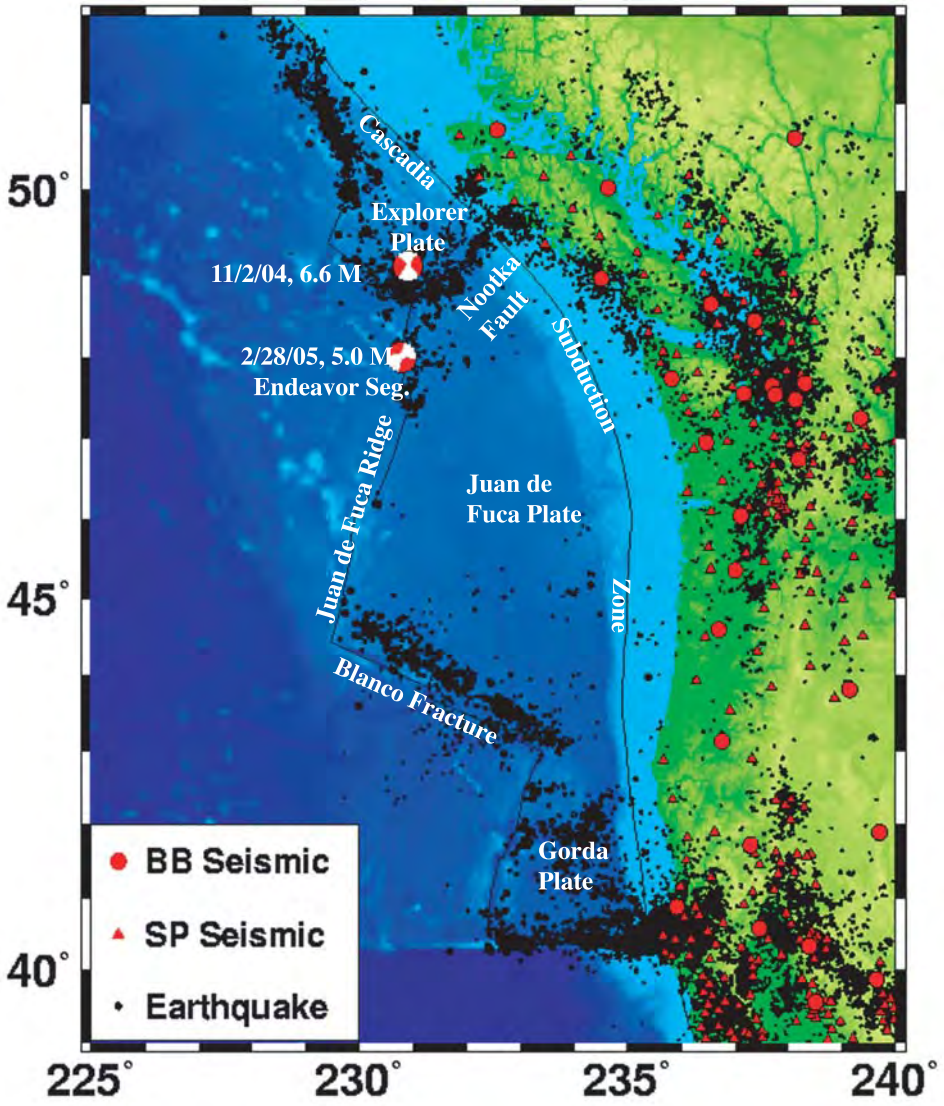

Figure 3-1. Map of the Juan de Fuca plate system, seismic networks, and seismicity over a several year period [courtesy of the NEPTUNE project]. Focal mechanisms for the large events that occurred during this study were obtained from the Harvard CMT website. Red quadrants are compressional, and white quadrants are dilational.

2. Geologic Setting

Only 80 km offshore Vancouver Island, BC, the Juan de Fuca plate is easily accessible from nearby ports. As a relatively small plate, the region has highly concentrated seismic activity on its divergent, convergent and two transform boundaries with the Pacific, North American, and Explorer and Gorda plates respectively (Figure 1). The Juan de Fuca plate system is a desirable location for the planned real-time observatory for geophysicists not only because of the seismic hazards and its proximity to shore, but because the plate is small. There are questions regarding the interactions between all three types of tectonic plate boundaries [*Kelley et al.*, 2006]. Simultaneous monitoring at all plate boundaries on this regional scale observatory will allow for investigation of, for example, ridge push verses slab pull, and whether intraplate deformation effects the surrounding plate boundaries

The Juan de Fuca plate is converging with the North American plate at approximately four centimeters per year [*DeMets*, 1990; *Riddihough and Hyndman*, 1991] in a northeast direction. The Nootka transform fault is the northern boundary between the Juan de Fuca and Explorer plates. Relative plate motion here is left-lateral with roughly three centimeters of motion per year [*Hyndman et al.*, 1979; *Riddihough and Hyndman*, 1991]. The sinistral motion is distributed across a zone of strike slip faults 20 km wide. The junction between the transform fault and the Cascadia subduction zone is a fault-trench-trench triple junction west of north-central Vancouver Island. Coinciding with where the fault zone intersects the margin is a preferential path for turbidite flows, which have carved out a “plunge pool”. The feature, and thus the triple junction, is easily located on the bathymetric map (Figure 2).

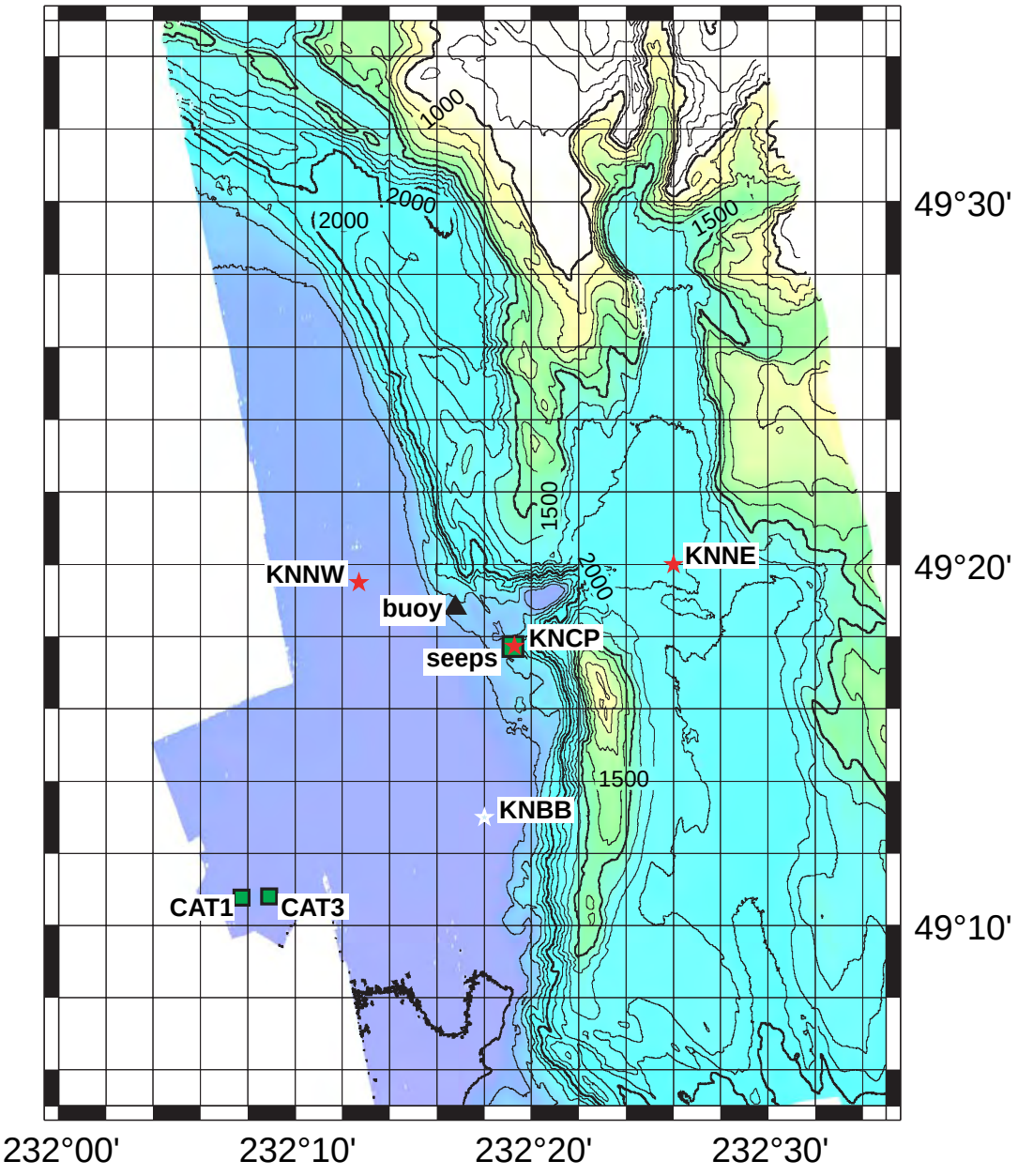

Figure 3-2. Bathymetric map (courtesy of University of Washington and the NEPTUNE project) with instrumented seep area and Nootka transform fault (green squares), WHOI buoy anchor location (black triangle), and short-period (red stars) and broadband (white star) seismometer locations. The Hyndman basin “plunge pool” is north of the seeps and east of the buoy.

In order to capture transients in flow rate using our hydrologic instrumentation, it is necessary to place the flow meters on cold seeps, identified by chemosynthetic biological communities. These are seafloor surface features with focused outflow as evidenced by the biological organisms surviving off the nutrients seeping from the seafloor. Due to the flow meter's method of flow rate determination, relative changes in flow rates are more easily distinguished when superimposed on a record of background outflow which seeps are likely to have. With a regional tectonic compression rate of ~4 cm/yr at the Cascadia subduction zone, pore fluids are likely overpressured near the deformation front and found escaping along pathways such as fractures or faults. Seeps were indeed discovered in the general area of the triple junction during a prior cruise, and the WHOI buoy was deployed to the northwest of the triple junction (Figure 2). The location of our study site, the "Nootka seep site", is just south of the Nootka-Cascadia junction on the toe of the accretionary prism.

3. Real-time Observatory Test

The Nootka Observatory, a collaborative effort between WHOI, UW, and SIO, is a moored-buoy system that uses acoustics to communicate with sensors on the seafloor and then transmits the data to shore via an Iridium satellite link (Figure 3). The instruments placed on the seafloor to observe the relationship of fluid flow and tectonic activity included a WHOI Ocean Bottom Seismometer (OBS) and the UW/SIO sensor package, or "hydronode", for monitoring fluid activity at the Nootka seep site. The hydronode was an assembly of three electronic sensors: a fluid resistivity probe, a heat flow probe, and the Optical Tracer Injection System (OTIS) flow meter; and a central

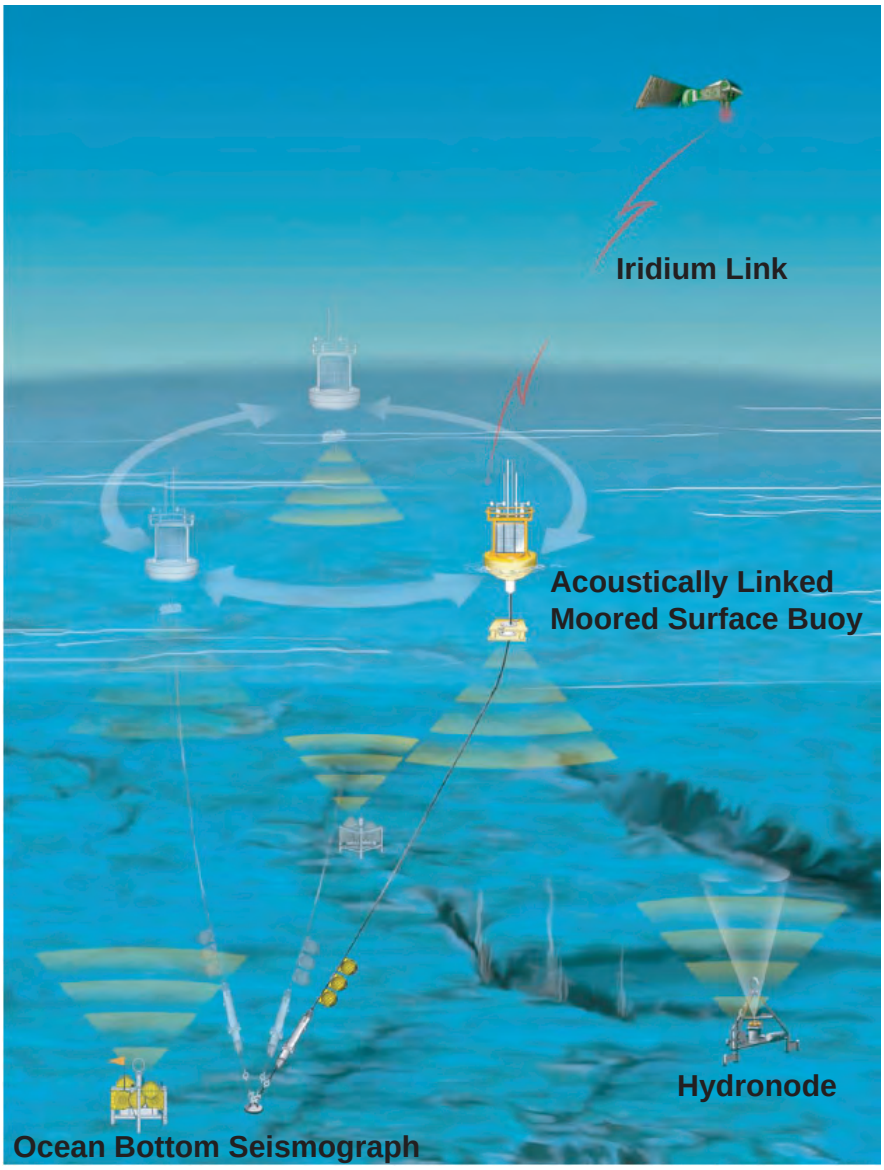

Figure 3-3. Acoustically-linked moored-buoy schematic modified from Frye et al. [2006].

data logger, the "Nootka Logger", packaged together with a high-data-rate, power efficient, acoustic modem developed at WHOI [*Freitag et al.*, 2000].

3.1 Instrumentation

Dr. Marvin Lilley's group from University of Washington contributed the resistivity and heat probes. Fluid resistivity is measured using a four electrode sensor. An AC signal is imposed across one pair of electrodes and fluid resistance is synchronously measured across the other pair of electrodes. The heat flow probe consists of four thermocouples capable of 0.01°C resolution placed 12, 7 and 2 inches below the sediment surface and one measuring the bottom water temperature 1 inch above the sediment surface.

The Optical Tracer Injection System, an electronic data logging flow meter designed for high resolution measurements in flow rate regimes ranging from 0.1 to >500 m/yr and programmed for real time data transfer, was developed at SIO. The OTIS measures aqueous flux at the seafloor by sealing into an area of the sediment surface and channeling the flow from this area through the instrument's outlet flow tube. Using a Persistor CF2 computer, 50uL pulses of fluorescent rhodamine tracer are injected into the flow tube (see Chapter 2, Figure 1). The pulse of tracer travels with the same velocity as the ambient flow through the flow tube. The computer records photodiode measurements of transmittance from an LED shining across the flow tube at detection stations located both upstream and downstream of the injection. The direction and rate of flow is determined from the "time of flight" of each individual tracer pulse

traveling from the injection to detection location. Data are transmitted real-time and a complete record is stored on Compact Flash for download upon recovery.

For deployment at the Nootka seep site, where flow rates are expected to be on the lower end of the OTIS's detection range, injections were 45 minutes apart to allow the slowly moving pulse of tracer to clear away before the next injection. Individual tracer pulses are then more easily distinguished from each other in the record making flow rate determination possible. To further improve resolution at low flow rates, a lower volume flow tube than in the original design was used to increase the speed of the pulse traveling through the outlet tube. Flow rates down to 0.05 m/yr are resolved with this setup. To power the OTIS electronics for the yearlong deployment at Nootka, the pressure housing was filled to capacity with 77 D-cell alkaline batteries.

Data from the hydronode's three sensors: the OTIS meter and resistivity and heat probes, all have to be passed to the modem for uplink to the surface buoy. Data are first collected on the Nootka Logger, and then passed to the hydronode modem. When the hydronode modem is interrogated the data are already packaged and ready for transmit. The Nootka Logger developed at UW is simply the data logger for the resistivity, and heat flow probe sensors, modified to communicate with the OTIS over a RS232 serial port and the hydronode modem. The heart of the Nootka Logger is an Onset Tattletale 8V2 microprocessor with 1MB of onboard memory and 192 MB of additional flash memory. The Nootka Logger is programmed to query the OTIS flow meter for its data before collectively passing all the data to the modem for transfer to the surface buoy.

A Chemical Aqueous Transport (CAT) meter is also included in the package to sample fluid chemistry in addition to gathering flow rate data alongside the OTIS. This osmotically driven flow meter is not electronic; therefore its data cannot be transferred in real-time. Although it is linked into the plumbing of the OTIS flow meter to gather data at the hydronode site, results from the CAT meter will be discussed in section 4.

All of the above instrumentation, and the WHOI modem, had to be assembled in a single robust package for maneuvering off the ship, into, and through the water column to the seafloor with an ROV, and for recovery. We, the UW/SIO collaborative group, decided the frame built to house the OTIS and CAT meters, being the largest and heaviest of all the instruments, would be a suitable platform for attachment of all the other instruments (Figure 4).

3.2 Data Transfer

Data transfer between the OTIS and Nootka Logger required a collaborative effort to design a physical electronic connection, develop a protocol for communication, and incorporate this protocol into the software. The cable used for the RS232 connection between the Nootka Logger and the OTIS meter was a six-foot long, six-conductor cable of which we wired three conductors, the ground, transmit, and receive lines for the serial connection. The communication protocol for data transfers between the UW Nootka Logger and WHOI modem, and WHOI modem to surface buoy, is to a large degree a black box. Information disclosed included the limitation on the amount of data that could be transmitted via the modem due to power constraints, which therefore limited the amount of data the OTIS could transfer to the Logger. We programmed the

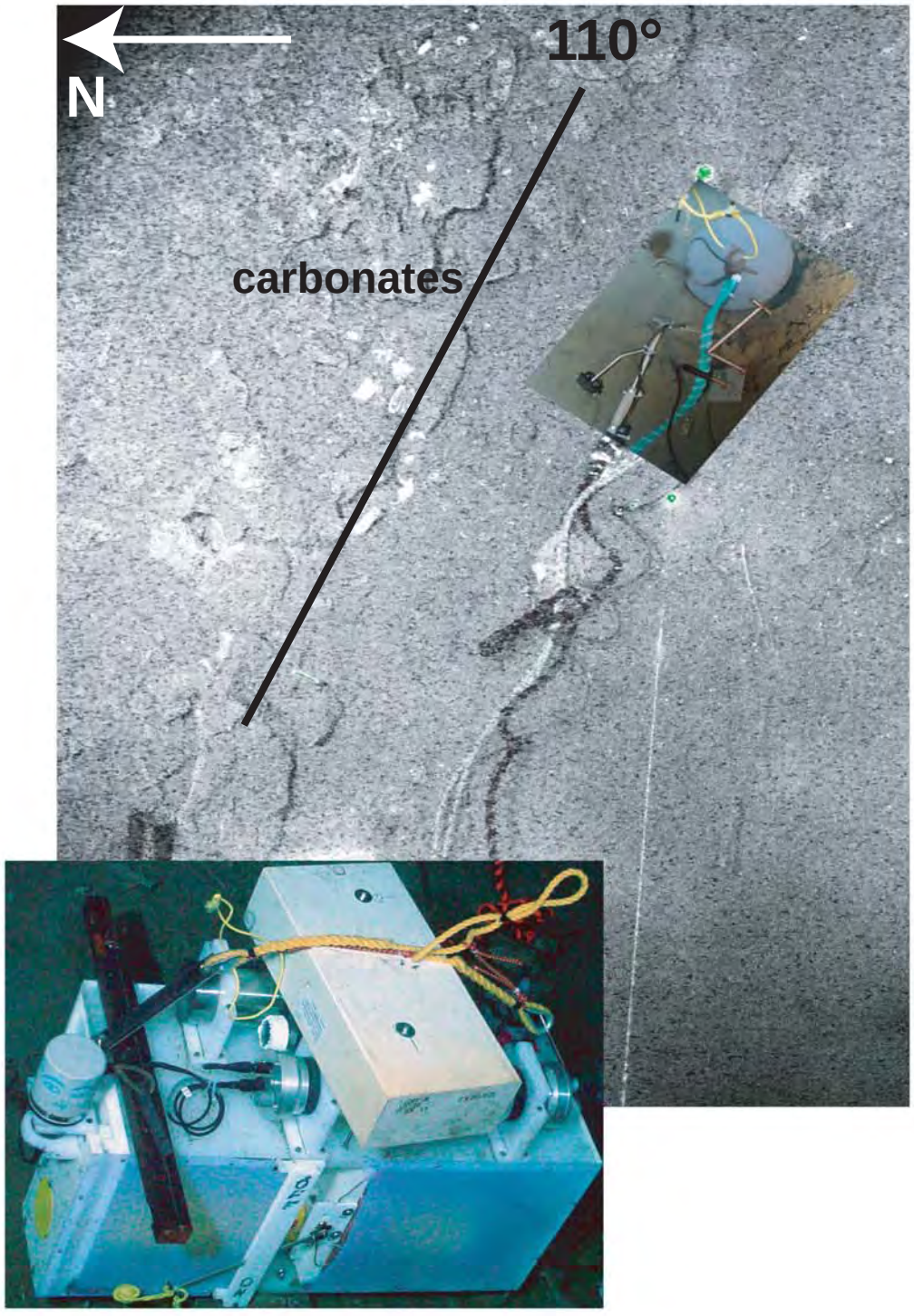

Figure 3-4. A mosaic of the Nootka tubeworm seep site. The hydronode package, the OTIS frame with Nootka Logger, modem with transducer and floatation mounted on the top is bottom left; hydrologic sensors inserted into the tubeworm seep is top right.

OTIS CF2 to store the most recent data in a cyclic buffer 743 samples long. Data in the cyclic buffer are broken into smaller blocks of data for transfer. Each block is 256 bytes long with the last 3 bytes storing block number, total number of blocks, and checksum values. The checksum was only used when processing the transmitted real-time data, as transmission errors over the short cable connection to the Nootka Logger were highly unlikely and the WHOI modem employed its own error checking protocol. We programmed the CF2 and Tattletale computers to follow the communication protocol outlined in Table 1. Every four hours the Logger Tattletale interrogates the OTIS, the OTIS CF2 responds with the number of blocks it will transfer in raw binary form, and when prompted, sends all blocks of data and the Tattletale acknowledges receipt of all blocks. The CF2 clears the data successfully transmitted from the cyclic buffer so only new data will be passed to the logger. If a transmit period is unsuccessful, the oldest samples in the cyclic buffer are overwritten as new samples are collected. The most recent data are then sent during the next transmission. After setting serial communication parameters, e.g. baud rate of 9600, we tested this protocol for data transfer with success.

The frequency of surface buoy to hydronode interrogations would be every 6 hours and last for 20 to 30 minutes. Among the many unknowns in this real-time observatory test were the effects of the high-voltage source of the acoustic modem during transmission on our electronic instrumentation. In case of accidental reset, the OTIS CF2 computer was set to boot the sampling application at power on, in which case the new data would be automatically appended to existing data files. The UW group received the modem a few days before heading out to sea, and tested for negative

effects of this electric current field on all three of our sensors. Fortunately, no problems were encountered.

Table 3-1. OTIS-Nootka Logger communication protocol

	sequence & timing of data & command transfer	
Task	**OTIS**	**Nootka Logger**
Send wake up command		S <0.5sec delay> S
Listen for response		<up to 5 seconds>
Pause between wake up attempts		<5 second delay>
Try a maximum of 3 times		
Respond	Blocks=XXXXX\r	
Listen for OK	<up to 10 seconds>	
return to sampling if no OK received		
Okay OTIS to send blocks of data		OK\r
send all 256 byte blocks	<1 second delay>	
	<block 1>	
	<1 second delay >	
	<block 2>	
	<…>	
	<1 second delay>	
	<block XXXXX>	
Listen for OK	<up to 5 seconds>	
Confirm receipt of all blocks		OK\r
Listen for OK	<up to 5 seconds>	
return to sampling		

3.3 Deployment

In fall of 2004, four months after the installation of the Nootka buoy and WHOI seismometer components of the Nootka observatory, the hydronode was installed at a seep 3.5 km southeast of the buoy anchor (Figure 2). This seep site, the most promising for making hydrologic measurements, was outside of the tested communication distance of the Nootka buoy. It was necessary to first test the communication between the

acoustic modem and the surface buoy at the seep site before committing to placing the hydronode there.

On 4 September 2004 ROPOS, University of Victoria's ROV, launched from the R/V Thomas Thompson carrying just the modem. We started communication tests within the buoy communication footprint, a radius of 2 km around the buoy anchor (and a line-of-sight distance to the buoy of 3 km if it were directly above its anchor), and moved away to the southeast. ROPOS set the modem on the seafloor, and transited away with the ship to minimize interference during buoy-modem connectivity tests. At all five test sites, most critically the final test at the active seep site proposed for the hydronode deployment, the buoy and seafloor modem were able to communicate. We had established that at least some data transmissions would be successful, especially with the help of prevailing northwest winds pushing the buoy closer to the seep site.

The modem was mounted back onto the hydronode, and on 6 September 2004, the hydronode package was loaded onto the ROPOS porch to be deployed at the seep site ROPOS navigated to the target site a seep site with a cluster of tubeworms living on the sedimented bottom and adjacent bacterial mat south of a 110° striking carbonate wall (Figure 4). Care was taken to align the hydronode package in a north-south orientation so the path from the modem transducer northwest and up to the buoy was clear of obstruction by either the carbonate shelf or the block of floatation mounted on the hydronode. After collecting the tubeworms for biological sampling, the heat flow probe and the resistivity-temperature probe were placed at the perimeter of the site. The OTIS chamber was then pushed into the center of the tubeworm seep site. Post deployment, the WHOI team remotely configurated the Linux based controller of the

buoy system adding the hydronode component of the observatory into the task management.

3.4 Results

Real-time data transfer occurred sporadically from the time of installation in early September 2004 until the WHOI buoy was recovered in June 2005 (Figure 5). Results from connectivity tests every half hour for several days after the hydronode deployment showed variability in the success and quality of data transmission with line of sight buoy to modem distance and buoy to modem bearing (Figure 6). In general, it appears that there is a sharp transition between successful and unsuccessful communications around a horizontal projection of buoy-modem distance of around 4200 meters, e.g. midday of 7 September 2004 and 10 September 2004. However, response success wasn't restored after the 7 September 2004 break until the morning of 9 September 2004 even though the distance is less than 4100 meters on the evening of the 8 September 2004. A good connection is reestablished on the morning of 9 September 2004, simultaneous with a major swing in the buoy from northwest of the modem to west-northwest of the modem. This corresponds to a 90° swing of the buoy around its anchor from east to south of the mooring.

Results from the flow sensors on the hydronode were transmitted to shore and available for download and processing from the WHOI website. The UW probes didn't detect any resistivity or heat anomalies. The OTIS transmittance record, rather than oscillating with each passing tracer pulse, decayed and flatlined at a value lower than possible (Figure 5), i.e. lower than the measured transmittance through 100% tracer

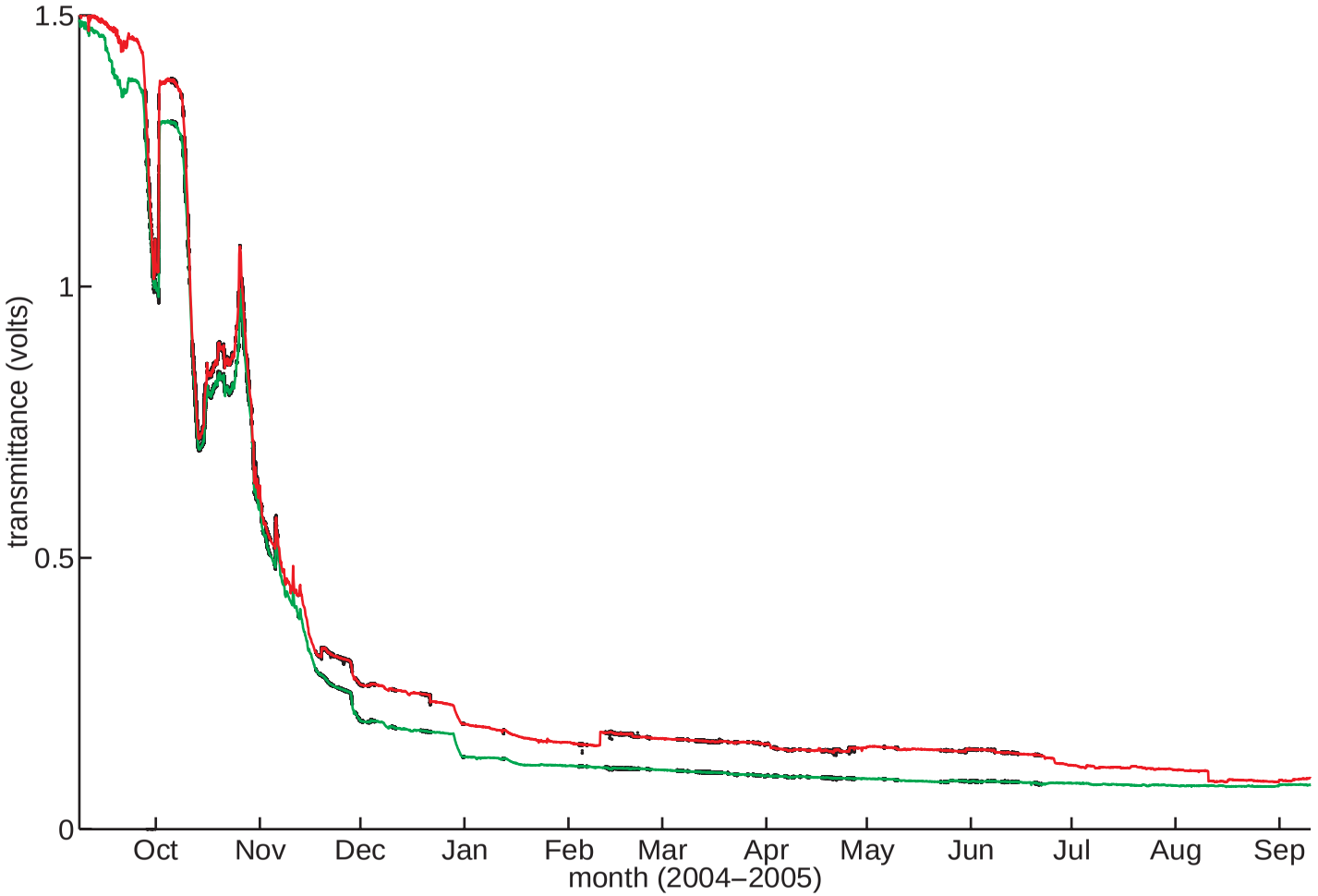

Figure 3-5. Time series of OTIS transmittance measurements on both sides of tracer injection location. Real-time transmitted data is plotted in black, and the complete record downloaded post recovery in red (downstream) and green (upstream).

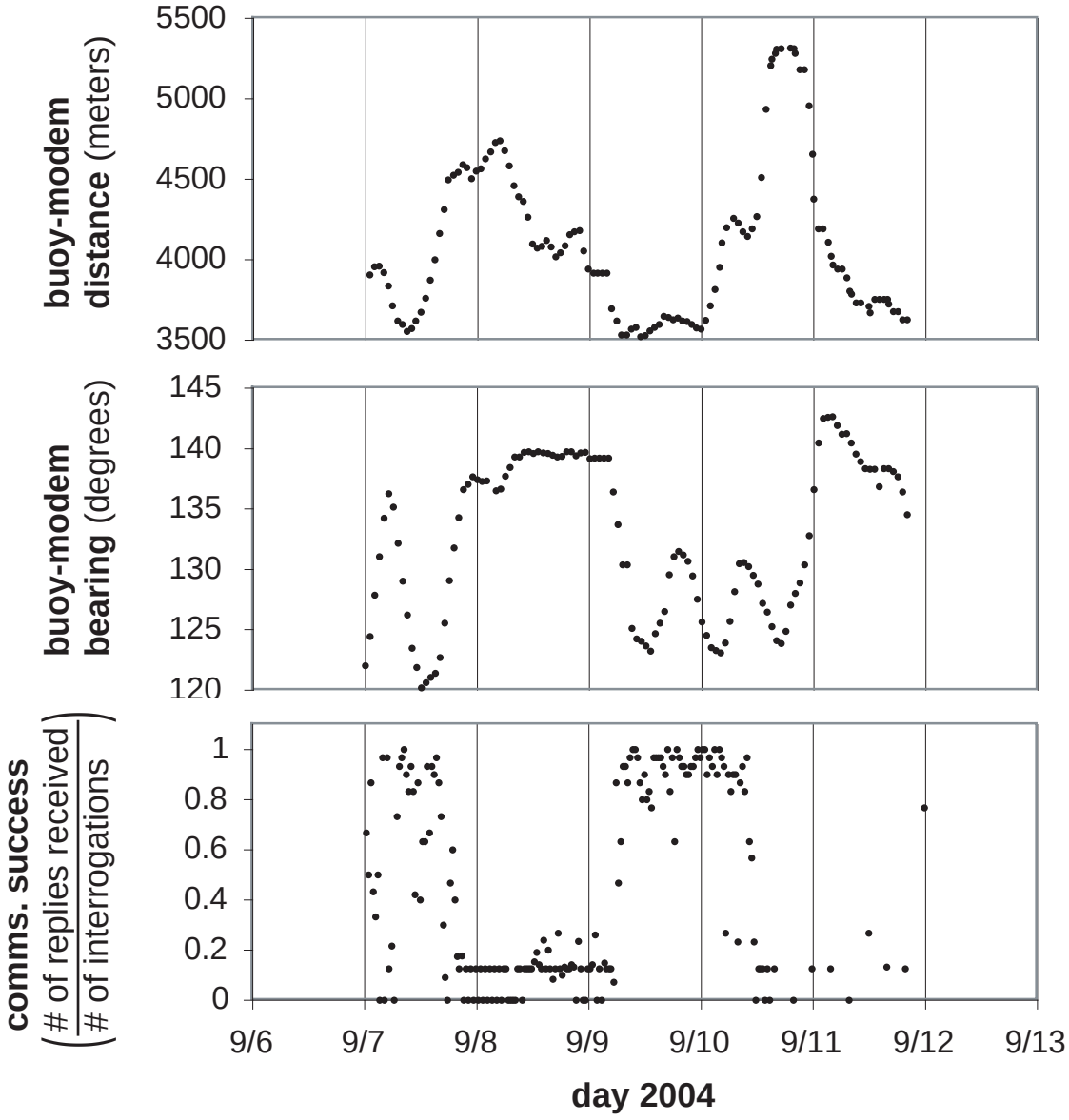

Figure 3-6. A comparison of buoy to hydronode modem communication success (bottom) with buoy to modem distance (top) and bearing (middle). The buoy interrogated the modem on the seafloor every half hour for the first five days after hydronode deployment. Data courtesy of the WHOI buoy team.

during pre-deployment calibration. A check of the logged LED reference values confirmed the LED intensities were stable and not the cause for decay. Another hypothesis for the observed decay was growth of bacterial matter between the LED and transmittance photodiode. A more fitting explanation is that particulate matter built up in the flow tube. Neither of these scenarios would render the OTIS data as useless since determination in flow rate is made by sensing relative changes in transmittance voltages with each passing tracer pulse, not by measure of absolute transmittance voltage. However, in this deployment we were also not able to detect the passing of the tracer pulse.

After recovery on 11 September 2005, we found the OTIS had ample power to supply the system for the entire year, even with the extra load on the battery from transferring data over the serial port to Nootka logger. The record on the onboard Flash Card was complete, and gaps in the transmitted record were filled (Figure 5). There was indeed evidence of particulate matter in the flow tube, and the solenoid pump responsible for injecting tracer pulses didn't function at depth, even though it worked on deck before and after the deployment. The best explanation for this malfunction to date is that vapor lock can occur between the outgoing check valve and the diaphragm when pressurizing the pump during descent in the off state (inlet valve closed). A solution is to frequently inject tracer pulses during descent (opening the inlet valve) and orient the outlet valve up so that internal air bubbles in the pump are simply displaced rather than trapped to create the vacuum.

3.5 Discussion

The acoustic modem and satellite transfer of data from the hydronode to the shore was a success. Analysis suggests that the success of buoy-modem communications may depend more on the buoy-modem bearing rather than the buoy-modem distance (Figure 6). Varying weather effects associated with particular wind directions, or bathymetric distances could conceivably control this apparent dependence on buoy-modem bearing.

The heat flow and resistivity probes were designed for flow rates typical of hydrothermal vent areas flowing kilometers per year, so it is not surprising they didn't register any anomaly in fluid flow at this site. The difficulties encountered with the OTIS instrumentation rendered the hydrologic data it gathered unreliable. It is possible that transients in the transmittance data (Figure 5) are associated with flushing events clearing particulate matter from the OTIS's flow detection cell. However, we have no way of constraining the magnitude of these events or even the direction of flow.

3.6 Conclusion

The Nootka Observatory test bed proved the functionality of a seafloor modem to surface buoy satellite connection for real-time data transmission. We expect to see use of similar observatory platforms during implementation of future ocean observatories. The WHOI system has improved data transfer rates as compared to older systems [*Suzuki*, 1989; *Suzuki et al.*, 1992]. Another major advantage of the WHOI system is the ease of adding sensors to the system since the Linux based controller of the buoy system can be remotely configurated and operated [*Frye et al.*, 2006].

With reasonable potential for failure of these types of systems in heavy weather, it is always necessary to include an onboard non-volatile store for independently logging a complete record of the data, like was done for the OTIS. This observatory test highlighted the benefit of real-time monitoring in the unfortunate case of instrument malfunction. By recognizing there is a problem soon after it occurs, attempts can be made to remotely, or while still on site, service the failed instrument and avoid the loss of a year's worth of data.

4. Nootka Hydro-tectonic Experiment

The second component of the Nootka study is designed to satisfy our scientific objective. To address the relationship of flow and regional tectonics, we deployed seven flow meters: two along the Nootka transform fault and five on the toe of the Cascadia subduction zone complex just south of the junction with the Nootka fault (Figure 2). Three short period seismometers and one broadband seismometer were also deployed in the area.

The three short-period seismometers: KNCP, KNNE, and KNNW; and one broadband seismometer, KNBB, were deployed in the area prior to our September 2004 deployment cruise. MBARI developed the short-period seismometers that have a frequency response of 1-100 Hz. The data loggers with ample storage space and high amp-hour lithium batteries allow the system to run for over 12 months. Guralp Systems Ltd. broadband sensors with a frequency range between 2.8 mHz and 100 Hz were purchased and packaged by MBARI.

The flow meters used were CAT meters, small, easy to deploy, and low cost flow meters developed in the Hydrogeology and Tectonic Studies laboratory (HTS) at SIO [*Tryon et al.*, 2001]. The CAT meter can make long-term measurements of fluid flow, quantifying both inflow and outflow rates on the order of 0.01 to 1500 cm/yr. A serial record of the fluid chemistry is also collected. During CAT meter deployment an external chamber is pushed into the sedimented seafloor. Flow is focused through the outlet tubing connected to this chamber. A Sc-Rb tracer solution is injected into the outlet tubing at a constant rate by two osmotic pumps. These same pumps withdraw a sample of the seep fluid and tracer mixture from either side of the tracer injection port into a ~100 m coil of sample tubing, thereby obtaining a serial record of the tracer dilution. Flow rate through the outlet tubing, and thus flux through the seep, is determined by measuring the dilution of the chemical tracer. The CAT II contains two independent CAT flow meters as described previously, however, the upstream sample is collected in gas-tight copper coils that are maintained at ocean bottom pressure during recovery allowing for analysis of the gas content of the samples. The CAT packaged in the hydronode is also one that collects a gas-tight time series of fluids on the upstream side. All the CAT meters were prepared for the yearlong deployment by setting the osmotic pump to approximately one milliliter per day.

Regional currents and oceanographic effects causing variation in pressure gradients at the seafloor are a possible cause of temporal variation in flow rate through the seafloor. To ensure flow events are actually a result of sub-seafloor pressure changes, we deployed an Acoustic Doppler Current Profiler (ADCP) and Bottom Pressure Recorder (BRP) at the site. The current profiler, a specialized version of the

Sontec Argonaut MD redesigned with new electronics and larger transducers was included in the CAT II package. It was programmed to take a 3-D velocity measurement and a temperature measurement every 5 minutes. The Bottom Pressure Recorder developed in the HTS laboratory measures pressure at a precision of 1 mm water depth and accuracy of 25 cm using a Paroscientific 46k-101 pressure transducer. Every 5 minutes a Persistor CF2 computer logs the pressure along with temperature at ± 0.001°C precision.

The five flow meter instruments were installed in September of 2004 near the triple junction at seeps with different geologic and biologic characteristics (Figure 7). On 4 September 2004, the CAT II, BPR, CAT 6 and CAT 13, and a locating transponder were loaded onto a biodegradable descender platform and deployed over the side of the ship at the seep location. The Remotely Operated Vehicle (ROV) Ropos navigated to the descender platform perched precariously on a steep slope of the seafloor, removed the BPR and deployed it near a seep site dense with clams. The CAT II was deployed at this clam site with one chamber (10) on a clam patch and the other (11) between the first and a second clam patch (Figure 7). CAT 6 was deployed at small dense clam patch ten meters to the west-northwest. Its external chamber was nestled in with the clams. CAT 13 was deployed on a small bacterial mat. During the next ROV Ropos dive on 6 September 2004, the hydronode, with its built in CAT 17, was deployed at the tubeworm and bacterial mat site ~70 meters to the east. Where necessary, biology (e.g. clams, tubeworms) were cleared aside from the seep site with the ROV to enable the flow meter collection chambers to be pushed into a soft sediment substratum to form a proper seal.

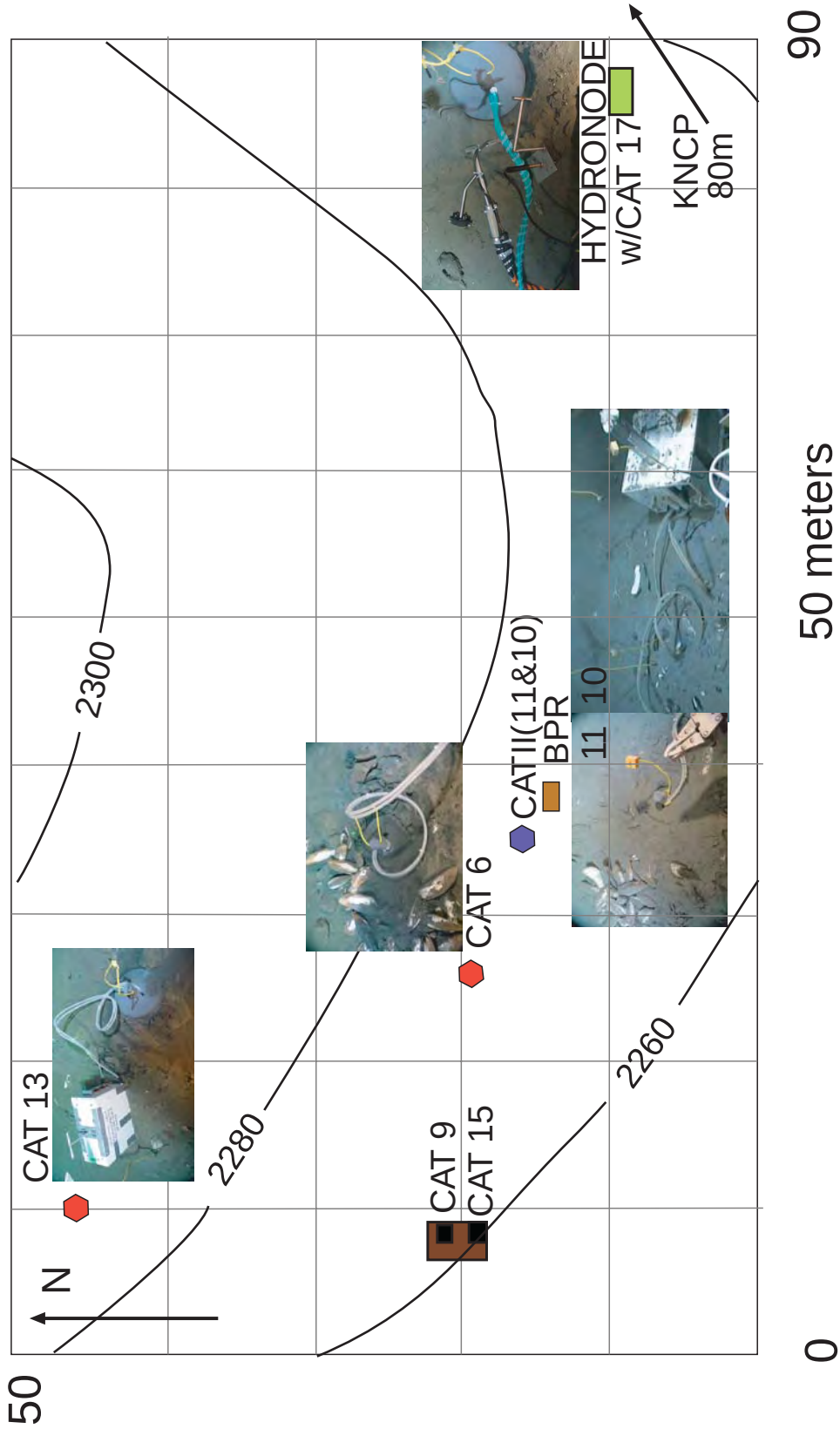

Figure 3-7. Detailed layout of the Nootka seep site instrument locations including seep site pictures. Picture of CAT II chamber 10 is from the recovery dive. Original placement of chamber 10 was amidst clams. Clams had dispersed or died between the time of flow meter deployment and recovery.

ROV operations ceased on 6 September 2004 when the weather picked up. CAT 9 and CAT 15 that had been sent to the bottom on another biodegradable descender were not deployed. Deployment of two more CAT meters rigged for launch from the ship and self-deployment at the seafloor could still be done in the heavy weather. These two CAT meters were dropped from the side of the ship over what was believed to be a mud volcano along the Nootka transform fault. Such a geologic feature is believed to have regional diffuse flow, and the need to carefully place the instrument at a seep site is eliminated.

All of the seven instrument packages were successfully recovered on a September 2005 cruise. The two self-deployed CAT meters along the Nootka transform fault were triggered to drop their ballast weight by acoustic communication and released to the surface for recovery. ROV Jason recovered the five instruments at the Nootka-Cascadia junction. CAT meters were turned off and stored on the ship until offloaded in San Diego two months later. Current and BPR data were downloaded from their internal data store for time series analysis. Data from the three short-period seismometers were downloaded upon their recovery. The Gulrap Broadband seismometer was also recovered from the Nootka site. In May 2006 the CAT meter coils were dispensed into 1 or 2 ml volumes and a subset of the samples were diluted 1 to 100 for tracer and major seawater ion concentration analysis. While the sampling frequency is 0.5 to 1 samples per day, the temporal resolution is typically lower and variable due to residence time and tracer mixing in the outlet tubing. The subset was analyzed for the Sc and Rb tracers and major ion concentrations (Ca, Mg, S, K, B, Li, Sr) using Inductively Coupled Plasma Optical Emission Spectrometry (ICP-OES). Analysis of a complete

sample set for a section of the time series showed the subset of samples analyzed adequately represents changes in the record. Determination of flow rates involved a calculation of the required volume of seep fluid mixed with tracer to result in the measured tracer concentration [*Tryon et al.*, 2001].

5. Results

Six of the seven deployed CAT meters collected a time series of fluids by which relative flow rates through the seafloor could be determined. The sample record from the two CAT meters deployed at the "mud volcano" showed the signature of oscillating inflow and outflow, i.e. tracer was detected on both sides of the injection location. These data simply demonstrate that the flow through the seafloor at this location is solely a response to the oscillating ocean tides and will not be further discussed.

Of the five instruments at the Nootka-Cascadia triple junction site the upstream coil of CAT 13, and the downstream coil of CAT 10, withdrew sample at a slower rate, 0.14 ml/day and 0.21 ml/day respectively, than the 1 ml/day rate at which the osmotic membrane was designed to pump. We observed that a valve on CAT 13 was faulty and causing a restriction of flow. Measured tracer concentrations for the 53 ml of sample collected in the upstream coil are below the error range for the analytical technique. Data from CAT 13 is therefore discarded. A kink in the CAT 10 downstream coil appears to have caused its low intake rate. Fortunately, the measured tracer concentrations register above the range of error. However, at such a low pump rate diffusion processes cause significant concern: the tracer concentrations may be systematically low and the temporal resolution of the record is severely compromised.

The data set is still valuable for interpretation of relative flow rates. The flow rate time series for CAT 10 and the other three functional CAT meters at the Nootka-Cascadia triple junction are plotted in Figure 8a.

We used rubidium percentages obtained from the ICP-OES analyses to determine flow rates using the tracer dilution method. With analytical chemistry results we were also able to identify the presence of pore fluids with altered chemistries in CAT 6 on 18 February 2005 and 13 March 2005 through 29 April 2005 with low calcium, sulfur and magnesium values of 3, 14.5, and 48.7 respectively. The altered chemistry on 18 February 2005 is a pulse, and likely associated with a short-lived event. Assuming the outflow during this time is short-lived, the magnitude of outflow using the CAT tracer dilution method for the 18 February 2005 event is an approximation and is dashed in Figure 8a.

A check for altered chemistry on CAT flow meters 10, 11, and 17 yielded no conclusive results. These three meters had copper coils for gas sampling. Copper reacts with the sulfates in pore fluids (Geoff Wheat personal correspondence) and potentially other unknown chemical reactions are occurring. The upstream coil fluid chemistries are thus unrepresentative of true chemistries and these data are discarded.

The BPR and current meter collected data with 5-minute resolution. While the BPR ran for the entire yearlong deployment, the current meter only recorded data for the first third of the deployment before exhausting its power supply on 20 January 2005.

6. Discussion

Figure 3-8. A) Time series of flow rates from the four functional CAT meters at the Nootka seep site. To adequately view relative changes in the records with both upflow and downflow, flow rates are plotted on a log scale with a minimum of 0.1 cm/yr. The downflow log plot was inverted and positive and negative flow rates with magnitude 0.1 were plotted on the axis and set to zero. Periods that the instruments recorded oscillating tidal flow are indicated by rectangles plotted on the axis. Transitions between tidal flow, upflow, and downflow are dashed due to the approximate handpicked location of these transitions. CAT 10 (green) with the low sample intake rate is dashed, and the flow rate at CAT 6 on 18 February 2005 is also an approximation. B) Bottom Pressure Recorder time series detrended to remove pressure sensor drift and bandstop filtered between a few hours and 18 days to remove lunar effects. Of the spikes in the record at least a couple correspond with seismic activity, see insets of change in water column height per measurement on 2 November 2004 and 25 December 2004. Times are in local PST.

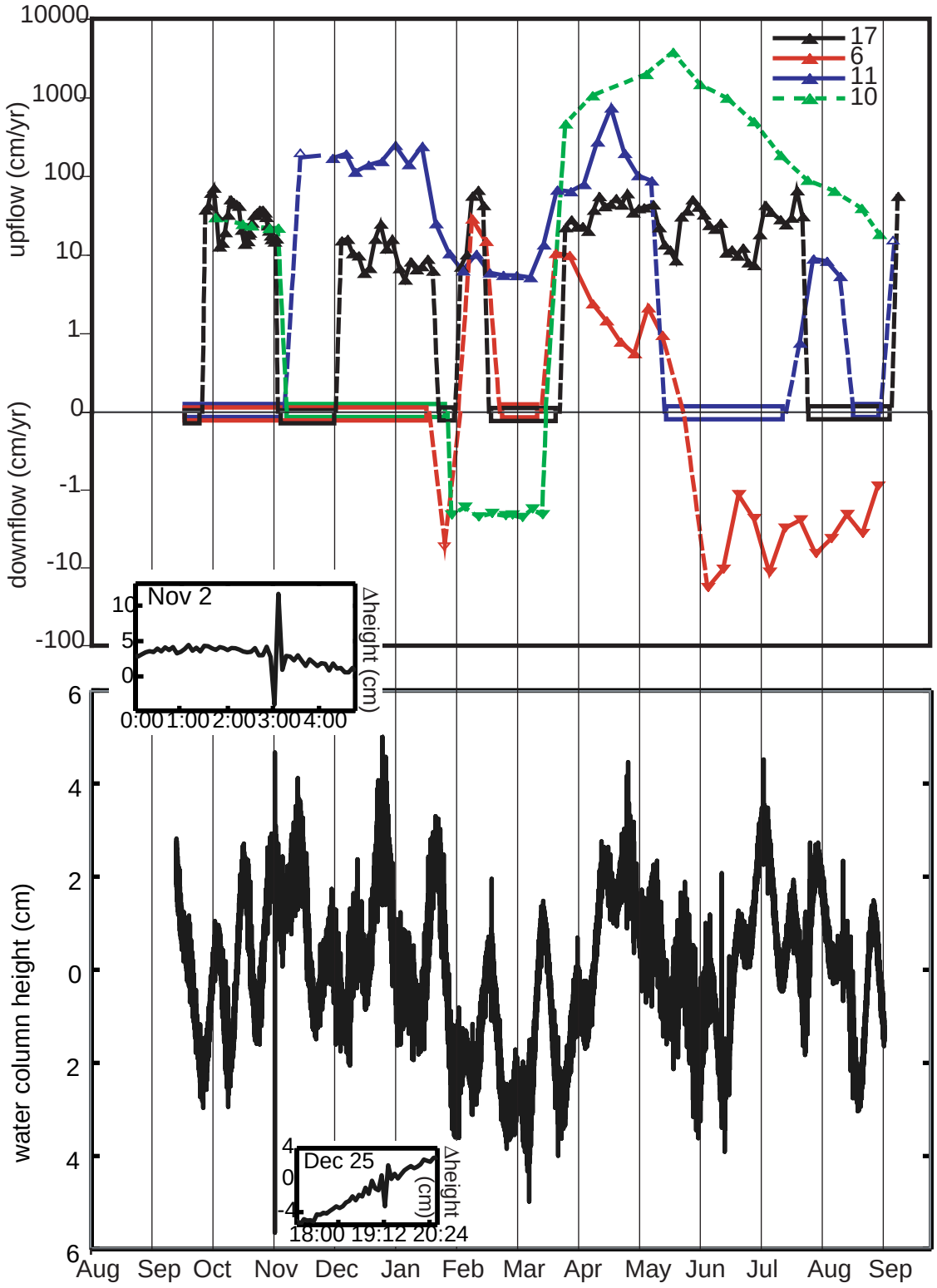
10000
1000
100
10
1
0
-1
-10
-100
upflow (cm/yr)
downflow (cm/yr)
17
6
11
10
Nov 2
10
5
0
Δheight (cm)
0:00 1:00 2:00 3:00 4:00
6
4
2
0
2
4
6
water column height (cm)
Dec 25
4
0
-4
Δheight (cm)
18:00 19:12 20:24
Aug Sep Oct Nov Dec Jan Feb Mar Apr May Jun Jul Aug Sep

This first yearlong deployment of the CAT meters and BPR yielded a substantial dataset. By comparing the flow rate datasets with the pressure data, a land based seismic network database, and the MBARI/Keck offshore seismic array, we evaluate mechanisms that could drive the observed relative flow rate changes. Because the flow rates can vary by several orders of magnitude over very short distances [*Tryon et al.*, 2002], and the primary goal of this study was to evaluate the relationship of transient fluid flow and deformation events, an interpretation of the differences in absolute flow rates between the seep sites is not included.

Observed changes in flow rates are potentially a result of changes in pore pressure from static and/or dynamic strain associated with deformation events, or changes in the permeability of the seep structures. Dynamic strain could generate anomalous flow rates through processes such as liquifaction, consolidation or triggered gas hydrate dissociation depending on the characteristics of the substrate at the instrument site. Changes in permeability of the seep structure would induce changes in flow rate patterns that are unique and only observed by instrumentation at that particular seep. However, regional deformation in response to static strain is more likely to result in flow rate patterns that agree across the study site. We investigate such events where all four of the functioning CAT meters have similar relative flow rate patterns, for instance, the increase observed in mid March (Figure 8a). After first eliminating bottom currents and oceanographic pressure effects as potential causes for regionally coincident flow rates, we compare the flow record with seismic data to test whether these events are a result of seismically generated static strain, or alternatively, a result of aseismic deformation.

Although the flow rate time series data from the osmotically driven CAT meter lacks the temporal resolution to perform a cross-correlation analysis between the current and flow rate data, we can conclude a lack of correlation by comparison to results from a recent study using a similar sized electronic OTIS instrument package deployed at a seep site in Monterey Bay. The Monterey site, with larger average current speeds than and similar variance to the currents recorded at the Nootka site, showed no correlation to recorded flow rates [*LaBonte et al.*, 2007]. Changes in the Nootka flow rate records are thus not a result of local pressure highs and lows created by currents flowing around the instrument package.

Just like overburden pressures from ocean tides drive flow through the seafloor, longer period oceanographic effects, such as shifts in the Alaska and West Wind Drift currents that diverge to the north and south off the coast of Vancouver Island, could potentially cause flow into and out of the sediments. The longer period variations in the BPR record after filtering out tidal oscillations measures five centimeters in peak-to-peak change in water height (Figure 8b). Flow rates resulting from an overburden of this amplitude can be calculated using the analytical solution for change in pore pressure with depth in permeable sediments under periodic loading [*Wang and Davis*, 1996]. We find that the low frequency changes in overburden pressure drive less than one centimeter per year of flow, insignificant in comparison to absolute flow rates observed at the seep site. Furthermore, theory predicts maximum downflow occurs during periods of increasing overburden pressure [*Jupp and Schultz*, 2004], for example in early April, but the contrary is observed at this time in the flow rate record (Figure 8).

To examine for flow rate response to tectonic deformation, a search of the Canadian National Seismographic Network (CNSN) earthquake database for seismic events during the deployment in a 5° latitude by 10° longitude area centered around the seep site was conducted. Seismic activity during the year was frequent: 1350 events, 238 of which were magnitude 3 or greater. Furthermore, a magnitude 5.0 earthquake occurred on 28 February 2005, the third day of a swarm that continued for a total of seven days at the northern end of the Endeavor mid-ocean ridge segment [*Hooft et al.*, 2006], and a magnitude 6.6 ruptured intra-Explorer-plate on 2 November 2004. Focal mechanisms obtained from the Harvard Centroid Moment Tensor (CMT) catalogue for these two events are displayed in Figure 1. Without the moment tensor solution for the remaining events, theoretical strain fields and predictions of pore pressure changes at the instrumented sites cannot be calculated. Instead, we calculate the amplitude that the CNSN events would measure on a seismometer located at the seep site by solving the Richter local magnitude (M_L) empirical equation [*Bullen and Bolt*, 1985] for A, the displacement amplitude of a hypothetical local seismometer:

$$M_L = \log_{10}A + 2.56\log_{10}\Delta - 1.67, \quad (1)$$

where Δ is source-receiver range in kilometers. Measurements of A plotted against the flow rate record (Figure 9) allow for comparison of the seismic moments corrected for distance from the seep site, a proxy for local strain, to flow rates measured at the seep site.

Figure 3-9. Flow rate data from Figure 8 with displacement amplitudes, *A,* of a hypothetical seismometer at the Nootka seep site plotted on a log scale and sharing the same X axis (time) as the flow rate data. Note that these are underestimates as the M_L values off Vancouver Island are approximately 0.6 magnitude units low [*Ristau et al.*, 2003]. Local moments from CNSN database events located in the 5° latitude by 10° longitude area are plotted. Large events recorded on the local short-period seismometer array that didn't show up in the CNSN database are plotted as a grey vertical line that we plot off scale as we don't know the seismic moment from the unprocessed data set.

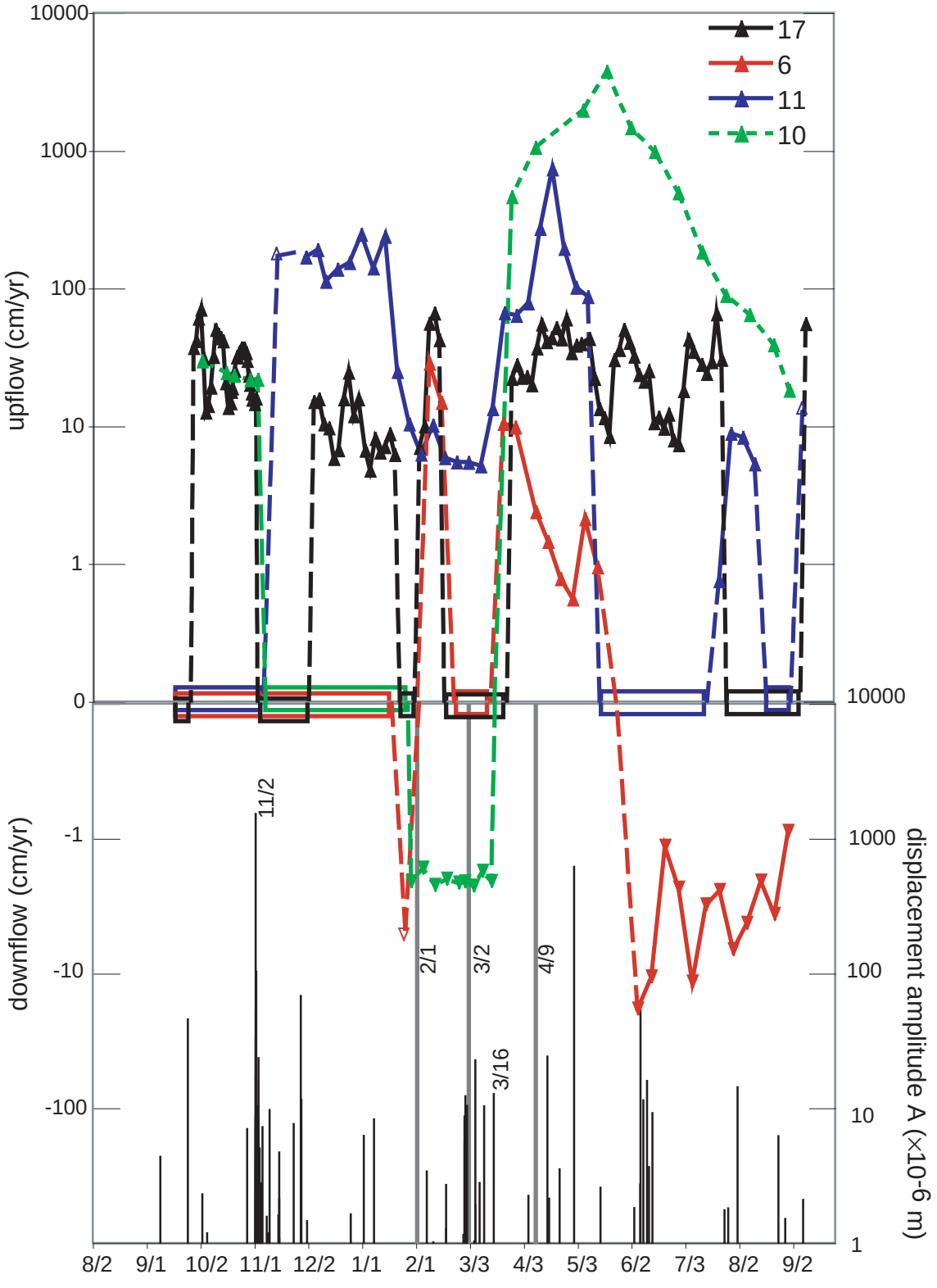
10000
1000
100
10
1
0
-1
-10
-100
upflow (cm/yr)
downflow (cm/yr)
17
6
11
10
11/2
2/1
3/2
3/16
4/9
10000
1000
100
10
1
displacement amplitude A (×10-6 m)
8/2
9/1
10/2
11/1
12/2
1/1
2/1
3/3
4/3
5/3
6/2
7/3
8/2
9/2

Static strain from the 28 February 2004 Endeavor swarms that originated 173-222 km south-southwest of the Nootka seep sites may be a cause for the sustained relatively low flow rates observed on all four instrument records during the late February to early March time period. The focal mechanisms for the events during this swarm are strike slip with a dilational 0° to 90° quadrant (Figure 1). This dilational sense of strain from the swarm agrees with the relatively low flow rates in all four records at this particular time. During the two weeks following the swarm the CNSN database lists three relatively large events and the flow rates remain low.

The last of the three large events following the February earthquake swarms was a magnitude 4.5 earthquake that occurred further north on the ridge on 16 March 2005. This event, located only 95 km distant from the seep site coincides with a jump in the flow rates measured at all of the instruments. The time scale for CAT meter records, unlike the electronic OTIS meter used for the real-time acoustically linked moored-buoy observatory, is constrained solely by the time the meters' valves were switched on and off at the beginning and end of the deployment. It is assumed that the osmotic pump rate is constant over the entire year duration, and by interpolating between the two endpoints, individual samples are assigned a time. For this yearlong deployment the temporal accuracy could be off by over a week in the middle of the record and less at the ends. Because of this error in the CAT time scale, it is possible the outflow began at the same time as the rupture at all four seep sites. The mechanism causing the increased outflow at all of the sites is likely a result of a transient deformation coinciding with the 16 March 2005 earthquake.

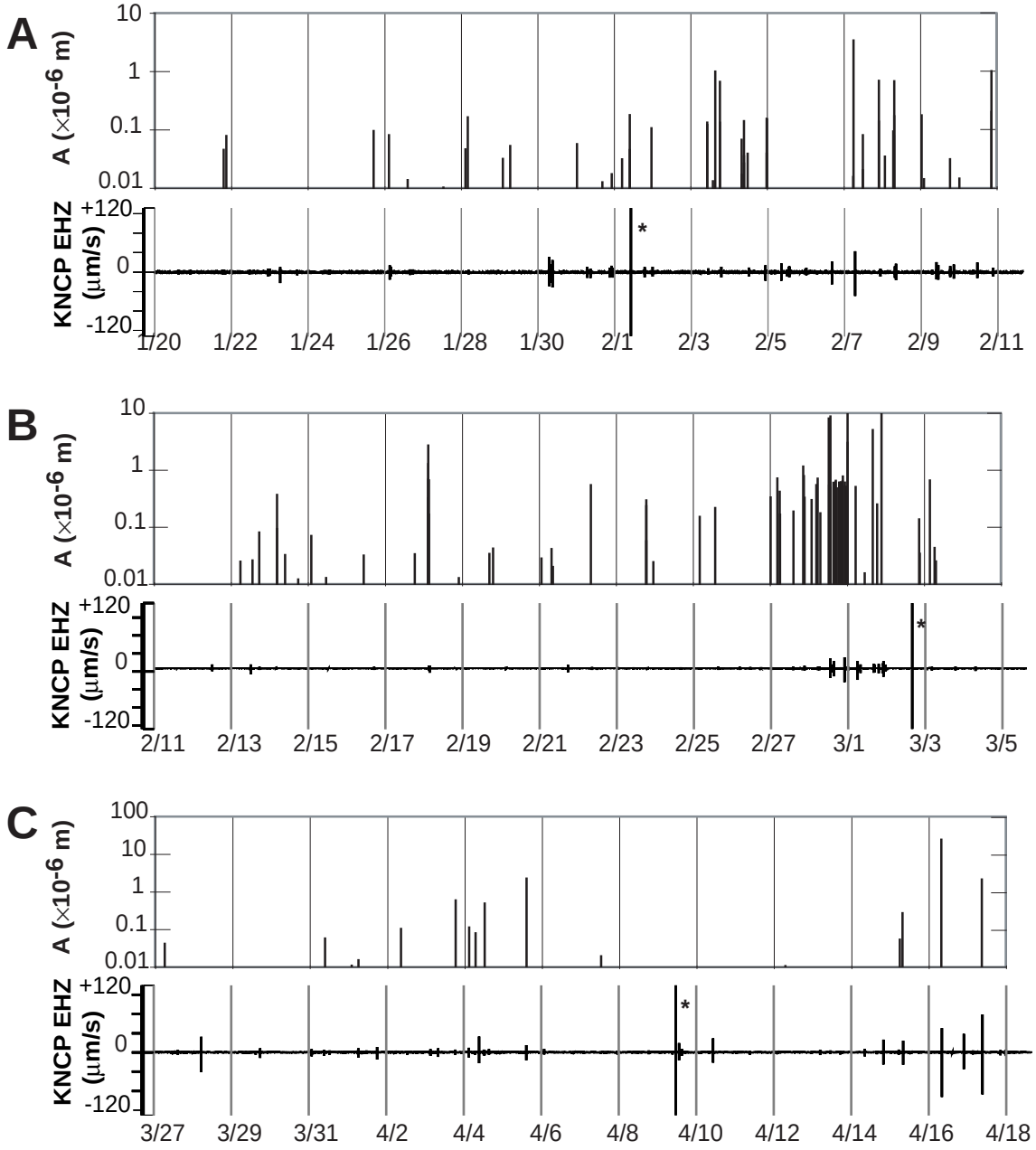

Figure 3-10. A comparison of hypothetical displacement amplitudes of events that registered in the CNSN database (top) and horizontal velocities recorded on KNCP, the closest short-period seismometer approximately 80 meters distant (bottom). Asterisk identifies off-scale events recorded on the local seismometer on A) 1 February 2005, B) 2 March 2005, and C) 9 April 2005 [courtesy of E. Hooft].

There are also flow events captured by the four instruments for which there is no concurrent seismic activity in the CNSN database and alternative explanations such as local seismicity or aseismic activity must be considered. An example is the dip-down and spike-up in all four flow-rate records prior to the Endeavor swarms (Figure 9). We viewed the 3 Hz high pass filtered data [courtesy of E. Hooft] from the three short-period stations, KNCP, KNNW, KNNE, between 20 January 2005 and 18 April 2005 and identified three events as significant and absent from the CNSN earthquake database (Figure 9,10). On 1 February 2005 readings on the KNCP seismometer less than 100 meters distant were maxed out (Figure 10a). A coincident earthquake registered in the database was located at 143 km distant to the south-southwest of the Nootka triple junction, near the northern end of the Endeavor mid-ocean ridge segment. Because the amplitude of the event is only off scale at the local KNCP seismometer, and not at the KNNW and KNNE seismometers, the KNCP seismometer is likely responding to a separate and local deformation event. Measurements on all three seismometers had railed for the 2 March 2005, and 9 April 2005 events and no coincident earthquakes were recorded in the database (Figure 10a,b). The explanation for the discrepancy between the offshore and shore-based arrays is that west of the North American-Juan de Fuca plate junction, the CNSN database is only complete for earthquake magnitudes over 3.5. The magnitude for these three events is thus less than 3.5. For a small earthquake to exceed the limits of the seismometer measurements, the earthquakes must be relatively local events. An accurate location could be calculated from the P-S times recorded on the three short-period and one broadband seismometer

when that data becomes available. No vertical step of the seafloor was detected by the BPR above its one-centimeter resolution.

The dip-down or spike-up in the flow rate records prior to the swarm might be associated with the local 1 February 2005 event. Aseismic deformation is also a plausible mechanism for the flow events. Because the pattern is similar across all instruments, the sense of strain resulting from the deformation events is similar throughout the region. It is likely the slip surfaces do not break the surface in the seep area because zones of both high and low pressure would result on either side of the fault surface and the flow meters, depending on their location relative to the fault, would respond in different senses. Perhaps activity on the decollement, a subsurface fault separating the frontal wedge from the subducting Juan de Fuca plate, is responsible for the regional flow pattern. Stable sliding along the decollement updip of the seismogenic zone is aseismic [*Hyndman et al.*, 1993; *Hyndman et al.*, 1997; *Brown et al.*, 2003; *Brown et al.*, 2005; *Davis et al.*, 2006]. The requirement that a local seismic event agrees with the timing of the flow events is therefore eliminated. Finally, the dip-down followed by a spike-up pattern could be explained as different segments of the decollement sliding consecutively.

The 2 November 2004 earthquake is the largest recorded seismic event that occurred in the region. Flow rates recorded on CAT 17 and CAT 10 exhibit a decrease, and CAT 11 an increase (Figure 9). However, the focal mechanism for this magnitude 6.6 event that occurred 97 kilometers away predicts that the entire seep area is under compression and outflow should occur at all of the sites if the flow response is purely due to static strain from this distant earthquake. However, a supposed fracture providing

fluids to the instrumented seep could conceivably be oriented in a fashion that allows for dilation on the particular fracture segment. Alternatively, permeability changes could be the cause of the relative inversion in flow rates between CAT II chambers 10 and 11, which lie in very close proximity. Shaking could have resulted in a shift of the primary pathway for focused fluid outflow from the seep under chamber 10 to the seep close to chamber 11. This may also explain why the live clams surrounding meter 10 at deployment were no longer living at the site upon recovery (Figure 7).

Such a large magnitude could have triggered coseismic local deformation events, and flow at the seep sites are perhaps in response to strains resulting from simultaneous local events. No evidence of a local vertical offset corresponding to the 2 November 2004 earthquake was found in the BPR data (Figure 8 inset). The pressure returns to its background state after the event, and vertical displacement of the seabed, if any, is less than the instrument resolution of approximately one centimeter. Local strike-slip faulting could result in both increase and decrease of measured flow rates in the area without vertical deformation. Ultimately, we are not able to constrain the relationship between the 2 November 2004 mid-Explorer plate earthquake and the flow events on the toe of the accretionary wedge at the Nootka-Cascadia triple junction.

Upon inspection of the pressure data, a curious anomaly at the time of the 2 November 2004 earthquake presented itself. I am unable to determine the mechanism causing the anomaly as the BPR only samples once every five minutes, and each sample is an average over seven seconds. A dynamic process is possibly the cause for the pressure spikes. The passing of surface waves from the nearby 2 November 2004 event could result in an impulse signal, however, these surface waves pass relatively quickly,

and the signal captured by the BPR lasts for over five minutes. The anomaly is potentially a pressure wave, or 'T-phase', moving through the SOFAR channel at the speed of sound and long enough to be sensed by the BPR. For example, the Sumatra earthquake produced a 'T-phase' that lasted ~800 seconds [*Tolstoy and Bohnenstiehl*, 2006]. The predicted time for a wave traveling at 1.5 km/s to arrive at Nootka, a great circle distance of 12820 km away, is 142 minutes, reasonably close to the measured 134 minute delay before a pressure anomaly, similar to the 2 November 2004 anomaly, was recorded on the BPR (Figure 8 inset).

7. Conclusion

Studies employing both instruments that can detect seismic and aseismic deformation events are important to address dynamics of subduction zones during the interseismic period. The OTIS and CAT flow meter instruments developed in the Hydrogeology and Tectonics Studies laboratory at SIO have both been successful during this study in their different ways. The CAT meter instrument was able to resolve low flow rates at these low-to-moderate flow-rate seeps that have periods of little-to-no flow. However, the inaccuracy of the timing of the flow events makes it difficult to constrain whether seismic events in the seismometer array records are simultaneous and potentially correlated or not. The OTIS meter recorded transmittance data digitally so each record in the data series had an accurate time stamp, and the data could be transmitted real-time. A combination of the two positive aspects of the CAT and OTIS in a modified instrument would be ideal for future studies of subduction zone dynamics.

This study highlighted that the Juan de Fuca plate, particularly the Nootka-Cascadia junction is hydrologically active as well as seismically active. Local events, that appear to correlate with some of the regional flow events, were detected with the offshore seismometer array. Other regional flow events that aren't concurrent with any seismic activity are potentially a result of aseismic activity. Future deployments would ideally include instrumentation for detecting aseismic deformation, such as seafloor marine geodetic installations for continuously monitoring seafloor movement, in addition to our current instrumentation for detecting flow rate changes resulting from pore pressure transients.

Results of these studies are promising. Continued use of flow rate and pressure monitoring instruments alongside GPS and seismic arrays will help fill out temporal and spatial scales. Observatories will be invaluable in the collection of these empirical measurements. Ultimately, constraints of models of subduction zone dynamics and the earthquake cycle in these areas that pose significant seismic hazards can be made.

References

Brown, K.M., A. Kopf, M.B. Underwook, and J.L. Weinberger (2003), Compositional and fluid pressure controls on the state of stress on the Nankai subduction thrust: A weak plate boundary, *Earth and Planetary Science Letters*, *214*, 589-603.

Brown, K.M., M.D. Tryon, H.R. DeShon, L.M. Dorman, and S.Y. Schwartz (2005), Correlated transient fluid pulsing and seismic tremor in the Costa Rica subduction zone, *Earth and Planetary Science Letters*, *238*, 189-203.

Bullen, K.E., and B.A. Bolt (1985), *An Introduction to the Theory of Seismology*, Cambridge University Press, Cambridge.

Byrne, D.E., D.M. Davis, and L.R. Sykes (1988), Loci and Maximum Size of Thrust Earthquakes and the Mechanics of the Shallow Region of Subduction Zones, *Tectonics*, *7*, 833-857.

Davis, E.E., K. Becker, K.L. Wang, K. Obara, Y. Ito, and M. Kinoshita (2006), A discrete episode of seismic and aseismic deformation of the Nankai trough subduction zone accretionary prism and incoming Philippine Sea plate, *Earth and Planetary Science Letters*, *242*, 73-84.

Davis, E.E., D.S. Chapman, C.B. Forster, and H. Villinger (1989), Heat-Flow Variations Correlated with Buried Basement Topography on the Juan-De-Fuca Ridge Flank, *Nature*, *342*, 533-537.

Davis, E.E., K. Wang, R.E. Thomson, K. Becker, and J.F. Cassidy (2001), An episode of seafloor spreading and associated plate deformation inferred from crustal fluid pressure transients, *Journal of Geophysical Research-Solid Earth*, *106*, 21953-21963.

DeMets, C. (1990), Current plate motions, *Geophysical Journal International*, *101*, 425-478.

Dragert, H., K. Wang, and G. Rogers (2004), Geodetic and seismic signatures of episodic tremor and slip in the northern Cascadia subduction zone, *Earth Planets and Space*, *56*, 1143-1150.

Dragert, H., K.L. Wang, and T.S. James (2001), A silent slip event on the deeper Cascadia subduction interface, *Science*, *292*, 1525-1528.

Freitag, L., M. Johnson, and D. Frye (2000), High-rate acoustic communications for oceanobservatories-performance testing over a 3000 m vertical path, in *OCEANS 2000 MTS/IEEE Conference and Exhibition*, pp. 1443-1448, Providence, RI.

Frye, D., L. Freitag, R. Detrick, J. Collins, J. Delaney, D. Kelley, A. LaBonte, and K. Brown (2006), An Acoustically-Linked Moored-Buoy Ocean Observatory, *Eos Trans. AGU*, *87*(22), 213.

Fujita, M., T. Ishikawa, M. Mochizuki, M. Sato, S. Toyama, M. Katayama, K. Kawai, Y. Matsumoto, T. Yabuki, A. Asada, and O.L. Colombo (2006), GPS/acoustic seafloor geodetic observation: method of data analysis and its application, *Earth Planets and Space*, *58*, 265-275.

Gagnon, K., C.D. Chadwell, and E. Norabuena (2005), Measuring the onset of locking in the Peru-Chile trench with GPS and acoustic measurements, *Nature*, *434*, 205-208.

Goldfinger, C., C.H. Nelson, and J.E. Johnson (2003), Holocene earthquake records from the Cascadia subduction zone and northern San Andreas Fault based on precise dating of offshore turbidites, *Annual Review of Earth and Planetary Sciences*, *31*, 555-577.

Hooft, E., H. Patel, W. Wilcock, H. Berkenbosch, D. Toomey, E. Davis, D. Butterfield, R. Dziak, and M. Fowler (2006), Spatial and Temporal Seismicity Patterns and Associated Vent Temperature and Borehole Pressure Perturbations of the February/March 2005 Swarm on the Endeavour Segment, Juan de Fuca Ridge, *Eos Trans. AGU*, *87*(52), Abstract B33D-07.

Hyndman, R.D., R.P. Riddihough, and R. Herzer (1979), Nootka Fault Zone - New Plate Boundary Off Western Canada, *Geophysical Journal of the Royal Astronomical Society*, *58*, 667-683.

Hyndman, R.D., and K. Wang (1995), The Rupture Zone of Cascadia Great Earthquakes from Current Deformation and the Thermal Regime, *Journal of Geophysical Research-Solid Earth*, *100*, 22133-22154.

Hyndman, R.D., K. Wang, T. Yuan, and G.D. Spence (1993), Tectonic Sediment Thickening, Fluid Expulsion, and the Thermal Regime of Subduction Zone Accretionary Prisms - the Cascadia Margin Off Vancouver-Island, *Journal of Geophysical Research-Solid Earth*, *98*, 21865-21876.

Hyndman, R.D., M. Yamano, and D.A. Oleskevich (1997), The seismogenic zone of subduction thrust faults, *Island Arc*, *6*, 244-260.

Jupp, T.E., and A. Schultz (2004), A poroelastic model for the tidal modulation of seafloor hydrothermal systems, *Journal of Geophysical Research-Solid Earth*, *109*, B03105, doi:10.1029/2003JB002583.

Kao, H., S.J. Shan, H. Dragert, G. Rogers, J.F. Cassidy, and K. Ramachandran (2005), A wide depth distribution of seismic tremors along the northern Cascadia margin, *Nature*, *436*, 841-844.

Kelley, D., K. Raybould, and W. Wilcock (2006), Regional cabled conceptual network design for ORION's Ocean Observatories Initiative (OOI), pp. 73, ORION Project Office, Washington, D.C.

LaBonte, A., K. Brown, and M. Tryon (2007), Monitoring periodic and episodic flow events at Monterey Bay seeps using a new optical flow meter, *Journal of Geophysical Research*, *112*, B02105, doi:10.1029/2006JB004410.

Mazzotti, S., H. Dragert, J. Henton, M. Schmidt, R. Hyndman, T. James, Y.A. Lu, and M. Craymer (2003), Current tectonics of northern Cascadia from a decade of GPS measurements, *Journal of Geophysical Research-Solid Earth*, *108*, 2554, doi:10.1029/2003JB002653.

Mazzotti, S., H. Dragert, R.D. Hyndman, M.M. Miller, and J.A. Henton (2002), GPS deformation in a region of high crustal seismicity: N. Cascadia forearc, *Earth and Planetary Science Letters*, *198*, 41-48.

Miyazaki, S., J.J. McGuire, and P. Segall (2003), A transient subduction zone slip episode in southwest Japan observed by the nationwide GPS array, *Journal of Geophysical Research-Solid Earth*, *108*, 2087, doi:10.1029/2001JB000456.

Moore, J.C., and D. Saffer (2001), Updip limit of the seismogenic zone beneath the accretionary prism of southwest Japan: An effect of diagenetic to low-grade metamorphic processes and increasing effective stress, *Geology*, *29*, 183-186.

Riddihough, R.P., and R. Hyndman (1991), The modern plate tectonic regime of the continental margin of western Canada, in *Geology of the Cordilleran orogen in Canada*, edited by H. Gabrielse, and C.J. Yorath., pp. 435-455, Geol. Surv. Can.

Ristau, J., G.C. Rogers, and J.F. Cassidy (2003), Moment magnitude-local magnitude calibration for earthquakes off Canada's west coast, *Bulletin of the Seismological Society of America*, *93*, 2296-2300.

Rogers, G., and H. Dragert (2003), Episodic tremor and slip on the Cascadia subduction zone: The chatter of silent slip, *Science*, *300*, 1942-1943.

Satake, K., K. Shimazaki, Y. Tsuji, and K. Ueda (1996), Time and site of a giant earthquake in Cascadia inferred from Japanese tsunami records of January 1700, *Nature*, *379*, 246-249.

Spiess, F.N., C.D. Chadwell, J.A. Hildebrand, L.E. Young, G.H. Purcell, and H. Dragert (1998), Precise GPS/Acoustic positioning of seafloor reference points for tectonic studies, *Physics of the Earth and Planetary Interiors*, *108*, 101-112.

Suzuki, M., T. Sasaki, and T. Tsuchiya (1992), Digital acoustic image transmission system for deep-sea research submersible, in *Proc. Oceans*, pp. 567-570, Newport, RI.

Suzuki, M.N., K; Tsuchiya, T; Nakanishi, T (1989), Digital acoustic telemetry of color video information, in *Oceans '89. Proceedings*, pp. 893-896, Seattle, WA.

Tadokoro, K., M. Ando, R. Ikuta, T. Okuda, G.M. Besana, S. Sugimoto, and M. Kuno (2006), Observation of coseismic seafloor crustal deformation due to M7 class offshore earthquakes, *Geophysical Research Letters*, *33*, L23306, doi:10.1029/2006GL026742.

Tolstoy, M., and D.R. Bohnenstiehl (2006), Hydroacoustic contributions to understanding the December 26th 2004 great Sumatra-Andaman Earthquake, *Surveys in Geophysics*, *27*, 633-646.

Tryon, M., K. Brown, L.R. Dorman, and A. Sauter (2001), A new benthic aqueous flux meter for very low to moderate discharge rates, *Deep-Sea Research Part I-Oceanographic Research Papers*, *48*, 2121-2146.

Tryon, M.D., K.M. Brown, and M.E. Torres (2002), Fluid and chemical flux in and out of sediments hosting methane hydrate deposits on Hydrate Ridge, OR, II: Hydrological processes, *Earth and Planetary Science Letters*, *201*, 541-557.

Vrolijk, P., A. Fisher, and J. Gieskes (1991), Geochemical and Geothermal Evidence for Fluid Migration in the Barbados Accretionary Prism (Odp Leg 110), *Geophysical Research Letters*, *18*, 947-950.

Wang, K., R. Wells, S. Mazzotti, R.D. Hyndman, and T. Sagiya (2003), A revised dislocation model of interseismic deformation of the Cascadia subduction zone, *Journal of Geophysical Research-Solid Earth*, *108*, 2026, doi:10.1029/2001JB001227.

Wang, K.L., and E.E. Davis (1996), Theory for the propagation of tidally induced pore pressure variations in layered subseafloor formations, *Journal of Geophysical Research-Solid Earth*, *101*, 11483-11495.

Zhao, S., X. Wu, T. Hori, A. Smith, Y. Kaneda, and S. Takemoto (2003), Deformation and stress localization at the Nankai subduction zone, southwest Japan, *Earth and Planetary Science Letters*, *206*, 145-160.

Chapter 4

Predicted Seafloor Flow Rate Response to Sudden and Slow Slip Deformation in a Heterogeneous Half-Space

Abstract

Observations of transient flow through the seafloor during the 2000 Costa Rica Seismogenic Zone Experiment off the Nicoya peninsula suggests transient deformation events occurred in the shallow subduction zone, around 10 km arcward from the Middle America Trench. The observed deformation in this region is unexpected, as it is generally believed that accommodation of plate convergence in the shallow plate interface is through stable sliding. This study is an investigation of the type and extent of deformation events that could cause these flow transients.

Fluid flow rates in response to displacement on a fault in a porous media are numerically calculated using a fully-coupled poroelastic finite element model. Modeled flow rates at the surface of a half-space, the seafloor, are intended to assist in interpretation of records from seafloor flow meter instrumentation. Model results show seafloor fluxes are a superposition of two effects causing volumetric strain at the surface: 1) compressional and dilational regions that radiate out from the fault tips, and 2) extensional and compressional bending of the free-boundary surface. Solutions of the spatial and temporal flow rate response to sudden slip along the decollement of a subduction zone are presented for near-field to far-field ruptures in a homogeneous crust and a heterogeneous crust with a layer of sediment overlying the basement.

The characteristic patterns in flow rate for near-field and far-field ruptures in homogeneous and heterogeneous crust help to determine optimal instrument placement for future subduction zone studies. In addition, comparisons of the fully-coupled half-space model simulations for a homogeneous verses a heterogeneous crust demonstrates

situations where it is safe to use existing analytical solutions for finite ruptures in a homogeneous poroelastic half-space instead of finite element modeling.

Novel simulations of updip and downdip propagating ruptures in this study demonstrate unique temporal records of flow rate through the seafloor surface. These propagating rupture model results are applied to help constrain rupture characteristics of a flow event recorded on the toe of the Costa Rica prism. The observed flow rate time series is nicely reproduced with a downdip propagating rupture centered below a flow meter instrument 6.5 km arcward from the trench. The observed variability in flow rates recorded at 2 instruments located at along-strike distances of 15 and 30 km could be explained by a single bilaterally propagating event that has an along-strike variation in rupture initiation. This is the first result suggesting episodic slow slip may initiate near the trench and possibly independent of a triggering event further downdip. A shallow slow release of stored energy is also the likely cause for shallow propagation during the nearby 1992 Nicaragua tsunamogenic earthquake.

This proposed slow slip event in the frontal Nicoya prism, a section where subducted clay-rich sediments along the decollement are saturated and hydrous, poses important questions concerning processes controlling temporal variation of fault mechanics in the 'stable-sliding' prism toe. How does stress accumulate at the shallow plate interface? Perhaps the topography associated with the normal faulting of the subducting basement prevents stable sliding from occurring until a critical stress threshold is overcome.

1. Introduction

The goals in this chapter are to 1) numerically predict surface flow rate patterns for sudden-slip seismic and slow-slip aseismic dislocations; 2) use these numerical model predictions to interpret data obtained from the toe of the Costa Rica forearc prism where unique temporally variable flow signals have been recorded [*Brown et al.*, 2005]; and 3) discuss optimal instrument placement for future deployments to constrain rupture dimensions.

Partial locking in the seismogenic zone of the Costa Rica subduction system [*Norabuena et al.*, 2004; *Schwartz and DeShon*, 2006] demonstrates that coupling of the plate interface does not follow a simple model of a locked seismogenic zone between stable-sliding aseismic zones [*Scholz*, 1998]. Other indications that the behavior of the plate interface varies spatially and temporally are hydrologic observations of episodic slip updip of this 'partially-locked zone' [*Brown et al.*, 2005; *Davis and Villinger*, 2006] in the supposedly stable-sliding zone, and anamolous tsunamogenic earthquakes with ruptures extending through to the trench [*Kanamori and Kikuchi*, 1993; *Polet and Kanamori*, 2000]. Although it is suggested that a transition from a locked zone to a stable sliding zone exists and corresponds with thermally controlled mineral reactions, e.g. opal diagenesis and smectite-illite dehydration reactions [*Harris and Wang*, 2002; *Spinelli and Saffer*, 2004], the aforementioned observations suggest that perhaps these processes aren't the primary control of rupture initiation and extent. Polet and Kanamori [2000] develop a new model to explain the updip propagation of tsunamogenic ruptures through the 'stable-sliding' zone that suggests characteristic differences in incoming basement topography and sediment thicknesses may play an important roll in fault mechanics in the shallow subduction zone.

Scientists desire to gain an understanding of these and other, potentially unknown, processes that govern the build-up and release of stress in these tectonically hazardous regions in a larger effort to understand the earthquake cycle. To do this, it is necessary to better quantify the temporal and spatial variation of stressing and relaxation over the entire plate interface updip of the 350° isotherm that roughly marks the transition from plastic to brittle rock deformation [*Hyndman et al.*, 1993; *Hyndman et al.*, 1997]. Furthermore, do the processes that control temporal variation in frictional properties such as potential migration of pore fluids [*Brown et al.*, 1994; *Melbourne and Webb*, 2003] influence neighboring plate interface 'zones', or do the frontal prism and 'partially-locked zone' further downdip behave independently of one another? If the assumption can be made that volumetric strain is the cause for observed hydrologic transience in the offshore subduction zone, then constraints on the location and/or size of faulting events causing hydrologic transience made via poroelastic modeling will help to address these questions.

Hydrologic variation in relation to earthquake events has been observed onshore in the form of well height and water chemistry changes [see Chapter 2, Section 1; *Roeloffs*, 1996; *Toutain and Baubron*, 1999 and references therein]. Although there are several theoretical explanations for mechanisms for hydrologic pressure response to deformation events, including permeability changes of fractures and seismic shaking induced changes in pore pressures in a saturated soil, volumetric strain related change in hydrologic pressure is particularly significant in the near field and very simple conceptually. Shear faulting on a finite length fault will result in a four-quadrant pattern of compression and dilation [*Booker*, 1974; *Rudnicki*, 1986; *Wang*, 1997; *Wang*, 2000]

with increased pressure in the compressional quadrants and decreased pressure in the dilational quadrants.

This hydrologic response to volumetric strain has been confirmed in exemplary studies where expected earthquake aftershock locations [*Bosl and Nur*, 2002] and coseismic well height changes [*Jonsson et al.*, 2003] match the volumetric strain predicted four-quadrant pattern. Common to these studies and several others [*Rudnicki et al.*, 1993; *Quilty and Roeloffs*, 1997; *Ge and Stover*, 2000; *Davis et al.*, 2001; *Lee et al.*, 2002; *Masterlark and Wang*, 2002], is the use of Biot's poroelastic theory which linearly relates changes in volumetric strain and fluid content per unit volume in a saturated porous material to changes in stress and pore pressure.

1.1. Models of Deformation in a Poroelastic Material

In certain cases observed data can be reasonably approximated using a simplified fault geometry [*Rudnicki et al.*, 1993]. By modeling dislocation on a semi-infinite fault plane in an infinite space Rudnicki et al. are conveniently able to use the analytical poroelastic solution obtained by Rice and Cleary (Table 1) [*Rice and Cleary*, 1976] to constrain the location of creep events on the San Andreas strike-slip fault with respect to a well monitoring station. Other studies find that models with this simple fault geometry do not reproduce the observations [*Quilty and Roeloffs*, 1997; *Davis et al.*, 2001; *Lee et al.*, 2002]. A buried fault plane requiring a half-space model, and/or a rectangular fault geometry requiring 3-D model, allows for a better fit. Futhermore, inclusion of a shear stress term in the relationship between volumetric strain and pore pressure is found to be a necessary modification of the poroelastic model in order to

explain observations very close to the fault plane where shear stresses are high [*Wang*, 1997; *Ge and Stover*, 2000]. While the coseismic solution of pore pressure resulting from a rectangular fault in a half space can be arrived at analytically (Table 1) [*Okada*, 1992], postseismic poroelastic relaxation must be modeled numerically, e.g. using a Finite Element Model (FEM).

Table 4-1: Models of Deformation in a Poroelastic Material

	Fault geometry	coupling	coseismic pressure field p(x,y,0)	Postseismic pressure field p(x,y,t)	half-space	hetero-geneous
Existing models	sudden slip on a semi-infinite or finite fault	coupled	Rice and Clearly 1976 Rudnicki 1986, 1987			
		uncoupled	Okada 1985, 1992	FEM	X	Cutillo et al. *permeability only*
	propagating semi-infinite fault	fully coupled	Roeloffs and Rudnicki, 1984/85			
Proposed models	sudden slip finite fault	fully coupled	FEM		X	X
	propagating finite fault	fully coupled	FEM		X	X

Shaded references indicate solution is analytical.
'X' or reference indicates capacity of modeling a half-space and/or heterogeneity.

The approach to modeling the pressure field in a half space in response to coseismic strain is to assume that stresses and strain do not vary with time following the initial dislocation on the fault. This is a valid assumption when deformation is

effectively instantaneous in comparison with diffusion times of the pore fluids through the porous media [*Wang*, 2000]. The model of the pore pressure field through time, as pore fluid diffusion occurs following an applied coseismic stress/strain field initial condition obtained using Okada's [1992] solution, is referred to as an uncoupled solution.

A study by Davis et al. [2001] highlights the use of this uncoupled poroelastic modeling technique to determine characteristics of a rupture from transients recorded at offshore hydrologic monitoring stations. Pressure records from instrumented boreholes located at 25.6 km, 33.5 km and 101 km distant from the Juan de Fuca Ridge spreading center logged transience correlated with an earthquake swarm at the ridge axis beginning on June 8, 1999. Using Okada's half-space solution, the authors estimate that a ~12cm dilatation event at the ridge is needed to produce the observed pressure transients. Energy from a rupture of this size is equivalent to a >5.7 magnitude earthquake, however, only a 4.6 magnitude earthquake is observed. This discrepancy indicates that much of the dilatation occurred aseismically. This and similar studies of pressure response to volumetric strain, coseismicly, tidally, or barometrically induced, also help to constrain material properties [*Bredehoeft*, 1967; *Rojstaczer and Agnew*, 1989; *Davis et al.*, 2000; *Davis and Villinger*, 2006] which are crucial to relating pore pressure to strain in poroelastic modeling, and accurately determining rupture characteristics from hydrologic observations.

Thus far I have reviewed strategies for modeling hydrologic response to sudden slip, i.e. seismic, deformation events. However, slow slip deformation, i.e. aseismic, events are an important part of the earthquake cycle and have the potential to trigger

large seismic events [Chapter 3, Section 1; *Dragert et al.*, 2001; *Rogers and Dragert*, 2003] and tsunamis [*Kanamori and Kikuchi*, 1993; *Polet and Kanamori*, 2000]. In modeling aseismic events, the earlier assumption that stress and strain do not change with time is no longer valid and a fully coupled model is required to model the continually changing volumetric strain and diffusion of pore fluids throughout the duration of the propagating rupture. Roeloffs and Rudnicki [1984/85] provide a fully coupled analytical solution for a steadily propagating edge dislocation in an infinite space (Table 1). They interpret a 1 km/day velocity of the propagating rupture tip in a material with diffusivity of 1 m^2/s to have caused the observed creep event on the San Andreas in 1971 [*Johnson et al.*, 1973]. Since they aren't able to constrain material properties, they are unable to conclude whether their coupled deformation-diffusion model or the uncoupled model [*Wesson*, 1981] better matches the observed data. Both models assume the propagating rupture tip starts at a distance infinitely far away, passes by the observation point, and continues to an infinite distance. The models poorly match the observed persistant water-level change and this could indicate that the creep event didn't pass completely by the observation well.

1.2. Deformation from Seafloor Flux Measurements: Model Requirements

Pressure measurements made at borehole observatories in the offshore environment, while highly valuable scientifically, are difficult and costly to obtain. A suite of flow meter instruments is relatively simple to deploy at the seafloor. A grid of flow meter instruments placed in a zone of deformation, such as a subduction zone, gathering a number of hydrologic responses all to the same deformation event [*Brown*

et al., 2005], improves the feasibility of constraining rupture characteristics through modeling.

The flow meter instruments developed in the Hydrogeology and Tectonics Studies Laboratory measure rates of fluid flow through the seafloor. A half-space with a null excess pore pressure boundary condition at the surface is required to model the zero excess pore pressure at the sediment-water interface (SWI). A sudden step in the near SWI seafloor sediments due to deformation of the ocean crust will also result in a sudden step in the pressure gradient driving through the SWI because the pore pressure at the SWI is fixed at zero.

An analytical solution for volumetric strain at the surface of a half-space, i.e. the modeled seafloor, due to sudden slip can be calculated (Table 1) [*Okada*, 1985]. Flow rates can be calculated from the volumetric strain at the seafloor using Roeloffs' [1996] equation for excess pressure as a function of depth and time following the step change in volumetric strain, similar in form to the equation for cooling of a half-space following a uniform step in temperature over the half-space. Although this uncoupled approach would work for arriving at the spatial and temporal patterns of seafloor flux produced from sudden-slip deformation in a half-space, Okada's solution does not allow for deformation in a heterogeneous material, or slow slip deformation (Table 1).

Cutillo et al. (Table 1) [2006] use an uncoupled FEM in a half-space with a heterogeneous permeability structure to simulate deformation and fluid flow due to sudden slip on the decollement in the Costa Rica subduction zone. As in the previously mentioned uncoupled poroelastic deformation modeling studies, the initial strain and pore pressure fields in their model are calculated using Okada's solution for sudden-slip

in a half-space. Athough their modeled subduction zone has uniform poroelastic moduli, Cutillo et al.'s model demonstrates the importance of modeling the heterogeneous permeability structure of the subduction zone, and a 2-D finite length fault as opposed to a semi-infinite fault. These same complexities will be modeled to predict seafloor fluxes in this study but with the additional complexity of heterogeneous poroelastic moduli to represent the unlithified sediments and fractured basement rock that comprise the layered structure of the oceanic crust.

It is essential to characterize the expected temporal and spatial variability of surface flow rates generated from a fault propagating slowly, or aseismically, as the few recent and essentially unexplained hydrologic observations in the offshore environment are suspected to be a result of such slow slip events [*Brown et al.*, 2005; *Davis and Villinger*, 2006]. Because the hydrologic observation location is at the seafloor and pore fluid diffusion through the seafloor occurs immediately after initiation of the rupture, in contrast to the long characteristic diffusion times of pore fluids internal to the full space and distant from these areas of high pore pressure gradients driving fluid diffusion, a fully-coupled model is absolutely required. The only existing fully-coupled analytical solution is for an infinitely propagating rupture in an infinite space (Table 1) [*Roeloffs and Rudnicki*, 1984/85].

In this chapter, I first illustrate the necessity of using FEM to predict spatial and temporal variability in seafloor fluxes due to deformation in a poroelastic media. A comparison of the predicted spatial variability of flow rates at the seafloor boundary in a half-space FEM with that of flow rates predicted at an equivalent hypothetical observation surface above a finite-fault in infinite space using the coupled poroelastic

analytical solution (Table 1) shows characteristic differences. This result precludes the use of the fully-coupled analytical solution for propagation in an infinite space as a good analogue to a half-space model for predicting spatial and temporal variability observed at the seafloor.

I next investigate temporal and spatial patterns in seafloor flux resulting from sudden slip in both homogeneous and heterogeneous half-spaces to determine whether layered material can be approximated by a homogeneous material with 'effective' material properties, i.e. permeability and diffusivity values that represent pore fluid diffusion through the layered material. If the results of homogeneous and heterogeneous models are similar, use of Okada's solution to calculate volumetric strain at the surface is adequate and a practical shortcut to fully coupled FEM.

Finally, I use both sudden slip and propagating FEMs to characterize spatial and temporal patterns in predicted flow rates at the Costa Rica subduction zone. In this case study, the geometry of the FEM is designed according to the structure of the Costa Rica subduction zone, complete with a sedimentary layer overlying the ocean basement. The FEM results are then compared with flow rates recorded during the 2000 Costa Rica Seismogenic Zone Experiment (CRSEIZE).

2. FEM of Sudden Slip in a Half Space

A finite element modeling software package, ABAQUS, was used to model deformation and fluid flow in a poroelastic half-space. ABAQUS numerically solves fully coupled displacement and pore fluid diffusion analyses in any material geometry, homogeneous or heterogeneous in character. The FEM uses the governing equations of

linear elastic theory coupled with pore fluid diffusion [*Biot*, 1941; *Rice and Cleary*, 1976; *Roeloffs*, 1996; *Wang*, 2000]. These same governing equations are used in solving the fully coupled analytical problems of a sudden slip displacement on a finite length fault [*Wang*, 1997; *Wang*, 2000] and a propagating edge dislocation [*Roeloffs and Rudnicki*, 1984/85]. By using these equations an assumption that the crust responds to deformation in an elastic manner is made. This assumption is valid on short timescales [e.g. *King et al.*, 1988; *Ge and Stover*, 2000; *Wang*, 2000; *Davis et al.*, 2001; *Dragert et al.*, 2001].

For the specific application of studying coupled deformation and fluid flow at subduction zones, the subduction zone can be considered infinite in the along strike direction, z (Figure 1). Thus, the plane strain constitutive equations are used for relating strain and fluid mass content per unit volume to stress and pore pressure. These equations require a set of four independent elastic moduli. The FEM calls for two drained moduli, Poisson's (v) and Young's (E), fluid bulk modulus (K_f), solid grain bulk modulus (K_s), and void ratio (e). The force equilibrium equations and a pressure diffusion equation derived from the laws of Darcy and fluid-mass conservation complete the set of governing equations. The FEM calculates displacement and pore pressure from which flow rate through the seafloor boundary is calculated using Darcy's law:

$$q = \frac{\kappa}{\rho g}\frac{\partial p}{\partial y} \tag{1}$$

where hydraulic conductivity, κ, and weight density of the fluid, ρg, are model input parameters and $\partial p/\partial y$ is the vertical pressure gradient.

Figure 4-1: FEM box model of left-lateral sudden slip on a horizontal fault of finite length, L, at depth, d. As a plane strain model, the 2-D 'across-strike' cross section represents the geometry that extends infinitely in the along-strike direction, z. Axes of the 2-D pressure field plot: across-strike distance, x, and depth, y, are the same scale. Coseismic response approximated at dimensionless time τ=5e-11. A) Vertical fluid flow rate, q_{norm}, through the deformed seafloor (vertically exaggerated) and pore pressure field, $p(x,y)$, for a far-field rupture, L/d=0.25. Seafloor extensional fold (EF) and compressional fold (CF) lie interior to surface signature of volumetric compressional lobe (CL, warm colors) and dilational lobe (DL, cold colors) radiating from rupture tips. B) Near-field rupture, L/d=4. EF and CF overlap with CL and DL directly above rupture tips.

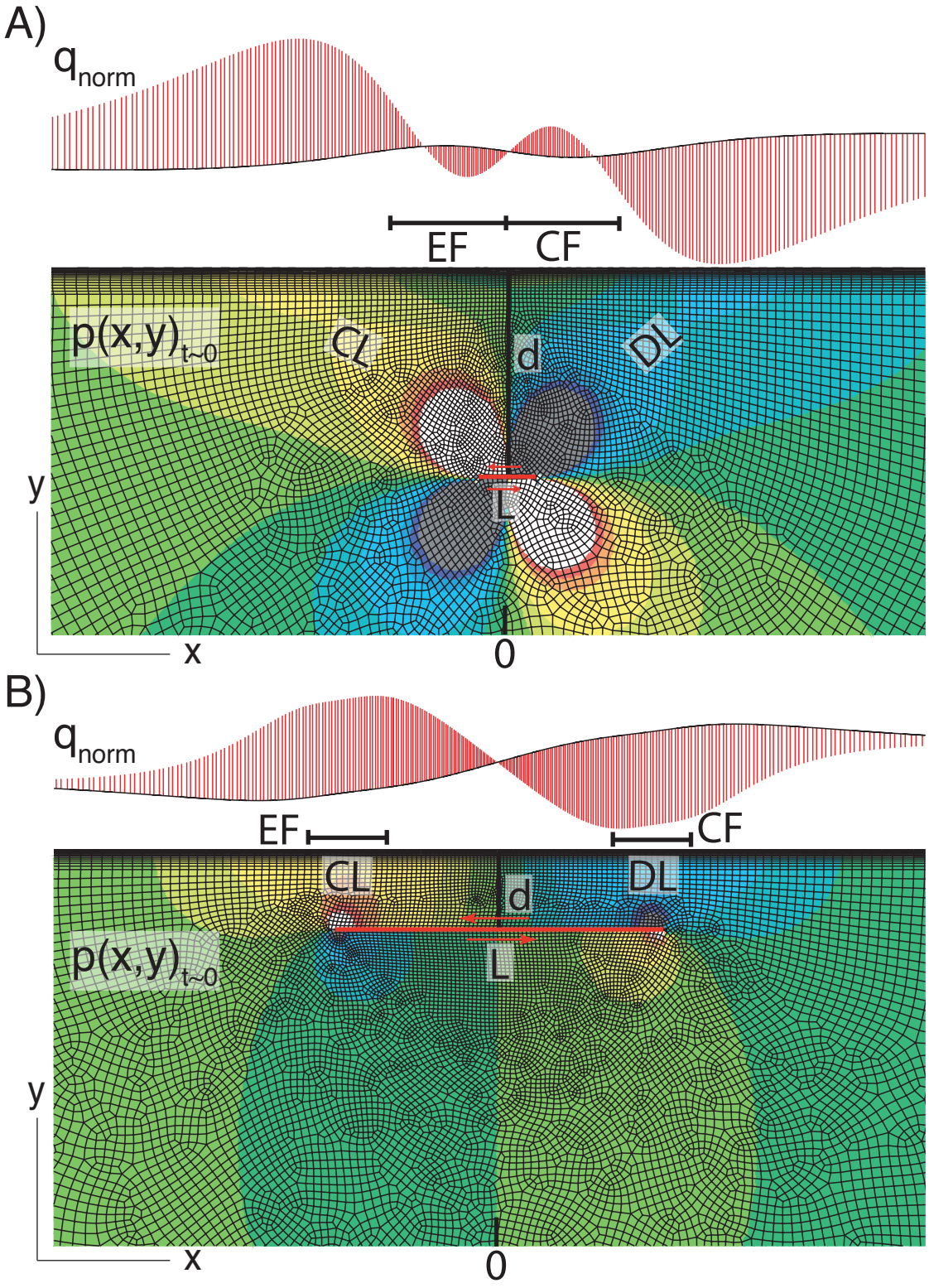
A)
q_{norm}
EF
CF
$p(x,y)_{t\sim0}$
CL
d
DL
L
y
x
0
B)
q_{norm}
EF
CF
CL
d
DL
L
$p(x,y)_{t\sim0}$
y
x
0

2.1 Box Model Geometry and Initial Boundary Conditions

A set of FEMs calculate near field to far field coseismic surface fluid velocities due to sudden slip on a horizontal fault of length L at a depth d below a horizontal free surface (Figure 1). These "box" models are comparable to the analytical model for sudden slip on a finite fault in an infinite space in all other significant aspects: models are composed of a homogeneous material and equal and opposite displacements occur on the upper and lower surfaces. Length to depth, L/d, ratios range from 4 to 0.0625 to characterize the half space solution at near and far fields, respectively. The walls and lower bound of the 2-D box model are ~150 km and >1e6 diffusion lengths from the fault at the early time at which estimates of coseismic fluid velocities are made. Diffusion length, $\sqrt{4ct}$, is the characteristic length to which a pressure wave will penetrate at a specified time, t, in a media with hydraulic diffusivity, c. In terms of model input parameters:

$$c = \frac{\kappa}{\rho g S} \tag{2}$$

where the hydrogeologic storage coefficient S is

$$S = \frac{\alpha\left(1 - \frac{4\eta B}{3}\right)}{KB} \tag{3}$$

Skempton's coefficient, B, frame bulk modulus, K, Biot-Willis coefficient, α, and poroelastic stress coefficient, η, are

$$B = \frac{\frac{1}{K} - \frac{1}{K_s}}{\frac{1}{K} - \frac{1}{K_s} + n\left(\frac{1}{K_f} - \frac{1}{K_s}\right)} \tag{4}$$

$$K = \frac{E}{3(1-2\nu)} \tag{5}$$

$$\alpha = 1 - \frac{K}{K_s} \tag{6}$$

$$\eta = \frac{\alpha(1-2\nu)}{2(1-\nu)}, \tag{7}$$

and the porosity, n, is simply

$$n = \frac{e}{1+e}. \tag{8}$$

The walls and lower bound are fixed in space whereas the upper bound, hereafter referred to as the seafloor, is free to move in both horizontal, x, and vertical, y, directions. The fault is a finite thickness of 10 meters.

Analytical models of edge dislocations on permeable (p=0) and impermeable ($\partial p/\partial y$=0) dislocation planes demonstrate that the pore pressure solutions for these two endmember cases converge at two diffusion lengths above the fault [*Rudnicki*, 1986]. Therefore, the permeability of the finite thickness fault in the FEM is insignificant as long as the depth of the fault is greater than $4\sqrt{ct}$ or one quarter meter. The walls and lower bound of the model are impermeable to flow but the seafloor, with boundary condition p=0, is permeable to flow.

The pore pressure is initially set to zero everywhere in the model. Although the true pore pressure in the crust has a hydrostatic gradient due to gravitational forces, the ambient field is arbitrary. The only forces driving transient flow events are the deviations from the ambient pressure field that result from strains in the crust.

2.2 Achieving Numerical Accuracy: Mesh Size and Minimum Resolvable Time

As accuracy of the model output at the seafloor is required, numerical artifacts in the near seafloor region cannot be tolerated. Meshing the FEM to obtain an accurate solution requires a small element size in regions with high pore pressure gradients, i.e. the rupture tips and more importantly in this application, the seafloor. At t=0 after a sudden slip is applied on the fault, the flow is infinite across the seafloor as pore pressure steps off to zero with the applied boundary condition. Therefore, no matter how small the element size, flow at the seafloor surface will not be resolved at an instantaneous time. However, the smaller the surface elements the earlier the time a stable pore pressure gradient at the surface is established and surface fluxes can be accurately resolved.

A seafloor surface element height of 1 cm is used for all FEM models in this study, and velocities are resolvable at a minimum dimensionless time of 5e-11. Dimensionless time, τ, is the fraction of the characteristic time for a pressure front to arrive at some distance from the source:

$$\tau = \frac{t}{\left(\frac{d^2}{4c}\right)}. \tag{9}$$

Note that the vertical distance from the seafloor to the fault, d, is used rather than a radial distance, $R = x^2 + d^2$. This simplification can be made for $|x| < d$ which is approximately the extent of the region with measurable flow rates and that for which flow rate predictions are intended. τ=5e-11 equates to tens to hundred of seconds after the seismic rupture in models with low permeability marine sediments (Table 2) and rupture depths of 2-16 km deep. Proportionately shorter times are resolvable in higher diffusivity materials. These minimum times at which flow rate predictions can be made are sufficiently small as they are on the order of the sampling frequency of the flow rate instrumentation. Finally, to prevent any numerical artifacts due to meshing, the element size gradually increases away from these very small elements at the surface and rupture tips out to the bounds of the box model (Figure 1).

Table 4-2: Poroelastic Material Parameters

Material Properties		Young Oceanic Basement	Costa Rica Sediment	Costa Rica Basement
Young's modulus (Pa)	$\boldsymbol{E}$	2.4e+10	6e+8	9.2e+9
Poisson's ratio	$\boldsymbol{\nu}$	0.25	0.1	0.3
grain bulk modulus (Pa)	$\boldsymbol{K_s}$	5e+10	5e+10	5e+10
fluid bulk modulus (Pa)	$\boldsymbol{K_f}$	2.4e+9	2.4e+9	2.4e+9
hydraulic conductivity (m/s)	$\boldsymbol{\kappa}$	1e-06	1e-10	1e-06
void ratio	$\boldsymbol{e}$	0.11	1.5	0.11
fluid weight density (Pa/m)	$\boldsymbol{\rho g}$	10253	10253	10253
hydraulic diffusivity (m^2/s)	c	1.4	5.2e-6	0.85

Bold parameters are parameters input into FEM

2.3. Running the Pore Pressure-Displacement Simulation

With the initial conditions specified and mesh over the geometry completed, the model is now ready to run a coupled pore pressure-displacement analysis, or in ABAQUS, a "soils" consolidation procedure. There are two steps within this analysis procedure, 1) application of the sudden displacement, hereafter referred to as the coseismic step, and 2) calculation of displacement, pore pressure, and fluid velocity fields after completion of the displacement, the postseismic step. In these sudden slip simulations, the postseismic step is just long enough for the numerical result to converge on a stable solution (τ=5e-11). The solution from the very short postseismic step will be used to approximate the coseismic response.

The displacement boundary condition is applied over the duration of the coseismic step, 1e-6 seconds. A physically representative elliptical displacement distribution, D, that satisfies the uniform stress drop criteria with the exception of at the rupture tip [*Lawn*, 1993; *Fialko*, 2004] is used

$$D = \frac{b\sqrt{\left(\frac{L}{2}\right)^2 - x^2}}{\frac{L}{2}} \tag{10}$$

$$x \leq \frac{L}{2} \tag{11}$$

where b, the maximum displacement of the upper fault surface relative to the lower fault surface, occurs at the center of the fault, or x=0 (Figure 1). A change in sign convention is applied such that b is positive for left lateral movement of the hanging wall with respect to the foot wall. The convenience of this sign change will become evident in the case study section. Following this coseismic step variable fields: displacement, pore pressure and fluid velocities, are calculated and output during the postseismic step.

The box model analyses for the range of length to depth ratios were run for each of two homogeneous material sections: relatively young, 3.6 Mya, oceanic basement, and low permeability Costa Rica sediment (Table 2). A specific weight, ρg, of the interstitial fluid of 1e5 kg m^{-2} s^{-2} was used for all analyses discussed in this chapter. A final set of analyses to investigate the effect of a more physically representative layered model was conducted for L/d=0.25. In this model, a 500 m thick section of Costa Rica sediment overlies the young oceanic basement (Figure 5 inset).

3. Predictions of Seafloor Fluid Flux in Response to Sudden Slip Deformation

The initial coseismic results from the box model FEM analyses are compared to the undrained pore pressure field solution for sudden slip on a finite horizontal fault. With an applied boundary condition p=0 at the seafloor in the FEM, it is clear that the magnitude of the coseismic flow rate predictions using the half space FEM verses infinite space analytical solution are not comparable. However, the aim of this comparison is to determine if there are significant differences in the spatial pattern of fluid flux through the seafloor. If so, then the existing fully coupled analytical solution for propagating edge dislocation in an infinite space is also not a good approximation for temporal or spatial patterns in surface flow rate response due to propagation.

3.1. Analytical Prediction

The analytical solution for pore pressure due to sudden slip on a semi-infinite horizontal fault or "edge dislocation" is

$$p(x,y)_{t=0} = -\frac{\gamma}{\pi} Gb \frac{y}{x^2 + y^2} \tag{12}$$

[*R. M. McKinley*, 1966; *Rice and Cleary*, 1976; *Rudnicki*, 1987; *Wang*, 2000]. The negative sign appears due to the aforementioned change in displacement, b, sign convention. The new material constants loading efficiency, γ, and shear modulus, G, are:

$$\gamma = \frac{B(1+\nu_u)}{3(1-\nu_u)} \tag{13}$$

$$G = \frac{E}{2 + 2\nu} \tag{14}$$

where the undrained Poisson's ratio, ν_u, is

$$\nu_u = \frac{3\nu + \alpha B(1 - 2\nu)}{3 - \alpha B(1 - 2\nu)}. \tag{15}$$

Following differentiation of equation (12) with respect to y

$$\frac{\partial p}{\partial y}_{t=0} = -\frac{\gamma}{\pi} Gb \frac{x^2 - y^2}{\left(x^2 + y^2\right)^2}, \tag{16}$$

coseismic vertical flow rates are calculated at the hypothetical observation surface $y=d$ using Darcy's law, equation (1). The pressure field for sudden slip on a finite fault centered at x=0 is obtained through superposition of two edge dislocations ending at x=–L/2 and L/2 [*Rudnicki*, 1986; *Wang*, 1997; *Wang*, 2000].

3.2. Spatial Variability in Seafloor Flux: FEM Box Model vs. Analytical Prediction

The FEM box model prediction of the coseismic pore pressure field, $p(x,y)_{t\sim 0}$, and resultant seafloor fluid flux patterns for both far and near field dislocations are as graphically depicted (Figure 1a,b). Pore pressure is positive due to compression in the upper left quadrant and negative due to dilation in the upper right quadrant. These compressional and dilational lobes of volumetric strain radiating out from the rupture tips will be hereafter abbreviated as CL and DL. Vertical fluid flow is up and out of the seafloor where CL meets the surface and down and into the seafloor where DL meets

the surface. In the near field, $L/d > 0.25$, peak pore pressures and fluxes at the seafloor associated with CL and DL are located above the rupture tips. As L/d decreases, the expression of CL and DL at the seafloor move further apart and outward from the rupture tips.

The comparison of the across-strike spatial variation in flow rate obtained using the analytical and finite element models demonstrates the significant differences in spatial patterns of surface outflow from the half space and infinite space approximations (Figure 2). To illustrate two primary effects of the free boundary, I plotted vertical component vectors of surface fluid velocities on a vertically exaggerated deformed seafloor and juxtaposed the pore pressure field (Figure 1). First, regions of compressional folding (CF) and extensional folding (EF) force fluid outflow and inflow, respectively. The signature of this flexure, or buckling, of the free boundary surface is superimposed on the CL and DL signatures. In the far field, $L/d \leq 0.25$, location of EF and CF are interior to CL and DL and an inversion of flow rates directly over the fault is observed (Figure 1a, 2a). In the near field, e.g. $L/d=4$, the effect of CF and EF above the rupture tips is barely distinguishable against the peak pore pressure magnitudes from the close proximity rupture (Figure 1b, 2b). The second major difference is the larger lateral spread of the pore pressure lobes in the half space as they reach the seafloor compared to the relatively tight contours of pore pressure below the fault (Figure 1). The manifestation of this effect in surface flow rate distribution is that a much broader tail exists in the half space solution than in the analytical solution (Figure 2).

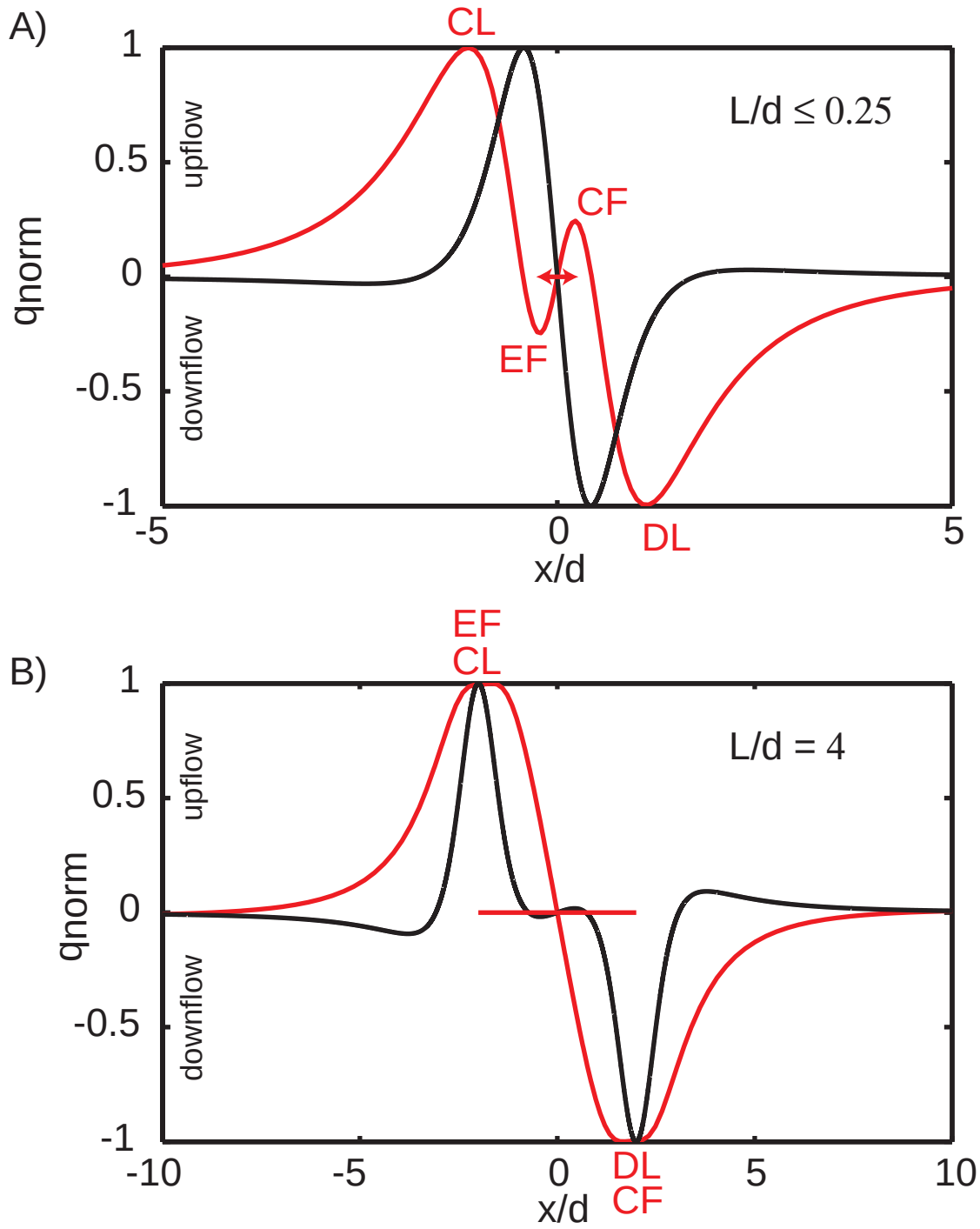

Figure 4-2: Normalized infinite-space analytical prediction (black line) of vertical flow rate, q_{norm}, at a hypothetical observation surface above a horizontal finite-length fault compared to normalized half-space FEM prediction (red line) of flow rate through the half-space surface, the seafloor. Predictions are plotted against dimensionless across-strike distance, x/d. A) Far-field rupture L/d≤0.25. B) Near-field rupture L/d=4.

3.3. Box Model Results: Temporal Variability

In addition to spatial variation in flow rates at the seafloor, numerical models are used to predict the temporal variation in vertical flow rate. The pressure field resulting from deformation in the coseismic step is unstable. Pore fluid diffusion, and hence fluid flow, occurs as excess pore pressures return to their equilibrium state, zero. A prediction of the temporal evolution of flow rates through the seafloor in this postseismic period is made using the solution to the analogous half-space cooling problem in thermodynamics [*Carslaw and Jaeger*, 1959; *Turcotte and Schubert*, 2002]

$$q_h \propto \frac{1}{\sqrt{\pi c_h t}} \tag{17}$$

where q_h is surface heat flux. The decay of vertical flow rate through the seafloor, q, is obtained by simply replacing the thermal diffusivity constant, c_h, with pore fluid diffusion constant, c, in equation (17). This analytical solution to the half-space cooling problem predicts the decay of surface flux in the numerical model very well even though it assumes the initial excess pressure throughout the half-space is uniform and extends to infinite depth (Figure 3). It is necessary to introduce a new dimensionless time, τ_0, for expressing the fraction of decay that has occurred due to drainage through the surface.

$$\tau_0 = \frac{d_{obs}}{\sqrt{\pi c t}} \tag{18}$$

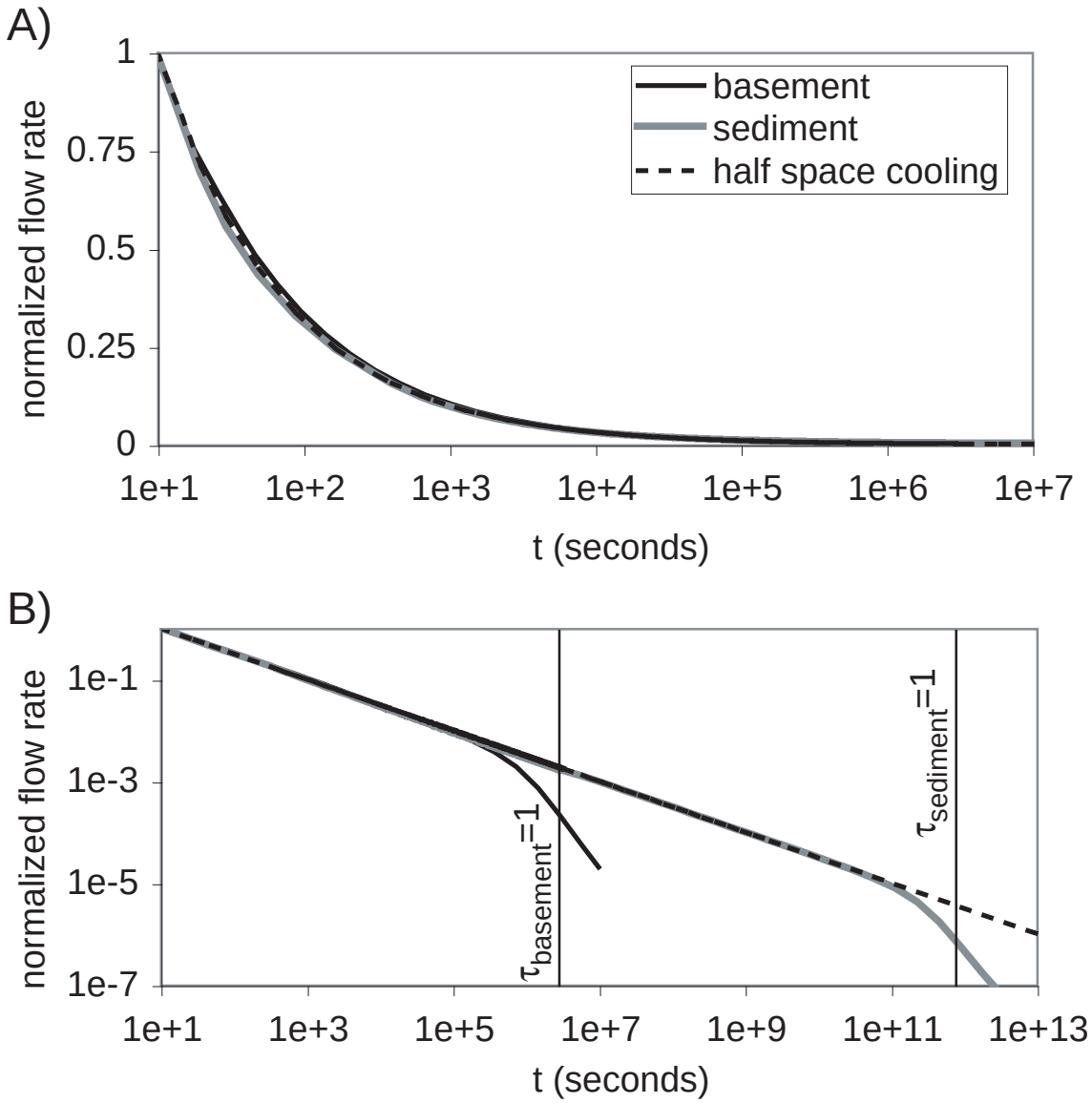

Figure 4-3: Half-space FEM predictions of decay of maximum vertical flow rate (i.e. evaluated at CL peak) for young oceanic basement and Costa Rica sediment (Table 2) compared to analytical prediction for pressure diffusion and flow rate time series based on the analogous thermal diffusion in a half-space problem. A) Log-linear plot of normalized dimensionless flow rate verses time, and B) log-log plot with characteristic diffusion times for basement and sediment materials at a distance d.

where d_{obs} is the depth of the hydrologic observation. In the FEM d_{obs} is the height of the seafloor element, 1 cm. Recall that the characteristic length used equation (9) to calculate the dimensionless time, τ, for pressure effects originating at the fault to arrive at the observation point, is the depth of the fault, d. At $\tau_{basement}$=1 the source of excess pressure originating at the fault reaches the seafloor surface and decay starts to occur more rapidly (Figure 3b), likewise for $\tau_{sediment}$=1. For times τ<1 the half-space analytical prediction can be used to extrapolate back to earlier times than could be resolved in the FEM.

3.4. Box Model Results: Applying Predictions

Solutions of spatial variation in flow rate across-strike from numerical simulations for the range of rupture L/d and in both basement and sediment materials are compared in figure 4. Vertical flow rates have been non-dimensionalized to allow the use of FEM predictions to determine vertical flow rates at the seafloor, in any homogeneous material, at any time τ<1.

$$\theta_s = \frac{q}{\left(\frac{\kappa\gamma G b \tau_0}{\pi\rho g d^2}\right)} \tag{19}$$

The dimensionless flow rate predictions are also applicable for ruptures with a comparable L/d in any spatial scale (note dimensionless x-axis) and with any maximum displacement distance b. Seafloor surface fluxes are larger for larger L/d since the stress

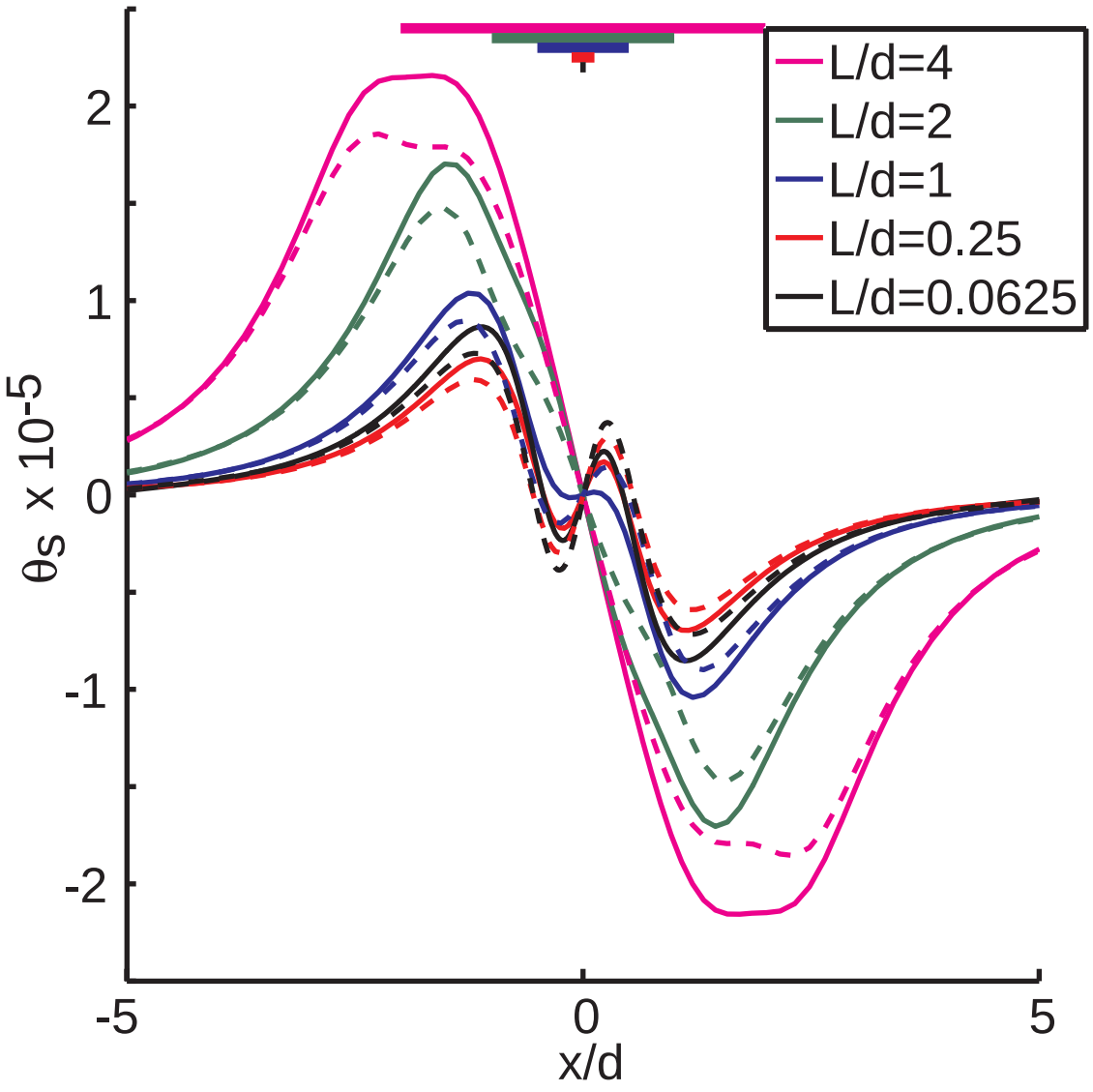

Figure 4-4: Box model dimensionless flow rate, θs, FEM predictions for a range of rupture L/d simulations in both homogeneous Costa Rica sediment (dashed) and young oceanic basement (solid) material (Table 2). Colored bars represent extent of rupture for each L/d value.

concentrated at the rupture tips from the strain that occurred over a relatively large area is greater. For L/d=4 down to L/d=0.25 the effect of EF and CF become increasingly significant as CL and DL migrate apart from rupture tips, and EF and CF. For $L/d \leq 0.25$, the ratio of the distances between EF and CF, and CL and DL, is constant and therefore the spatial flow rate pattern is constant. Notice also that for low-permeability sediment, the relative contribution of EF and CF to surface flow rates is greater than for the high-permeability basement.

3.5. Box Model Results: Layered Material Section

Dimensionless vertical flow rates through the seafloor of the heterogeneous layered and homogeneous basement and sediment models for L/d=0.25 are plotted in figure 5. To nondimensionalize, and thus allow for comparison of the layered model with homogeneous material models, effective hydraulic conductivity of the layered section, κ_{eff}

$$\kappa_{eff} = \frac{1}{\frac{l_1}{\kappa_1} + \frac{l_2}{\kappa_2}} \tag{20}$$

was used in place of κ in equation (19) and likewise, τ was calculated using the effective diffusivity, c_{eff}

$$c_{eff} = \frac{1}{\frac{l_1^2}{c_1} + \frac{l_2^2}{c_2} + l_1 l_2 \left(\frac{\kappa_2}{\kappa_1 c_2} + \frac{\kappa_1}{\kappa_2 c_1} \right)} \tag{21}$$

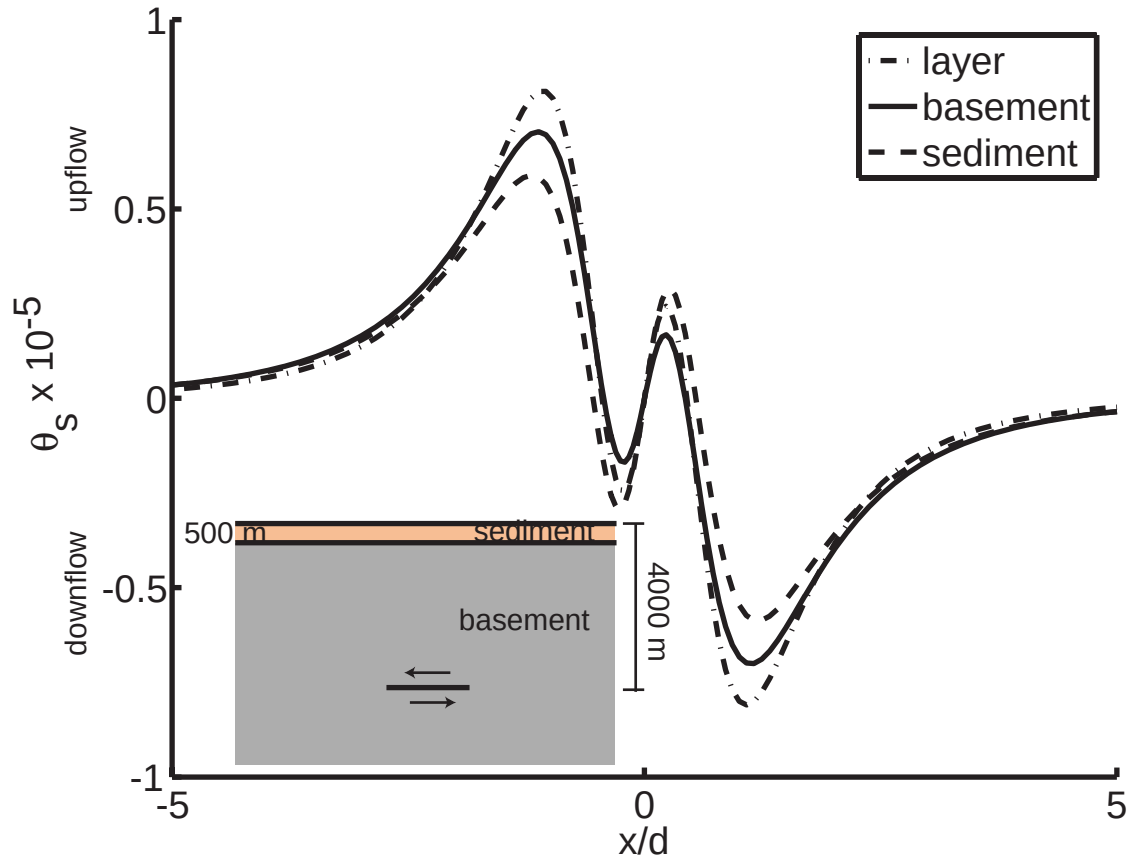

Figure 4-5: Layered box model prediction compared to homogeneous Costa Rica sediment and young oceanic basement predictions for rupture L/d=0.25. Inset: Layered box model geometry: 500 meter thick Costa Rica sediment overlying young oceanic basement in which a horizontal rupture occurs at d=4000 m.

[*Kyaar and Vares*, 1982; *Salazar et al.*, 1998]. Parameters with subscripts '1' and '2' refer to sediment and basement layer properties, respectively; l_1 and l_2 are the proportional thicknesses 0.125 and 0.875 for the 500 m sediment layer and the 3500m basement layer that lie between the pressure source, the fault, and the surface (Figure 5 inset). Effective poroelastic moduli for a layered material are nonexistent; hence, values for the loading efficiency and shear modulus for the surface sediment layer are used in equation (19). The dimensionless flow rates produced by the layered model numerical simulation exceed that of the homogeneous sediment and homogeneous basement results, but are still within the same order of magnitude.

4. Case study: Costa Rica

4.1. Geologic background

The Central American subduction zone is a well-studied non-accretionary subduction zone margin. The late Oligocene aged, ~24My, Cocos plate [*Klitgord and Mammerickx*, 1982; *Barckhausen et al.*, 2001] meets with the Caribbean plate at the Middle America Trench (MAT). The plate convergence rate is 8.5cm/yr [*DeMets*, 2001]. The resultant accumulation of tectonic strain is released during large earthquakes rupturing the seismogenic zone every 40 to 50 years [*Guendel*, 1986] cited by [*Cutillo et al.*, 2006]. However, interseismic microseismisity and aseismic slip in the offshore region, including the updip partially-locked section of the seismogenic zone and continuing up to the trench, are poorly characterized.

The incoming Cocos plate is composed of two sections: the northern section formed at the East Pacific Rise (EPR), and the southern section derived from plate

formation at the Cocos-Nazca Spreading (CNS) center. The EPR-CNS suture between these two sections extends offshore from the Nicoya peninsula [*von Huene et al.*, 2000; *Barckhausen et al.*, 2001]. North of the suture, the subducting plate is relatively thin and cold compared to the CNS generated plate to the south [*Protti et al.*, 1995; *Ye et al.*, 1996; *Sallares et al.*, 2000]. The Cocos plate to the south of the EPR-CNS suture is dotted with a chain of Galapagos hot spot related seamounts. Just north of the EPR-CNS suture, the incoming Cocos plate is free of seamounts but exhibits outer rise normal faulting. The incoming basement topography at the northern end of the Cocos plate, off the coast of Nicaragua, is also unique with abundant normal faulting and horst and graben structures (von Huene et al. 2000).

The across-strike corridor of the subduction zone, from Costa Rica's Nicoya peninsula to the MAT north of the EPR-CNS suture has been the subject of extensive surveying and monitoring experiments. The abundant data sets from the Costa Rica margin are largely due to the proximity of the MAT to land. Deep-sea, and Ocean drilling program boreholes [*von Huene*, 1985] et al. [*Kimura et al.*, 1997; *Morris et al.*, 2003], seismic surveys [*Shipley et al.*, 1992; *Hinz et al.*, 1996; *Ye et al.*, 1996; *Christeson et al.*, 1999], swath bathymetry [*von Huene et al.*, 2000], geodetic studies [*Norabuena et al.*, 2004; *Protti et al.*, 2004; *Schwartz and DeShon*, 2006], Ocean Bottom Seismometer (OBS) [*Newman et al.*, 2002] and flow meter measurements [*Brown et al.*, 2005], and borehole CORK installments [*Davis and Villinger*, 2006] have provided valuable insight into the structure, material properties and mechanical behavior of the subduction zone interface.

In a seismic survey of this corridor of the Cocos plate Shipley [1992] characterized the geometry of the margin from the toe to just beneath the shelf edge, ~55km distant from the trench. Based on cores from deep-sea drilling project site 565, von Huene [1985] suggested the prism is an offshore extension of the late Cretaceous age [*Di Marco*, 1995.] Nicoya ophiolite complex exposed on the Nicoya peninsula. Seismic velocity measurements further support this theory [*Hinz et al.*, 1996; *Ye et al.*, 1996; *Christeson et al.*, 1999]. The Nicoya complex reaches to within 10 km of the trench. The frontal prism, or the ~5-7 km frontal to this Nicoya complex backstop, is a section primarily composed of deformed trench fill sediments from further up the prism slope [*Christeson et al.*, 1999; *von Huene et al.*, 2000]. Sediment on the incoming plate subducts with the Cocos plate as per the non-accretionary subduction zone classification [*Kimura et al.*, 1997; *McIntosh and Sen*, 2000]. In addition to seismic velocity measurements, ODP leg 205 geotechnical hydrogeological tests [*Bolton et al.*, 2001], and borehole formation pressure measurements [*Davis and Villinger*, 2006] further help to constrain material properties of the Costa Rica subduction zone.

Accurate GPS measurements of plate deformation in the seismogenic region during interseismic periods using onshore arrays have been obtained since most of the seismogenic zone is conveniently located beneath the Nicoya peninsula as opposed to offshore. These geodetic surveys in conjuction with measurements of seismicity have helped scientists to identify multiple transitions in the mechanical behavior of interseismic interplate deformation within the seismogenic zone [*Norabuena et al.*, 2004; *Schwartz and DeShon*, 2006], and the occurrence of slow slip events [*Protti et al.*, 2004]. Through interpretations of geodetic inversions of interseismic slip, it is estimated

that updip of the freely-slipping zone exhibiting microseismisity (Mw<5) the plates are partially locked at 50-75% of plate velocity [*Norabuena et al.*, 2004; *Schwartz and DeShon*, 2006]. This partially-locked zone extends from 15 km depth below sea level updip along the interplate interface to a depth of ~8 km below sea-level, corresponding to a distance from the trench of ~70 km to ~35 km.

It is hypothesized that the transition from stick-slip behavior in the partially-locked zone, to aseismic stable-sliding updip of the partially-locked zone is thermally controlled [*Harris and Wang*, 2002; *Spinelli and Saffer*, 2004]. However, the updip limit of this partially-locked zone is poorly constrained as 1) onshore GPS measurements are unable to accurately resolve offshore motions, and 2) mineral reactions that occur with increasing temperature of subducting sediments don't necessarily control the frictional properties of the plate interface. Significant changes in plate coupling not correlated with temperature [*Norabuena et al.*, 2004] suggest an alternative mechanism controls coupling. Measurements of the seismic frequency-magnitude relationship, the *b*-value, off the Nicoya peninsula nicely resolve along-strike variation in plate coupling [*Ghosh et al.*, 2006]. Locations where seamounts ride the subducting basement beneath the forearc prism south of the EPR-CNS suture have low *b*-values, indicating stronger plate coupling associated with this anomalous basement topography.

4.2. Hydrogeologic Transient Events

Although this presumed aseismic deformation has not been detected using offshore geodetic measurements, recent hydrogeologic measurements made offshore the

Nicoya Peninsula have indicated the presence of slow slip events updip of the partially-locked zone and possibly extending into, or originating from within, the partially-locked zone [*Brown et al.*, 2005; *Davis and Villinger*, 2006]. Hydrologic instrumentation for measuring formation pressure captured two transient events in the toe of the Costa Rica prism [*Davis and Villinger*, 2006]. GPS velocities recorded onshore also show anomalous activity at the same time [*Protti et al.*, 2004]. The GPS data for one of these events suggests that a 60 km rupture initiated at the coast of the peninsula and propagated northeast over a period of 2-3 weeks. The pressure transient recorded at the toe of the prism, ~60 km offshore, occurred about three weeks after the initiation of the onshore propagating slip. Davis and Villinger [2006] suggest the event is potentially a result of a mirroring propagating slip that migrated updip along the interplate interface from the coast to the trench.

Evidence for aseismic activity at the toe of the Costa Rica prism was recorded using flow meter instrumentation placed at the seafloor during the CRSEIZE (Figure 6) [*Brown et al.*, 2005]. Three Chemical Aqueous Transport flow meters [*Tryon et al.*, 2001], numbers 2, 3 and 5 located on the frontal prism spanning an along-strike distance of 30km, simultaneously recorded three 2-3 week duration flow events during the six-month deployment (Figure 7). No seismic activity, but rather a tremor-like noise correlating with timing of the flow pulses is recorded. Events are therefore hypothesized to result from a strain imposed by aseismic deformation [*Brown et al.*, 2005].

More flow meter records, borehole formation pressure measurements in combination with offshore seismic and geodetic measurements are needed to adequately constrain these transient events. However, a preliminary effort to determine whether

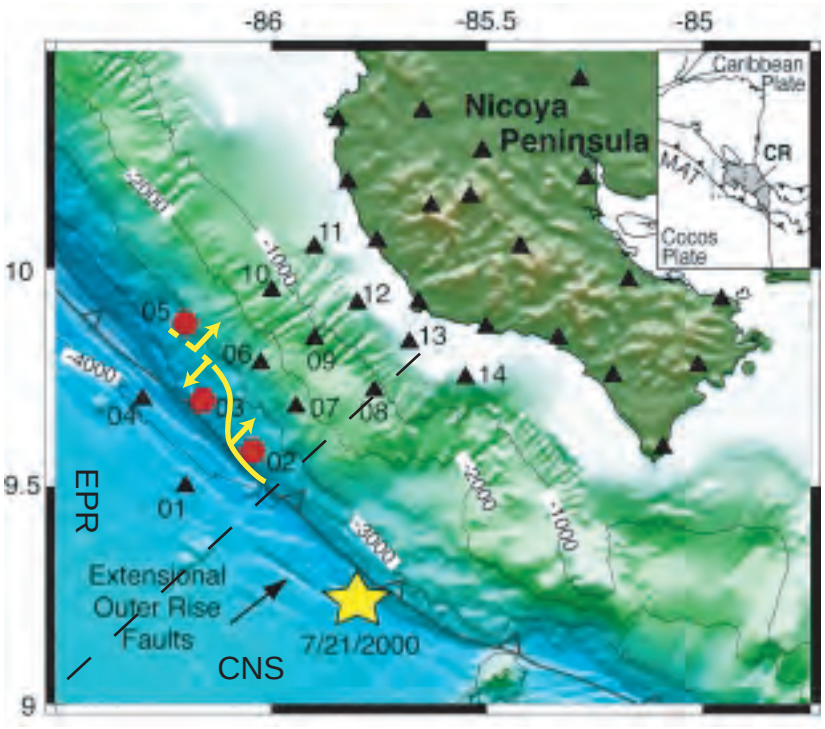

Figure 4-6: Along and across-strike placement of flow meters in the Costa Rica subduction zone north of the EPR-CNS suture (dashed line) during the 2000 CRSEIZE (Brown et al. 2005). Proposed initiation of bidirectional rupture propagation varies along strike (yellow line).

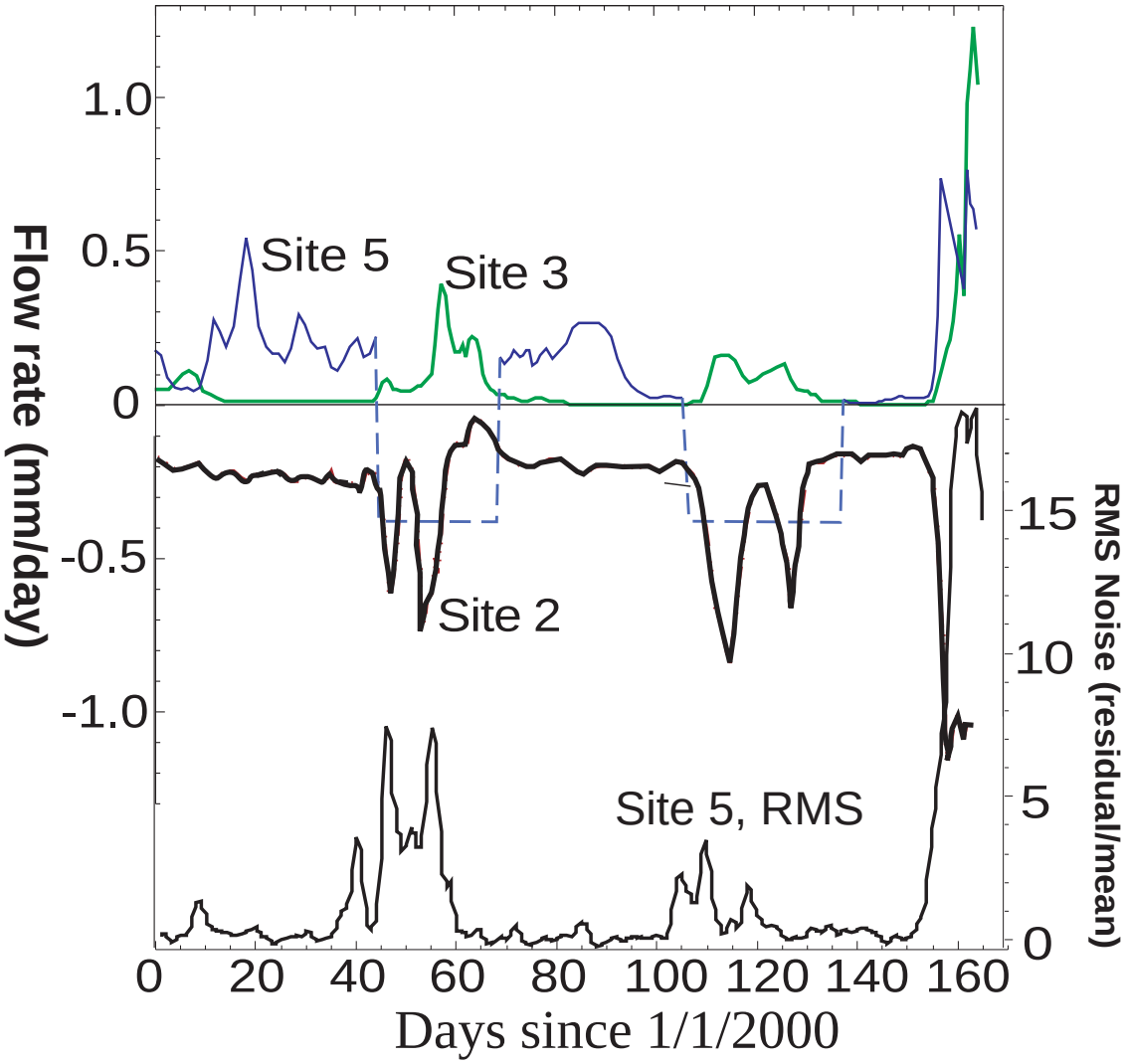

Figure 4-7: Three 2-3 week long periods of flow rate transience observed at three flow meter sites located along the toe, or frontal prism, of the subduction zone. Residual vertical accelerations recorded on OBS at site 5 is plotted for comparison. The RMS record is smoothed using a 12 hour box car window (Brown et al. 2005).

aseismic movement could potentially cause these observed hydrogeologic transients is made with the use of a FEM tailored to represent the geometry and material sections in the Costa Rica subduction zone.

4.3. Methods: Costa Rica Sudden and Slow Slip FEM

4.3.1. Model Geometry, Material Properties, and Meshing

A simplified FEM geometry for the Costa Rica case study is based on the thickness of the slope sediments and location of the decollement as inferred from seismic sections of the margin [*Shipley et al.*, 1992; *Christeson et al.*, 1999], and seafloor bathymetry. The seafloor surface arcward of the trench is 5° and dipping toward the trench, and seaward of the trench the seafloor is 3°, also dipping toward the trench (Figure 8). A 500 m thick sediment layer overlies the incoming Cocos basement and linearly thickens over the prism to >2 km at the continental margin. The surface along which ruptures occur in the simulations dips 10° arcward, an average of the steepening dip angle of the decollement between the toe and the continental margin [*Shipley et al.*, 1992; *Christeson et al.*, 1999]. While it is a significant simplification, choosing a constant dip angle to represent the decollement is necessary to maintain the desired similarity of the model geometry, and therefore model predictions, at different spatial scales.

The sediment apron over both the incoming plate and prism are assigned the same ‘Costa Rica sediment’ material properties (Table 2, Figure 8). Likewise, the incoming basement and prism sections beneath the sediment apron are assigned the

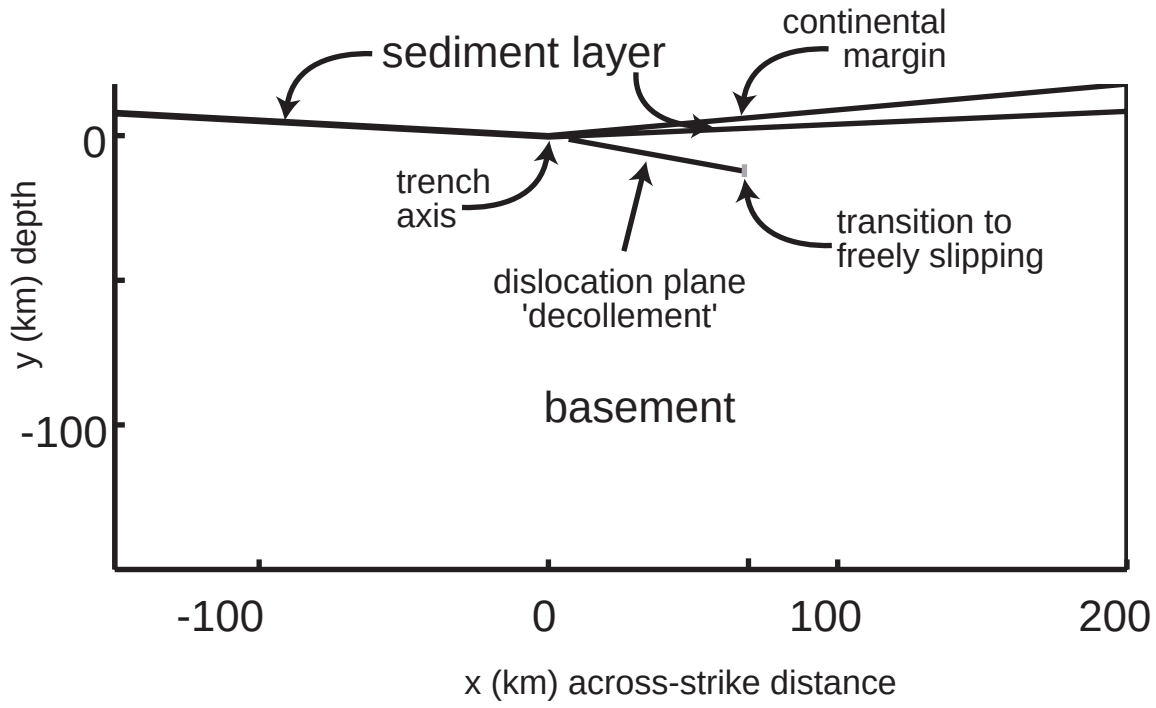

Figure 4-8: Costa Rica subduction zone model geometry, across-strike cross section. Displacement occurs along the dislocation plane during FEM simulations. Maximum modeled rupture lengths extend from near the trench axis to a maximum distance of ~70 km from the trench, the updip limit of the microseismic zone (Schwarz and DeShon, 2006).

same ‘Costa Rica basement’ material properties. Although the subducting Cocos basement and the Nicoya ophiolite complex that composes the prism have different ages, and likely different material properties, the sensitivity of surface flow rates to these differences is suspected to be negligible when a much lower permeability and diffusivity sediment overlies the basement, equations (20) and (21).

Elastic moduli for Costa Rica basement and Costa Rica sediment in Table 2 are those determined from borehole measurements of formation pressure response to tidal loading in the incoming Cocos basement (ODP hole 1253) and the Costa Rica frontal prism sediments (ODP hole 1255), respectively [*Davis and Villinger*, 2006]. Davis and Villinger [2006] assumed a Poisson’s ratio of marine sediment equivalent to that of earlier works [*Wang and Davis*, 1996]. Sediment porosity used is an average of the porosity-depth trend measured in prism sediment cores [*Kimura et al.*, 1997; *Bolton et al.*, 2001; *Davis and Villinger*, 2006]. The void ratio and Poisson’s ratio assumed in calculations of basement compressibility [*Davis and Villinger*, 2006] are again based on previous work [*Davis et al.*, 2000].

The basement permeability used is that of young oceanic basement (Table 2) [*Davis et al.*, 2000; *Becker and Davis*, 2004]. Again, calculated effective permeabilities and diffusivities of a layered media are relatively insensitive to the underlying basement permeability. The sediment permeability used in the majority of Costa Rica FEM simulations was the low-end of measured permeability values for Costa Rica sediment, hydraulic conductivity κ=1e-10 m/s. However, it is important to test the sensitivity of the layered model to the overlying sediment permeability. Both low-end, κ=1e-10 m/s,

and high-end, κ=1e-8 m/s, hydraulic conductivities for fine-grained marine sediment [*Becker and Davis*, 2004; *Spinelli et al.*, 2004; *Davis and Villinger*, 2006] were used for the modeled sediment layer in 'permeability contrast' simulations (Section 4.3.3). Cutillo et al. [2006] use κ=1e-8 m/s for uncompacted high-porosity surface sediments in their Costa Rica FEM. Like in the box model study, flow rate predictions from the layered model are compared to predictions made in a homogeneous material model to determine the necessity of FEM to simulate deformation and fluid flow resulting from sudden slip (Table 1).

Like the design of the box model runs, the mesh at the near seafloor is sufficiently fine such that coseismic flow rate predictions can be made for the sudden slip simulations at times as low as ~10 s (τ= 4e-11). With the tilted rupture and the tilted seafloor geometry, τ is calculating using the average depth to the fault for d, and an effective diffusivity, c_{eff}, of the layered section between the fault center and the seafloor.

4.3.2. Initial and Displacement Boundary Conditions

Initial and boundary pore pressure conditions in the case study are identical to that of the box model studies. The displacement boundary conditions again satisfy the elliptical distribution as stated in equation (10) where b is now a vector with both x and y components so the imposed displacement is parallel to the dislocation plane. Also, it is necessary to replace x with $\bar{x}$, to account for ruptures on the decollement plane not centered at x=0

$$\bar{x} = |x - x_i| - \frac{V_r}{2} \tag{22}$$

where x_i is the rupture initiation location. The Costa Rica model simulations for sudden slip and slow propagating slip differ in that in the propagating model the length of the rupture L and therefore the maximum displacement over the rupture length, b, vary as a function of time, t, and speed of the propagating rupture tip, V_r

$$L(t) = V_r t \tag{23}$$

$$b(t) = b_f \frac{V_r t}{L_f} \tag{24}$$

for dimensionless rupture time τ_r

$$\tau_r = \frac{V_r t}{L_f} \leq 1 \tag{25}$$

where b_f and L_f are final maximum displacement and rupture length after propagation terminates, $\tau_r \geq 1$ (Figure 9). Modifying equation (10) by applying the coordinate shift in equation (22) and time dependencies, equations (23) and (25), the displacement distribution for the propagating rupture is:

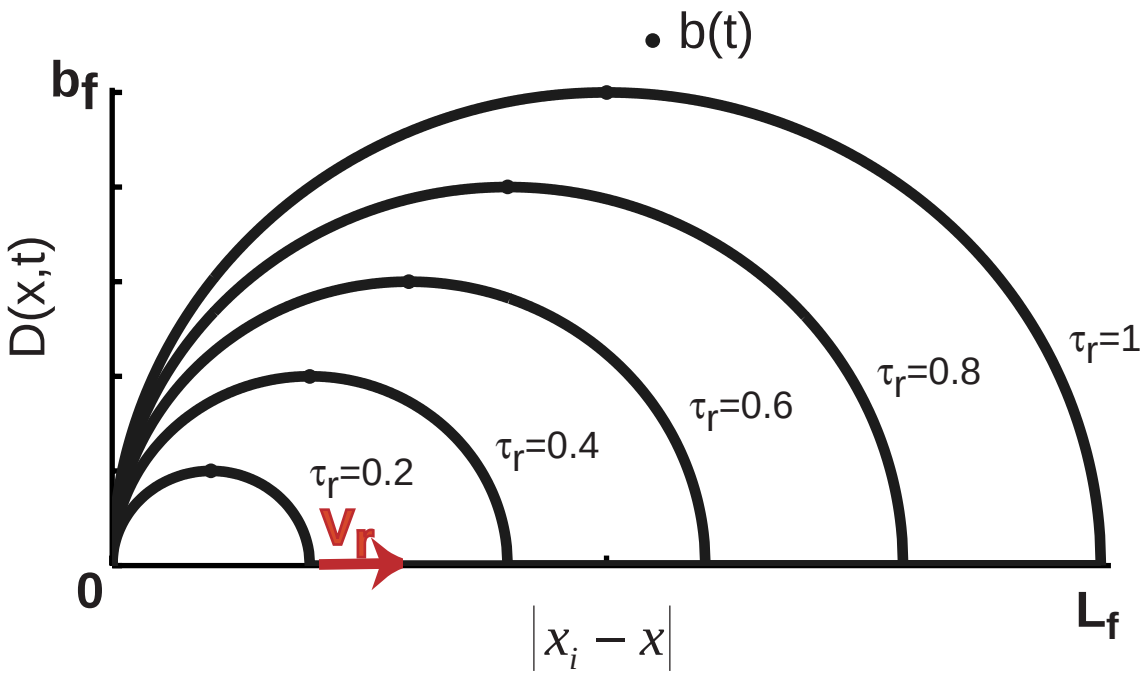

Figure 4-9: Schematic of displacement distribution, D(x,t), of a propagating dislocation for dimensionless rupture time $0<\tau_r\leq 1$. x-axis is shifted so rupture initiation location plots at the origin.

$$D(t) = \frac{b(t)\sqrt{\left(\frac{L(t)}{2}\right)^2 - \bar{x}^2}}{\frac{L(t)}{2}} \tag{26}$$

for

$$\bar{x} \leq \frac{L(t)}{2}. \tag{27}$$

With the change in sign convention as described in the box model methods section, positive displacement, b, designates thrust faulting as is desired in this subduction zone margin.

4.3.3. Costa Rica Pore Pressure-Displacement Simulations

The fully coupled Costa Rica sudden slip analyses were run in two ABAQUS "soils consolidation" steps, a 1e-6 s duration "instantaneous" coseismic step where the displacement boundary conditions are applied, and a postseismic step 10 s in duration. Simulations for a range of L/d values from 0.5 to 6 were run. These simulations were centered at a horizontal distance of 37 km from the toe, corresponding to a depth below the seafloor of 10 km. Rupture lengths ranged from 5 km to 60 km. The maximum rupture size of 60 km was chosen as ruptures longer than this would extend beneath the Nicoya peninsula into the freely slipping zone of microseismicity. The ratio of hydraulic conductivity of Costa Rica sediment, $\kappa_{sediment}$=1e-10 (Table 2), to that of

Costa Rica basement, $\kappa_{basement}$=1e-6, is 1e-4 in these runs. This ratio, $\kappa_{sediment}/\kappa_{basement}$, is hereafter referred to as the 'permeability contrast'.

A final set of sudden-slip FEM analyses in the Costa Rica geometry were designed to compare predictions from a homogeneous model to predictions from layered models with different permeability contrasts. The sudden-slip displacement for these analyses was on a near-field rupture, L/d=6. Costa Rica sediment, κ=1e-10m/s, is used in the homogeneous model. An upper layer sediment hydraulic conductivity of 1e-8 m/s rather than κ=1e-10m/s is used for the low-permeability contrast, $\kappa_{sediment}/\kappa_{basement}$=1e-2, layered model.

Propagating rupture simulations in the Costa Rica model geometry included updip and downdip propagating ruptures at speeds of 1-10 km/day over the full 60 km length, ie. between 7 km and 67 km distance from the trench. For the long event durations of 6-60 days, diffusion lengths are much longer. It is important that the fully coupled governing equations are used as was done in using the ABAQUS soils analysis procedure. The FEM model is again preformed in two steps, a propagation step, and a relaxation step. However, the length of the coseismic step where the displacement boundary condition is applied is the total duration of the rupture. Time iterations within the coseismic step are $1/100^{th}$ of the total rupture time. A postseismic drainage step follows the coseismic step. ABAQUS calculates and outputs fluid velocities as well as displacement and pore pressure fields for all simulations.

4.4. Results: Costa Rica Sudden-Slip FEM

The flexure related EF and CF superimpose on the pressure lobes CL and DL emanating from the rupture tip in the same manner as in the box model sudden slip simulations. In the far field, EF and CF are interior of CL and DL (Figure 10a) and in the near field the flexure and pressure lobe signatures overlap lying directly over the rupture tips (Figure 10b). Nondimensionalized vertical flow velocities at the seafloor for the range of L/d values tested are displayed (Figure 11). The same nondimensionalization of vertical fluid velocities used in the box model simulations, equation (19), is applied here. However, depth, d, effective diffusivity, c_{eff}, and effective permeability, κ_{eff}, vary with distance from the trench axis so the values of d, κ_{eff}, and c_{eff}, used in the nondimensionalization are calculated at the center of the rupture, 37 km distant from the trench axis, where depth from the seafloor to decollement is 10 km. The high amplitude predicted flow rate resulting from CL is a result of the shallow depth of the updip rupture tip, and likewise, the low amplitude DL is due to the relatively deep downdip rupture tip. Relative amplitudes of EF and CF compared to CL and DL are larger in the far field than in the near field.

Nondimensionalized vertical flow velocities at the seafloor for a homogenous marine sediment material simulation with L/d=6 is plotted for comparison (Figure 11). As in observed in the box model simulations (Figure 5), nondimensionalized layered and homogeneous material simulations for the Costa Rica geometry are not an exact match, but they are well within an order of magnitude of each other. An interesting result is obtained from a final FEM analysis with a lower permeability contrast between the basement and sediment layers, $\kappa_{sediment}/\kappa_{basement}$=1e-4 (Figure 11). The nondimensionalized results from the low permeability contrast simulation matches the

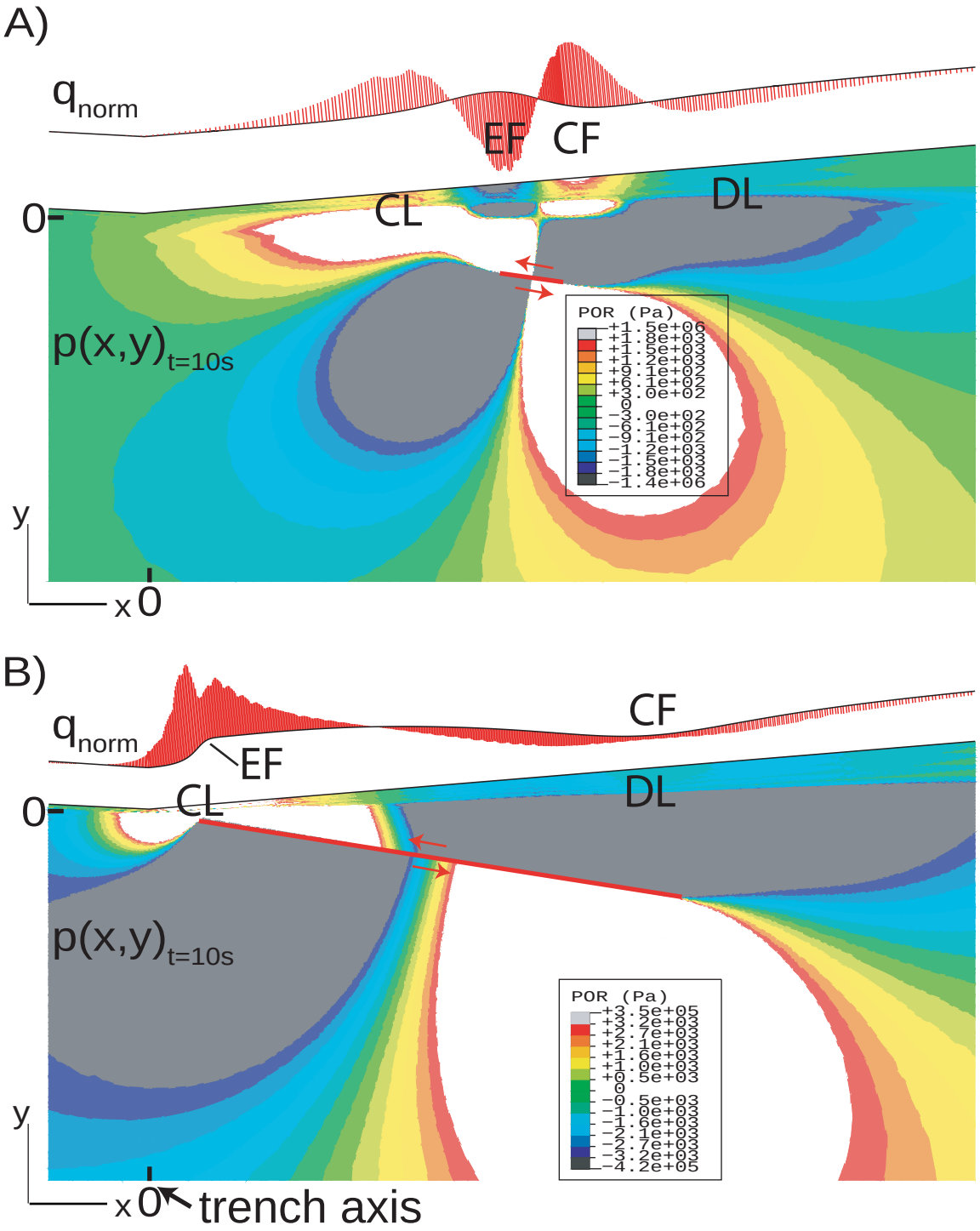

Figure 4-10. Coseismic response to sudden-slip thrust event with displacement b=1 m in layered Costa Rica sediment and Costa Rica basement material model (Figure 8, Table 2) approximated at dimensionless time τ=4e-11, or t=10 s. Vertical fluid flow rate through the deformed seafloor (vertically exaggerated), q_{norm}, and pore pressure field, p(x,y), where axes, across-strike distance, x, and depth, y, are the same scale, for A) far-field, L/d=0.5, and B) near-field, L/d=6, ruptures.

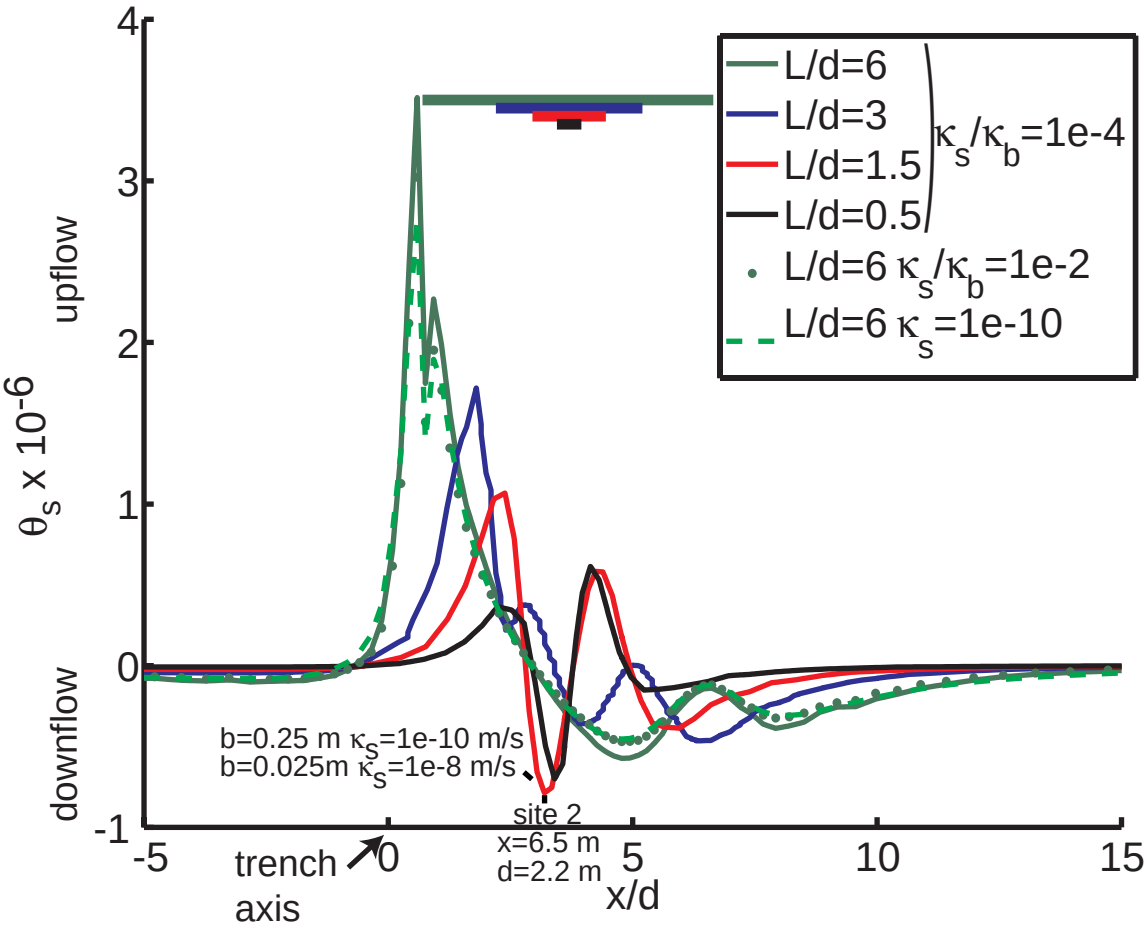

Figure 4-11: Costa Rica sudden-slip FEM predictions of dimensionless flow rate, θs, for 0.5<L/d<6 simulations in layered Costa Rica material model with high permeability contrast, κ_S =1e-10 m/s and κ_b =1e-6 m/s (solid lines). Included are predictions for low-permeability contrast layered material, κ_S =1e-8 m/s and κ_b =1e-6 m/s (green dotted sequence), and homogeneous sediment, κ_S =1e-10 m/s (green dashed line). Colored bars represent extent of rupture for each L/d value. Minimum displacement, b, required to produce observed downflow rate, q_0=-0.5 mm/day, at site 2 via a sudden-slip event is determined assuming site 2 is directly above negative peak in dimensionless flow rate at x/d=3. The observed flow rate is an average over 16 hours, a result of the flow meter sampling method. An equivalent smoothing is applied to the FEM predicted time series to calculate displacement. An observation depth, dobs, of 0.1 m is assumed. Minimum displacements are calculated for both κ_S =1e-10 m/s and κ_S =1e-8 m/s.

homogeneous material simulation results remarkably well suggesting that elevated flow rate predictions for the high permeability contrast layered model, $\kappa_{sediment}/\kappa_{basement}$=1e-2, could be a result of stresses induced by concentrated areas of pore pressure trapped beneath the confining layer.

4.5. Costa Rica FEM Results: Propagating Rupture

For both updip and downdip propagation simulations, snapshots in time of the spatial variability of vertical flow rates through the seafloor in response to a propagating rupture are presented (Figure 12a,b). Flow rate predictions are plotted as a new dimensionless term, θ_r, that is independent of rupture propagation speed, V_r:

$$\theta_r = \frac{q}{\left(\frac{\kappa\gamma G b_f \sqrt{\frac{V_r L_f}{4c}}}{\pi\rho g d^2} \right)} \tag{28}$$

The new correction term in equation (28) replaces the $\sqrt{\tau_0}$ in equation (19), and is the ratio of rupture speed to diffusion speed:

$$\sqrt{\frac{V_r L_f}{4c}} = \frac{V_r}{\sqrt{\frac{4c}{\frac{L_f}{V_r}}}}. \tag{29}$$

Values used in equation (28) for spatially varying parameters d, κ_{eff}, and c_{eff}, are calculated at the center of the final rupture length, $\left| x_i - L_f / 2 \right|$, 37 km distant from the trench. The subscript 'cent' is added to θ_r to specify these specific

nondimensionalization parameters used in dimensionless flow rate vs. across-strike distance plots (Figure 12a,b).

Each snapshot in dimensionless time, τ_r, can be interpreted as the across strike pattern of vertical flow rate through the seafloor at the completion of a rupture that propagated only a fraction of the total rupture length, L_f (Figure 9), and thus is a prediction for ruptures with a smaller L/d value. For example, at time τ_r =0.20 (Figure 12b), a 12 km updip propagating rupture has occurred. The seafloor flow rate pattern for this propagating rupture in the far field (L/d~1) is similar to the vertical seafloor flux pattern for the far field sudden slip solution (Figure 11). The sudden slip and propagating slip seafloor flow rate patterns diverge as the L/d value increases because with increasing rupture time, drainage through the seafloor dampens flow rate response in the propagating slip prediction as compared to the sudden slip prediction. Still, the same physical causes for change in the pressure field that drive flow rates in the sudden slip model still hold in both the far field and near field in the propagation model. For example, the spatial pattern produced from a propagating rupture in the near field has the same dimple effect above the rupture tips due to the superimposed signatures of EF and CF on CL and DL. The general snapshot image that results from this dimple effect in the downdip propagating rupture is two negative subpeaks straddling the propagating rupture tip location, and two positive subpeaks around the updip propagating rupture tip (Figure 12 a,b).

To illustrate possible seafloor flux time series that are generated by propagating updip and downdip ruptures, the velocity independent vertical flow rate solutions are

Figure 4-12. a,b) Snapshots of dimensionless flow rate predictions, $\theta_{r\text{-}cent}$, for downdip and updip propagating dislocations verses dimensionless across-strike distance, x/d, at dimensionless times, $0.2<\tau_r<1$. Colored bars represent extent of rupture at each τ_r value. c-l) Time series predictions for dimensionless along-fault distances, $0.05<\chi_r<1$. Dimensionless flow rates, $\theta_{r\text{-}cent}$ and $\theta_{r\text{-}x}$, are calculated using κ_{eff}, c_{eff}, and d values calculated above the center of the final rupture length and above the rupture at the specific along fault distance, respectively.

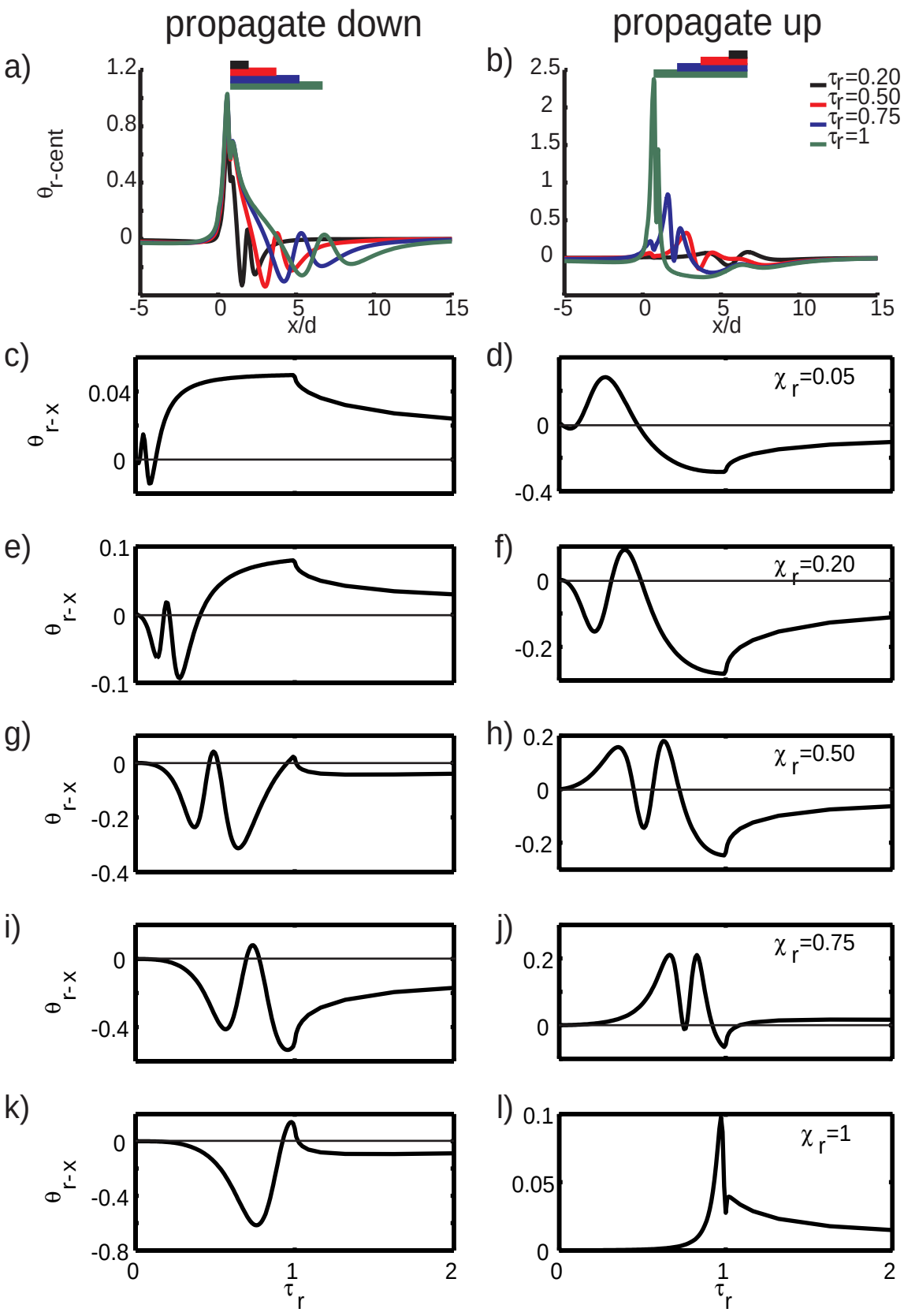
propagate down
propagate up
a)
b)
c)
d)
e)
f)
g)
h)
i)
j)
k)
l)
θr-cent
θr-x
x/d
τr=0.20
τr=0.50
τr=0.75
τr=1
χr=0.05
χr=0.20
χr=0.50
χr=0.75
χr=1
τr

plotted against dimensionless time τ_r (Figure 12c-l). The nondimensionalization for vertical fluid velocities plotted verses time is slightly different than $\theta_{r\text{-}cent}$ used in plots of flow rate verses across strike distance plots (Figure 12a and b). Since the observation point from where the time series measurement is made is fixed in space d, κ_{eff}, and c_{eff} for the specific observation location is used in the nondimensionalization $\theta_{r\text{-}x}$.

To understand the cause for each of the peaks in the time plots resulting from a propagating rupture at depth, it is instructive to refer to the fully coupled analytical solution for the pore pressure as a function of distance from the rupture tip and time due to a propagating edge dislocation in infinite space [*Roeloffs and Rudnicki*, 1984/85]. Roeloffs and Rudnicki explain the variation in pore pressure signal in space due to the passing of the rupture tip underneath the location of the measurement, also represents variation of pore pressure in time. Similarly, the variation in flow rate over time for a stationary observation point located above the rupture is similar to the pattern seen by an observation point that slides along the spatial plot (e.g. Figure 11) from out in front of the rupture tip, over the rupture tip, and continuing back behind the rupture tip above the ruptured fault.

In using this convolution concept to understand the cause for flow rate changes in the time series at different dimensionless along fault observation locations, χ_r, above a fault of finite length, L_f, where

$$\chi_r = \frac{|x - x_i|}{L_f}, \tag{30}$$

consider that the observation point sliding along the spatial plot starts at a finite distance before the termination location of the propagating rupture tip, and stops over the ruptured fault at a the same finite distance before the rupture initiation location x_i. As the observation point never passes over x_i, the flow signature with time recorded at an observation point anywhere over the final rupture length is primarily the signature of CL and EF for an updip propagating rupture, and DL and CF in the case of the downdip propagating rupture. Hence, like spatial plots (Figure 12a,b), time series plots (Figure 12c-l) have characteristic double downflow peaks for a downdip propagating rupture and double upflow peaks for an updip propagating rupture.

Instead of being the result of a simple convolution between an impulse function and the spatial flow rate result, as in the propagating edge dislocation problem, the time series due to propagation of a finite length rupture is the result of a more complicated convolution. The time series is a convolution of the spatial flow rate result and a function that varies in time, as both b and L are time dependent. Simply put, the effect of the convolution for a b increasing with time is the magnitudes of the fluid velocity at the seafloor will be more heavily weighted with increasing time.

5. Discussion

The predictions of seafloor flow rate response to both sudden and slow slip events in the modeled Costa Rica margin are used to investigate the possible rupture characteristics that could generate flow rates observed during the 2000 CRSEIZE. Specific recommendations for instrument placement along and across the subduction

zone forearc prism are made to better constrain rupture characteristics in future studies. Finally, the investigation of layered verses homogeneous material models suggests that short cuts to the fully coupled heterogeneous FEM can be made in certain situations.

5.1. Interpretation of Observed Flow Rates at Costa Rica

Brown et al. 2005 interpreted the subpeaks within the 2-3 week flow events observed (Figure 7) to be a result of inhomogeneities on the dislocation plane. Using FEM results to interpret the well defined downflow subpeaks in the time series recorded at site 2, 6.5 km from the trench axis, I suggest two potential alternatives: 1) Two consecutive short duration (less than one day) slip events occurred to generate the subpeaks in the site 2 time series, or 2) subpeaks are generated by a propagating aseismic dislocation with a three week duration.

Model results predict relatively large rates of downflow for a sudden slip event occurring on a rupture with $0.5<L/d<1.5$ (Figure 11). Recall the time series record of seafloor flow rates is a sharp step followed by decay as fluids drain through the seafloor and the driving pressure gradient deteriorates (Figure 4). The flow meter time series, however, will not capture this sharp peak, as the sampling method acts to average the flow rates over a window of 16 hours. Applying this smoothing effect to the sudden-slip FEM result, I obtain minimum displacements required to generate the observed $q = -0.5$mm/day (Figure 11). For high and low-end sediment permeabilities, respective displacements of 0.25 m and 0.025 m are required. This minimum displacement estimate assumes the updip limit of the $L/d=1.5$ rupture is 6.5 km back from the trench, i.e. the site 2 flow meter is recording the maximum downflow, θ_s=7.5e5. If the meter is

not actually located directly above the rupture tip, a larger displacement value is required. Dimensionalization parameters specific to the material section above the midpoint of the rupture, and an observation depth, d_{obs}, of 0.1 m, the approximate depth to which the flow meter chamber is inserted into the sediments, are used when calculating b using equation (19). While the centimeters to tens of centimeters displacement required to generate the observed downflow is not unreasonable, I reject this first hypothesis based on the lack of correlation in the timing of observed subpeaks at site 2 and site 3 (see Section 5.2). Furthermore, it is suspicious that this consecutive rupture pattern would be a frequent phenomenon: notice both recording flow meters exhibit the same doublet in flow rate during the second period of flow transience in the 6 month record (Figure 7).

The second alternative hypothesis, subpeak generation from a slowly propagating dislocation, seems likely as the time series looks similar to downdip propagating signatures at low to mid dimensionless distances along the fault, χ_r=0.2-0.5 (Figure 12e,g). A remarkable match of the observed record is made with the predicted time series at χ_r=0.4 (Figure 13). Using this result, and the constraint $x_i \geq 0$ as the trench axis limits the updip rupture initiation location, the rupture length, L_f, is a maximum of 15 km, rupturing from 0.5-15.5 km from the trench axis. The duration of the hypothesized propagating rupture event is easily constrained as the time between onset of increased flow rate and the peak before the final decay, or 3 weeks. This implies a propagating rupture speed, V_r, of 0.7 km/day.

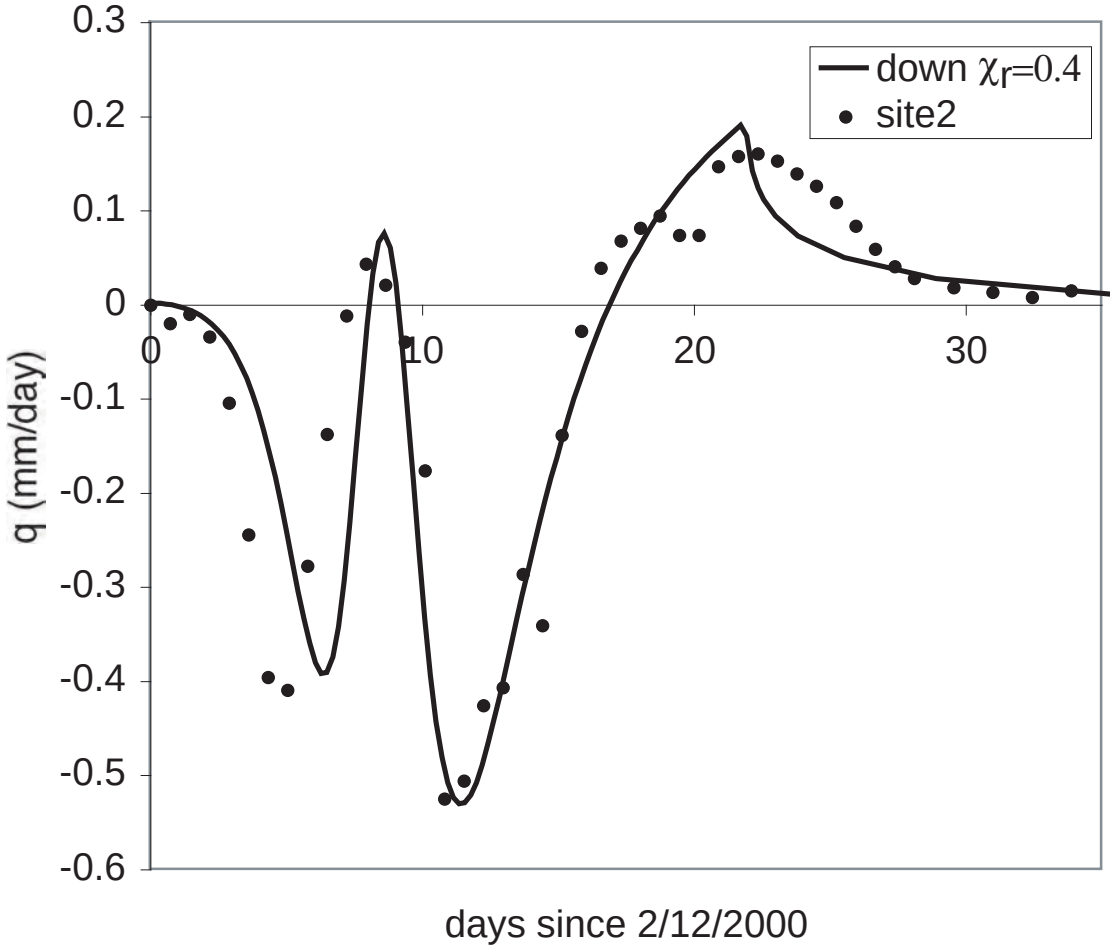

Figure 4-13: Downdip propagating FEM L/d=6 flow rate prediction with b=4.5 m, $d_{(\chi_{r=0.4})}$=1.75 km, Vr=0.7 km/day, and 22 day duration compared to observed flow rates at site 2, ~6.5 km distant from the trench axis. κ_{eff} and c_{eff} used to re-dimensionalize $\theta_{r\text{-}cent}$ are those calculated for the material section between the seafloor and dislocation at ~6.5 km distance from the trench, where high-end permeability Costa Rica sediment, κ_S=1e-8 m/s, and Costa Rica basement material properties are used (Table 2).

A slip displacement, b_f, of 4.5 m is calculated from the predicted $\theta_{r\text{-}x}$ result obtained at χ_r =0.4 (Figure 13) using equation (28). I used rupture velocity, V_r=0.7 km/day, and d, κ_{eff}, c_{eff}, parameters specific to the material section between the modeled dislocation plane and the observation site at x=6.5 km. At 6.5 km distant from the trench the depth from the seafloor to the dislocation is 1.75 km. The modeled basement fraction of this 1.75 km depth, l_1=0.55, and sediment fraction, l_2=0.45, are used in calculating the effective permeability and diffusivity using equations (20) and (21). The poroelastic moduli for Costa Rica basement and prism sediment are as specified in Table 2 but with a high-end sediment hydraulic conductivity, $\kappa_{sediment}$, of 1e-8 m/s.

This calculated displacement, b_f=4.5 m, is much larger than the 0.025 m displacement required to generate observed flow rates at site 2 for $\kappa_{sediment}$=1e-8 m/s via a sudden slip event (Figure 11). This difference is a result of the larger pressure head at the surface that results from an instantaneously applied strain, whereas there is a significant loss of pressure head as fluids drain through the surface over the duration of a slowly migrating slip event. The b_f =4.5 m displacement estimate is non unique. Shortening the rupture length, thus reducing the rupture speed, and increasing the displacement b_f would generate the same flow rates.

The calculated 4.5 m displacement is similar to the 4.25 m displacement that Cutillo et al. [2006] estimated for a great earthquake based on the plate convergence rate of 8.5 cm/yr and 50 yr recurrence interval. It is improbable that these aseismic slip events also only occur every 50 years, especially as we see 3 events in this <6 month observation period. Dragert [2001] geodetically observed an aseismic slip event in

Cascadia with a 2 cm displacement, equivalent to half a year of convergence between the Juan de Fuca and North American Plate. Ozawa [2001] interprets a slow slip event in the Nankai trough subduction zone with a total displacement of 5-20 cm as the release of 10 years of strain accumulated via convergence. However, 4.5 m of slip may not in fact be necessary.

Recalling the simplifications made in the Costa Rica FEM helps to explain the over-valued displacement estimate. One simplification that affects predicted flow rates is the constant dip angle of the dislocation plane used in order to obtain results that are representative for any spatial scale. The 10° arcward dip is an average of the steepening dip of the subducting slab over the 0-70km offshore subduction zone segment. When scaling the model to represent a shorter rupture length near the trench, the over-steep dip angle of the modeled rupture compared to the true depth of the decollement beneath the frontal prism introduced a model artifact. The depth of the modeled dislocation is too deep which results in undervalued predicted flow rates, and therefore a larger required displacement to reproduce the observed flow rates. The true depth of the decollement beneath site 2 is approximately 1.35 km, as opposed to the modeled depth of 1.75 km. As flow rate is a function of d^{-2}, a dislocation at the slightly shallower depth would produce a near doubling of the predicted flow rates,

$$\frac{\theta_{r(3°)}}{\theta_{r(10°)}} \propto \frac{{d_{(10°)}}^2}{{d_{(3°)}}^2} = \frac{1.75^2}{1.35^2} = 1.68 \tag{31}$$

and thus a lower required displacement, $b_f \approx 2.6$ m, to produce measured flow rate. A displacement of this size, releasing 30 years worth of accumulated strain at this subduction margin with a plate convergence rate of ~0.09 m/yr [*DeMets*, 2001], is still improbable.

Another simplification that makes the FEM prediction potentially unrepresentative of flow rates at the toe of the prism is the uniform material properties used for the sedimentary apron (Table 2). Relatively recently deposited trench fill sediments at the toe likely have a higher permeability due to higher porosities as they are not yet consolidated. Furthermore, the structure in the frontal prism deformation zone between the trench and the Nicoya basement complex backstop, ~5-7 km distant from the trench, is more complex [*Shipley et al.*, 1992]. Normal faults and out-of-sequence thrust faults are potential focused pathways for fluid escape, although Bolton [2001] states the prism sediments are not conducive to formation of fluid conduits. Finally, over- and under-pressured pore fluids in the near surface reservoir during the time of the dislocation may result nonlinear amplification of fluid outflow due to changes in porosity and permeability. In any case, if the substrate beneath the frontal prism at site 2 is indeed more permeable, a smaller displacement would be required to produce the observed flow rates. For example, a $\kappa_{sediment}$ of 1e-7 m/s requires a displacement, b_f of <0.9 m rather than the 2.6 m displacement required to push fluids through sediments with a hydraulic conductivity of 1e-8 m/s.

The two dimensionality of the rupture and subduction zone in the FEM is also potentially unrepresentative. Cascadia slow slip events observed to rupture along strike is one of many scenarios where the propagating rupture should be modeled in 3-D. In

the Costa Rica subduction zone, a discrepancy in flow direction was observed between sites 2, 3, and 5, suggesting that the rupture is propagating downdip at site 2 and 5, and updip at site 3. The distinct pattern in flow rate observed at site 3 (Figure 7) is remarkably similar to the predicted pattern observed for an updip propagating dislocation at χ_r=1 (Figure 12l). This suggests site 3 is above the updip limit of a updip propagating dislocation that has the same ~3 week duration. It is unlikely that propagations in opposite directions are occurring simultaneously and side-by-side. Instead, it is possible that the updip propagating dislocation terminating beneath site 3 occurs over a narrow patch. Off the edges of this patch dislocation, flow in the opposite direction as observed at sites 2 and 5 could occur. Perhaps a more feasible and simple explanation is that dislocation initiates along a line sub-parallel to the trench axis and propagates in both updip and downdip directions (Figure 6). Bidirectional slow-slip events have been observed in Cascadia [*Melbourne et al.*, 2005]. Either way, the dislocation must have three-dimensionality to simultaneously produce the observed records at sites 2, 3 and 5.

This interpretation, that a bidirectional slow slip event produced the observed hydrogeologic transients, suggests that the aseismic slip event initiated in the frontal prism. The larger question is: how does enough strain accumulate in the frontal prism to result in dislocation with no apparent connection to rupture events further downdip? It has been suggested that larger fault normal stresses build where the decollement dips more steeply at normal fault locations on the downgoing Cocos basement slab [*McIntosh and Sen*, 2000]. Furthermore, McIntosh and Sen [2000] find that there is significant along strike variation in the thinning of downgoing sediments in

coordination with the distribution of normal faults. Perhaps this basement topography and varying distribution of sediments between normal faults prevents the stable sliding that is expected to occur as the hydrous, velocity-strengthening, sediments of the frontal prism don't necessarily create a continuous slippery surface.

In previous observations of very shallow ruptures, [*Kanamori and Kikuchi*, 1993; *Polet and Kanamori*, 2000], the rupture initiated in the deeper seismogenic zone of the plate interface and propagated updip through the 'stable-sliding' zone. Polet and Kanamori explain the unstable sliding in the 'stable-sliding' zone during these tsunamogenic events off Nicaragua (1992), Java (1994), and Peru (1996), could be a result of the normal-faulted basement topography characteristic of the incoming subducting plate in all three locations. If basement topography does govern stress build-up and faulting in the shallow plate interface, is it possible that the stress potential could become large enough for independent initiation of episodic slip in the frontal prism as is suggested by these modeling results? Independent release of stress and strain in the shallow subduction zone is clearly important as much larger, more infrequent, dislocations were observed to result in tsunamis. Perhaps the shallow plate interface experiencing occasional self-initiated episodic slip can contribute to the tsunamogenic potential of the subduction thrust, should basement interactions be sufficiently large to store significant energy in these otherwise stable-sliding zones. However, the topography of the oceanic basement off Nicaragua is particularly anomalous, and the more frequent distribution of normal faulting there may allow for greater quantities of stored energy and shallow tsunami earthquakes, in contrast to the relatively smooth section of the Cocos plate in this CRSEIZE study area.

5.2. Optimal Instrumentation and Placement

There is an alternative to the hypothesis that a slow slipping rupture occurred to generate the subpeaks at site 2. Two consecutive short duration slip events could have occurred, and the smoothing effect from the flow meter's sampling method could make the characteristic sharp peak of a sudden slip event irresolvable in the temporal record. While this doesn't appear to be the case because OBS records are noisy for the entire three-week duration, and the subpeaks at sites 2, 3, and 5, don't line up with each other (Figure 7). This scenario demonstrates the importance of acquiring time series from multiple instruments.

Offshore seismometer measurements will help to confirm whether a deformation event has actually occurred, and an array of seismometers could help to locate that deformation event. As slow slip events are aseismic, a network of flow meters, preferably a flow meter with the low flow rate detection capability of the CAT meter and the high temporal resolution of the OTIS meter, is also essential to quanitfy the aseismic contribution to overall stress and strain in subduction zone systems.

Only two flow rate time series records were needed to rejecting the hypothesis that two consecutive sudden slip events occurred during the first period of observed flow transience. The subpeaks during the second period of flow transience line up (Figure 7), but this would also be expected for a rupture propagating perpendicular to the trench axis because both instruments are located ~7 km distant from the trench. This highlights the necessity of having an array of two flow meters both along strike and across strike. Unfortunately, with the sparse across strike spacing of the grid in the

CRSEIZE study, the nearest across strike instruments 15 km upslope did not register the deformation event.

If two across strike instruments both record flow transience and the subpeaks don't line up, implying slow slip deformation is potentially the cause of the subpeaks, the length and speed of the rupture can be constrained. The timing of subpeaks is unique for each dimensionless along fault distance, χ_r (Figure 12). By using the FEM propagation simulation results to determine χ_r for each instrument, and knowing the distance between the two instruments, it is simple to calculate the updip and downdip limits of the slow slip event. Determining along strike limits of a propagating rupture can presumably be achieved once the 3D propagation model has been constructed. For this reason, instruments should be in a grid as they were in the CRSEIZE study but perhaps more closely spaced in the across strike direction near the trench. If any instruments are placed on the incoming plate they should be within a few kilometers of the trench.

Unlike propagating events, temporal flow rate records resulting from sudden slip events all behave the same regardless of location of the recording flow meter (Figure 3). Therefore, matching the spatial variability of outflow to predicted variability is the only option to determine updip and downdip limits of sudden slip events. This would be unreasonable to attempt considering capturing the spatial complexity as predicted by sudden slip simulations of the Costa Rica subduction zone (Figure 11) would require ~500 m spacing at the trench axis with a linear increase to 5 km spacing at the continental shelf. Ship time and funds would be better spent in co-deploying a modest offshore seismometer array to detect locations of seismic events. With accurate

earthquake locations, displacement magnitudes could be constrained from the measured flow rate response to sudden slip as long as the sediment permeability is well constrained.

5.3. Short Cuts to FEM

The fully coupled half-space FEM is still required for propagation simulations as the rate of diffusion through the seafloor surface is greater than the rate of propagation of the fault, uncoupled models can be used to simulate sudden-slip displacement. The pore pressure field FEM result for sudden slip in a homogenous material shows good likeness to an analytical solution for coseismic strain field in half-space (Figure 14) [*Cutillo et al.*, 2006]. Cutillo et al. calculated the coseismic strain field using Okada's [1992] analytical solution that requires a homogeneous material half-space. The pore pressure field for the layered material model (Figure 8c) is very different at depth as fluids are trapped beneath the confining sedimentary layer, but the location and extent of regions of over- and under- pressured fluids in the surface sediment section still match that of the homogeneous field, and analytically predicted strain field.

The non-dimensionalized sudden-slip prediction in the homogeneous sediment model is well within an order of magnitude of the sudden slip prediction in the layered model (Figure 5,11). The implication of this result is that Okada's solution for sudden slip displacement in a homogeneous half-space can be used instead of an FEM by simply choosing effective permeabilities and diffusivities to represent a layered material. Furthermore, this effective homogeneous material approximation does an even

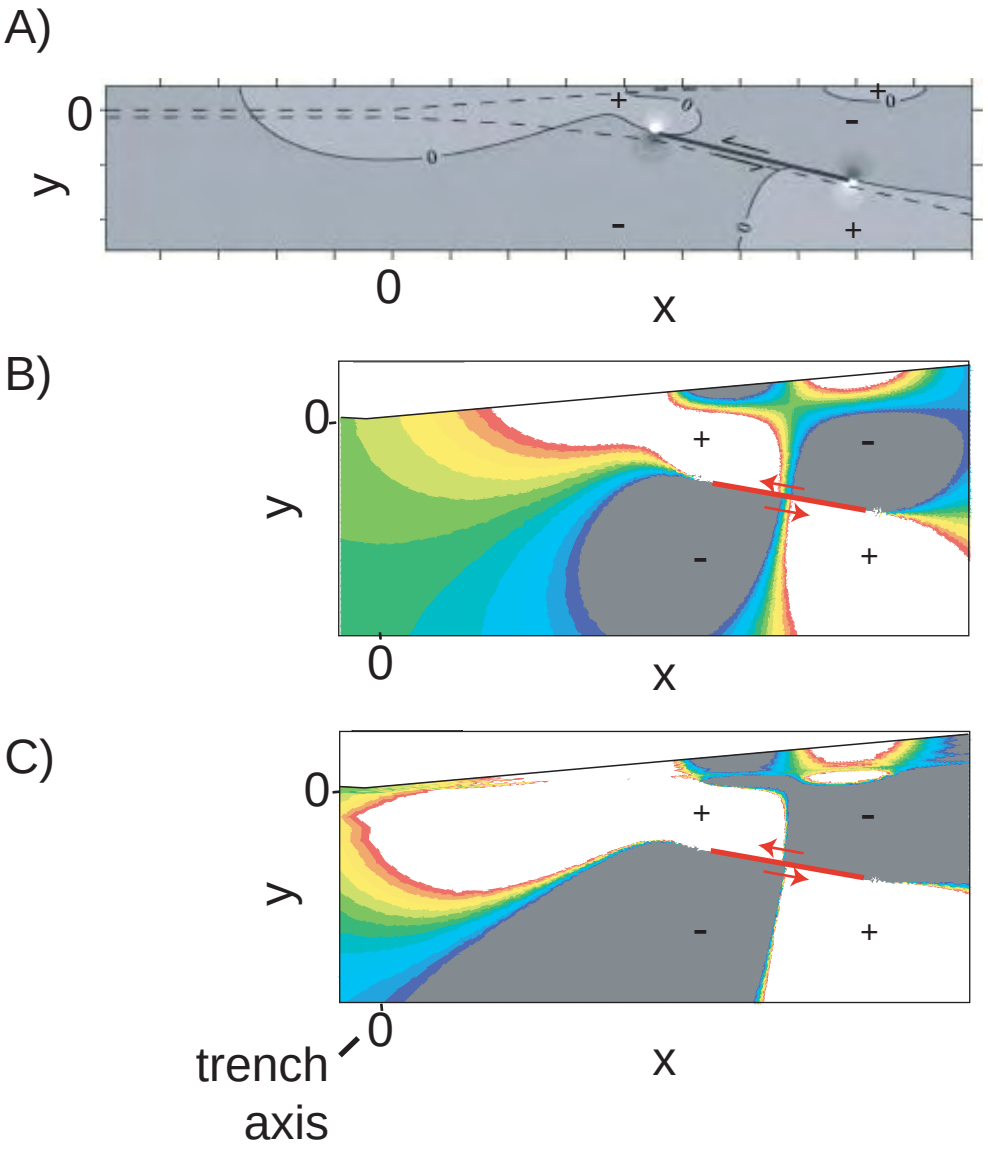

Figure 4-14: Comparison of solutions for a sudden-slip thrust rupture in models with Costa Rica geometry. Axes: across-strike distance, x, and depth, y, are the same scale A) Analytical strain field prediction in a homogeneous material [Cutillo et al., 2006] using Okada's solution [1992], B) FEM pore pressure field solution in homogeneous material, and C) and layered material $\kappa_{sediment}/\kappa_{basement}$=1e-4.

better job accurately predicting the result of a layered material with low permeability contrast (Figure 11).

6. Conclusions

In a brief sensitivity study, I determined that a layered subduction zone prism is effectively modeled with an equivalent homogenous material. Only mild differences would result if the 5° seafloor surface is reduced to a flat surface. With these simplifications, the existing uncoupled analytical solution for deformation in a homogeneous half-space can be used to make predictions of surface flow resulting from sudden-slip, i.e. seismic, deformation.

Ideal flow meter spacing at the toe of the margin is on the order of a few kilometers in the across strike direction. Fortunately, this is feasible as the flow meters developed in the Hydrogeology and Tectonic Studies laboratory are easy to deploy and relatively inexpensive. Future deployments should also include seismometers to help constrain rupture locations and confirm whether a hydrogeologic event related to a deformation event, and whether that event is seismic or aseismic. Finally, it is crucial that material properties, such as poroelastic moduli and permeabilities, are well constrained in the study area to be able to use these modeling techniques to infer the size of deformation events.

Although a number of complexities are not modeled in this preliminary FEM study, e.g. steepening dip of the decollement, different frontal prism material properties, out-of-sequence thrust faults, the predicted patterns of flow rate at the seafloor surface for propagating slow-slip events are likely insensitive to these complexities. The

predicted flow rate time series at different dimensionless along-fault distances are conveniently unique. While a new 3-D FEM with tailored geometry and material properties to better represent the Costa Rica frontal prism would be helpful to accurately reproduce CRSEIZE hydrogeologic observations, I am able to preliminarily interpret the hydrogeologic event on the toe by matching the unique time series to the 2-D FEM predictions. A bidirectional slow-slip event along the shallow plate interface, initiating along a line subparallel to the trench axis, would reproduce the downflow and upflow observations at the two flow meter sites. The normal-faulted subducting Cocos plate could be catching on the overlying prism, and this basement topography could be the potential cause for independent initiation of slow-slip events in the shallow subduction zone.

This first modeling study to predict patterns of flow rates at the seafloor surface as a result of deformation along the decollement of subduction zones is a stepping stone to more complex modeling and a better understanding of interseismic deformation in subduction zone systems. Quantitative estimates of stress and strain build up and release through aseismic deformation in the offshore environment are possible through modeling and empirical measurements from offshore seismometers and flow meters that are sensitive to slow slip events. Assuming the number and variety of monitoring instrumentation at subduction zones will multiply with the advent of ocean observatories such as ORION, modeling as was done in this study will be a critical component in scientists' efforts to condense the data sets and improve knowledge of earthquake cycle processes in subduction zone environments that pose a significant seismic hazard and are potentially tsunamogenic.

References

Barckhausen, U., C.R. Ranero, R. von Huene, S.C. Cande, and H.A. Roeser (2001), Revised tectonic boundaries in the Cocos Plate off Costa Rica: Implications for the segmentation of the convergent margin and for plate tectonic models, *Journal of Geophysical Research-Solid Earth*, *106*, 19207-19220.

Becker, K., and E.E. Davis (2004), In situ determinations of the permeability of the igneous oceanic crust, in *Hydrogeology of the Oceanic Lithosphere*, edited by E.E. Davis, and H. Elderfield, pp. 189-224, University Press, Cambridge.

Biot, M.A. (1941), General theory of three-dimensional consolidation, *Journal of Applied Physics*, *12*, 155-164.

Bolton, A.J., P. Vannucchi, M.B. Clennell, and A. Maltman (2001), Microstructural and geomechanical constraints on fluid flow at the Costa Rica convergent margin, Ocean Drilling Program Leg 170, in *Proceedings of the Ocean Drilling Program, Scientific Results*, edited by E.A. Silver, G. Kimura, and T.H. Shipley, *170*, pp. 1-32, Ocean Drilling Program, Texas A&M University, College Station, TX.

Booker, J.R. (1974), Time-Dependent Strain Following Faulting of a Porous-Medium, *Journal of Geophysical Research*, *79*, 2037-2044.

Bosl, W.J., and A. Nur (2002), Aftershocks and pore fluid diffusion following the 1992 Landers earthquake, *Journal of Geophysical Research-Solid Earth*, *107*(B12), 2366, doi:10.1029/2001JB000155.

Bredehoeft, J.D. (1967), Response of Well-Aquifer Systems to Earth Tides, *Journal of Geophysical Research*, *72*, 3076-3087.

Brown, K.M., B. Bekins, B. Clennell, D. Dewhurst, and G. Westbrook (1994), Heterogeneous Hydrofracture Development and Accretionary Fault Dynamics, *Geology*, *22*, 259-262.

Brown, K.M., M.D. Tryon, H.R. DeShon, L.M. Dorman, and S.Y. Schwartz (2005), Correlated transient fluid pulsing and seismic tremor in the Costa Rica subduction zone, *Earth and Planetary Science Letters*, *238*, 189-203.

Carslaw, H.S., and J.C. Jaeger (1959), *Conduction of heat in solids*, 510 pp., Oxford University Press, USA.

Christeson, G.L., K.D. McIntosh, T.H. Shipley, E.R. Flueh, and H. Goedde (1999), Structure of the Costa Rica convergent margin, offshore Nicoya Peninsula, *Journal of Geophysical Research-Solid Earth*, *104*, 25443-25468.

Cutillo, P.A., S. Ge, and E. Screaton (2006), Hydrodynamic response of subduction zones to seismic activity: A case study for the Costa Rica Margin, *Tectonophysics*, *426*, 167-187.

Davis, E.E., and H.W. Villinger (2006), Transient formation fluid pressures and temperatures in the Costa Rica forearc prism and subducting oceanic basement: CORK monitoring at ODP Sites 1253 and 1255, *Earth and Planetary Science Letters*, *245*, 232-244.

Davis, E.E., K. Wang, K. Becker, and R.E. Thomson (2000), Formation-scale hydraulic and mechanical properties of oceanic crust inferred from pore pressure response to periodic seafloor loading, *Journal of Geophysical Research-Solid Earth*, *105*, 13423-13435.

Davis, E.E., K. Wang, R.E. Thomson, K. Becker, and J.F. Cassidy (2001), An episode of seafloor spreading and associated plate deformation inferred from crustal fluid pressure transients, *Journal of Geophysical Research-Solid Earth*, *106*, 21953-21963.

DeMets, C. (2001), A new estimate for present-day Cocos-Caribbean plate motion: Implications for slip along the Central American volcanic arc, *Geophysical Research Letters*, *28*, 4043-4046.

Di Marco, G., Baumgartner, P.O. and Channell. J.E.T. (1995.), Late Cretaceous-early Tertiary paleomagnetic data and a revised tectonostratigraphic subdivision of Costa Rica and western Panama., in *Geologic and Tectonic Development of the Caribbean Plate Boundary in Southern Central America*, edited by P. Mann, *295*, pp. 1-27, Spec. Pap. Geol. Soc. Am., Boulder, Colo.

Dragert, H., K.L. Wang, and T.S. James (2001), A silent slip event on the deeper Cascadia subduction interface, *Science*, *292*, 1525-1528.

Fialko, Y. (2004), Temperature fields generated by the elastodynamic propagation of shear cracks in the Earth, *Journal of Geophysical Research-Solid Earth*, *109*, B01303, doi:10.1029/2003JB002497.

Ge, S.M., and S.C. Stover (2000), Hydrodynamic response to strike- and dip-slip faulting in a half-space, *Journal of Geophysical Research-Solid Earth*, *105*, 25513-25524.

Ghosh, A., A.V. Newman, A.M. Thomas, and G.T. Farmer (2006), Variability in Shallow Subduction Zone Locking Inferred From Earthquake Activity Near Nicoya Peninsula, Costa Rica, *Eos Trans. AGU*, *87*(52), Fall Meet. Suppl., Abstract T11G-02.

Guendel, F. (1986), Seismotectonics of Costa Rica: an analytical view of the southern terminus of the Middle American Trench, Ph.D. thesis, University of California, Santa Cruz.

Harris, R.N., and K. Wang (2002), Thermal models of the middle America trench at the Nicoya Peninsula, Costa Rica, *Geophysical Research Letters*, *29*(21), 2010, doi:10.1029/2002GL015406.

Hinz, K., R. VonHuene, C.R. Ranero, E. Flueh, D. Klaeschen, J. Leinbach, O. Ruoff, H.O. Bargeloh, M. Block, J. Fritsch, P. Kewitsch, H. Meyer, B. Schreckenberger, and I. Mrazek (1996), Tectonic structure of the convergent Pacific margin offshore Costa Rica from multichannel seismic reflection data, *Tectonics*, *15*, 54-66.

Hyndman, R.D., K. Wang, T. Yuan, and G.D. Spence (1993), Tectonic Sediment Thickening, Fluid Expulsion, and the Thermal Regime of Subduction Zone Accretionary Prisms - the Cascadia Margin Off Vancouver-Island, *Journal of Geophysical Research-Solid Earth*, *98*, 21865-21876.

Hyndman, R.D., M. Yamano, and D.A. Oleskevich (1997), The seismogenic zone of subduction thrust faults, *Island Arc*, *6*, 244-260.

Johnson, A.G., R.L. Kovach, and A. Nur (1973), Pore Pressure Changes During Creep Events on San-Andreas Fault, *Journal of Geophysical Research*, *78*, 851-857.

Jonsson, S., P. Segall, R. Pedersen, and G. Bjornsson (2003), Post-earthquake ground movements correlated to pore-pressure transients, *Nature*, *424*, 179-183.

Kanamori, H., and M. Kikuchi (1993), The 1992 Nicaragua Earthquake - a Slow Tsunami Earthquake Associated with Subducted Sediments, *Nature*, *361*, 714-716.

Kimura, G., E. Silver, and P. Blum (1997), Proc. ODP, Init Repts., *170*, pp. 458, Ocean Drilling Program, College Station, TX.

King, G.C.P., R.S. Stein, and J.B. Rundle (1988), The Growth of Geological Structures by Repeated Earthquakes .1. Conceptual-Framework, *Journal of Geophysical Research-Solid Earth and Planets*, *93*, 13307-13318.

Klitgord, K.D., and J. Mammerickx (1982), Northern East Pacific Rise - Magnetic Anomaly and Bathymetric Framework, *Journal of Geophysical Research*, *87*, 6725-6750.

Kyaar, K.A., and V.A. Vares (1982), Calculation of the effective thermal diffusivity of heterogeneous layered material, *Journal of Engineering Physics and Thermophysics*, *43*, 768-773.

Lawn, B. (1993), *Fracture of Brittle Solids*, 378 pp., Cambridge Univ. Press, New York.

Lee, M., T.K. Liu, K.F. Ma, and Y.M. Chang (2002), Coseismic hydrological changes associated with dislocation of the September 21, 1999 Chichi earthquake, Taiwan, *Geophysical Research Letters*, *29*(17), 1824, doi:10.1029/2002GL015116.

Masterlark, T., and H.F. Wang (2002), Transient stress-coupling between the 1992 Landers and 1999 Hector Mine, California, earthquakes, *Bulletin of the Seismological Society of America*, *92*, 1470-1486.

McIntosh, K.D., and M.K. Sen (2000), Geophysical evidence for dewatering and deformation processes in the ODP Leg 170 area offshore Costa Rica, *Earth and Planetary Science Letters*, *178*, 125-138.

Melbourne, T.I., W.M. Szeliga, M.M. Miller, and V.M. Santillan (2005), Extent and duration of the 2003 Cascadia slow earthquake, *Geophysical Research Letters*, *32*(4), L04301, doi:10.1029/2004GL021790.

Melbourne, T.I., and F.H. Webb (2003), Slow but not quite silent, *Science*, *300*, 1886-1887.

Morris, J.D., H.W. Villinger, and A. Klaus (2003), *Proc. ODP, Init. Repts., 205 [Online]*, http://www-odp.tamu.edu/publications/205_IR/205ir.htm.

Newman, A.V., S.Y. Schwartz, V. Gonzalez, H.R. DeShon, J.M. Protti, and L.M. Dorman (2002), Along-strike variability in the seismogenic zone below Nicoya Peninsula, Costa Rica, *Geophysical Research Letters*, *29*(20), 1977, doi:10.1029/2002GL015409.

Norabuena, E., T.H. Dixon, S. Schwartz, H. DeShon, A. Newman, M. Protti, V. Gonzalez, L. Dorman, E.R. Flueh, P. Lundgren, F. Pollitz, and D. Sampson (2004), Geodetic and seismic constraints on some seismogenic zone processes in Costa Rica, *Journal of Geophysical Research-Solid Earth*, *109*, B11403, doi:10.1029/2003JB002931.

Okada, Y. (1985), Surface Deformation Due to Shear and Tensile Faults in a Half-Space, *Bulletin of the Seismological Society of America*, *75*, 1135-1154.

Okada, Y. (1992), Internal Deformation Due to Shear and Tensile Faults in a Half-Space, *Bulletin of the Seismological Society of America*, *82*, 1018-1040.

Ozawa, S., M. Murakami, and T. Tada (2001), Time-dependent inversion study of the slow thrust event in the Nankai trough subduction zone, southwestern Japan, *Journal of Geophysical Research-Solid Earth*, *106*, 787-802.

Polet, J., and H. Kanamori (2000), Shallow subduction zone earthquakes and their tsunamigenic potential, *Geophysical Journal International*, *142*, 684-702.

Protti, M., V. Gonzalez, T. Kato, T. Iinuma, S. Miyazaki, K. Obana, Y. Kaneda, P. La Femina, T. Dixon, and S.Y. Schwartz (2004), A Creep Event on the Shallow Interface of the Nicoya Peninsula, Costa Rica Seismogenic Zone, *Eos Trans. AGU*, *85*(47), Fall Meet. Suppl., Abstract S41D-07.

Protti, M., K. McNally, J. Pacheco, V. Gonzalez, C. Montero, J. Segura, J. Brenes, V. Barboza, E. Malavassi, F. Guendel, G. Simila, D. Rojas, A. Velasco, A. Mata, and W. Schillinger (1995), The March 25, 1990 (M(W)=7.0, M(L)=6.8), Earthquake at the Entrance of the Nicoya Gulf, Costa-Rica - Its Prior Activity, Foreshocks, Aftershocks, and Triggered Seismicity, *Journal of Geophysical Research-Solid Earth*, *100*, 20345-20358.

Quilty, E.G., and E.A. Roeloffs (1997), Water-level changes in response to the 20 December 1994 earthquake near Parkfield, California, *Bulletin of the Seismological Society of America*, *87*, 310-317.

R. M. McKinley, H.O.J., W. W. Harris, R. A. Greenkorn, (1966), Non-Newtonian flow in porous media, *AIChE Journal*, *12*, 17-20.

Rice, J.R., and M.P. Cleary (1976), Some Basic Stress Diffusion Solutions for Fluid-Saturated Elastic Porous-Media with Compressible Constituents, *Reviews of Geophysics*, *14*, 227-241.

Roeloffs, E. (1996), Poroelastic techniques in the study of earthquake-related hydrologic phenomena, in *Advances in Geophysics, Vol 37*, *37*, pp. 135-195.

Roeloffs, E., and J.W. Rudnicki (1984/85), Coupled Deformation-Diffusion Effects on Water-Level Changes Due to Propagating Creep Events, *Pure and Applied Geophysics*, *122*, 560-582.

Rogers, G., and H. Dragert (2003), Episodic tremor and slip on the Cascadia subduction zone: The chatter of silent slip, *Science*, *300*, 1942-1943.

Rojstaczer, S., and D.C. Agnew (1989), The Influence of Formation Material Properties on the Response of Water Levels in Wells to Earth Tides and Atmospheric

Loading, *Journal of Geophysical Research-Solid Earth and Planets*, *94*, 12403-12411.

Rudnicki, J.W. (1986), Slip on an impermeable fault in a fluid-saturated rock mass., in *Earthquake Source Mechanics, Geophys. Monograph Ser.*, edited by Das, Boatwright, and Scholz, *37*, pp. 81-89, American Geophysical Union, Washington, D.C.

Rudnicki, J.W. (1987), Plane-Strain Dislocations in Linear Elastic Diffusive Solids, *Journal of Applied Mechanics-Transactions of the Asme*, *54*, 545-552.

Rudnicki, J.W., J. Yin, and E.A. Roeloffs (1993), Analysis of Water-Level Changes Induced by Fault Creep at Parkfield, California, *Journal of Geophysical Research-Solid Earth*, *98*, 8143-8152.

Salazar, A., A. Sanchez-Lavega, and J.M. Terron (1998), Effective thermal diffusivity of layered materials measured by modulated photothermal techniques, *Journal of Applied Physics*, *84*, 3031-3041.

Sallares, V., J.J. Danobeitia, and E.R. Flueh (2000), Seismic tomography with local earthquakes in Costa Rica, *Tectonophysics*, *329*, 61-78.

Scholz, C.H. (1998), Earthquakes and friction laws, *Nature*, *391*, 37-42.

Schwartz, S.Y., and H.R. DeShon (2006), *Distinct Up-dip Limits to Geodetic Locking and Microseismicity at the Northern Costa Rica Seismogenic Zone: Evidence for Two Mechanical Transitions, in Interplate Subduction Zone Seismogenesis*, Columbia Univerisity Press, New York.

Shipley, T.H., K.D. McIntosh, E.A. Silver, and P.L. Stoffa (1992), 3-Dimensional Seismic Imaging of the Costa-Rica Accretionary Prism - Structural Diversity in a Small Volume of the Lower Slope, *Journal of Geophysical Research-Solid Earth*, *97*, 4439-4459.

Spinelli, G.A., E.R. Giambalvo, and A.T. Fisher (2004), Sediment permeability, distribution, and influence on fluxes in oceanic basement, in *Hydrogeology of the Oceanic Lithosphere*, edited by E.E. Davis, and H. Elderfield, pp. 151-188, University Press, Cambridge.

Spinelli, G.A., and D.M. Saffer (2004), Along-strike variations in underthrust sediment dewatering on the Nicoya margin, Costa Rica related to the updip limit of seismicity, *Geophysical Research Letters*, *31*(4), L04613, doi:10.1029/2003GL018863.

Toutain, J.P., and J.C. Baubron (1999), Gas geochemistry and seismotectonics: a review, *Tectonophysics*, *304*, 1-27.

Tryon, M., K. Brown, L.R. Dorman, and A. Sauter (2001), A new benthic aqueous flux meter for very low to moderate discharge rates, *Deep-Sea Research Part I-Oceanographic Research Papers*, *48*, 2121-2146.

Turcotte, D.L., and G. Schubert (2002), *Geodynamics*, 456 pp., Cambridge Univ. Press, Cambridge.

von Huene, R. (1985), Site 565, *Initial Rep. Deep Sea Drill. Proj.*, *84*, 21-77.

von Huene, R., C.R. Ranero, W. Weinrebe, and K. Hinz (2000), Quaternary convergent margin tectonics of Costa Rica, segmentation of the Cocos Plate, and Central American volcanism, *Tectonics*, *19*, 314-334.

Wang, H.F. (1997), Effects of deviatoric stress on undrained pore pressure response to fault slip, *Journal of Geophysical Research-Solid Earth*, *102*, 17943-17950.

Wang, H.F. (2000), *Theory of linear poroelasticity with applications to geomechanics and hydrogeology*, 287 pp., Princeton Univ. Press, Princeton, NJ.

Wang, K.L., and E.E. Davis (1996), Theory for the propagation of tidally induced pore pressure variations in layered subseafloor formations, *Journal of Geophysical Research-Solid Earth*, *101*, 11483-11495.

Wesson, R.L. (1981), Interpretation of Changes in Water Level Accompanying Fault Creep and Implications for Earthquake Prediction, *Journal of Geophysical Research*, *86*, 9259-9267.

Ye, S., J. Bialas, E.R. Flueh, A. Stavenhagen, R. vonHuene, G. Leandro, and K. Hinz (1996), Crustal structure of the middle American trench off Costa Rica from wide-angle seismic data, *Tectonics*, *15*, 1006-1021.

Chapter 5

Conclusions

Like onshore records of water table height, well height and spring flow change in response to tectonic deformation events, flow rate at the ambient seabed and flow from submarine hydrologic seeps respond to tectonic events at all types of active margins. Observations and interpretation of flow response to volumetric strain in a transform margin (Monterey Bay), a convergent margin (the Costa Rica subduction zone), and a triple junction (the Nootka transform fault-Cascadia subduction zone) are investigated in this thesis. The investigation of the hydro-tectonics at these study sites was completed using newly developed instrumentation and finite element modeling (FEM). Each study was conducted at a different type of plate boundary, with a different set of instruments, and on different hydrogeologic structures, seeps or the ambient seabed [Chapter 1, Section 5]. The better known tectonic structure, and the types of instrumentation deployed at Monterey Bay and the Costa Rica margin, made interpretation of the hydrogeologic measurements from these study sites more clear cut than those gathered at the Nootka study site. One conclusion is clear, a combination of the best of all the attributes that each of these studies had to offer, i.e. real-time long-term monitoring using ample flow meter instrumentation with high temporal resolution and accuracy at both seeps and the ambient seabed and an array of seismometers, could provide significant insight into the dynamics of subduction zone margins, and potentially transform and divergent margins as well.

Chapter 2 was a demonstration of the capacity of the newly developed sediment-water interface (SWI) flow meter, the Optical Tracer Injection System (OTIS), to detect transient deformation events in the offshore environment at high temporal resolution and accuracy. During this first deep-water three-month test deployment, the OTIS

cleanly resolved high frequency tidal variability, and if a tectonic deformation had occurred during this short duration, we are confident the OTIS meter would have captured it. While no tectonic deformation events were recorded with the OTIS in the Monterey Bay deployment at a rapidly flowing seep site, the temporal accuracy and resolution of the new OTIS meter allowed for determination of the structure of the hydrologic seep. Tidal overburden pressure and flow rate where observed to be in phase, much like the barometric response of a well tapping a confined aquifer. This result implies a highly permeable conduit connects the seep to a confined aquifer at depth. This is confirmed by measured helium isotopic ratios, which suggest the seep is tapping a deep source. Perhaps the seep is a continuation of a buried vertical strike-slip fault through to the surface. Temperature and chemistry records allowed us to place bounds on the depth to which the seep was sourced, or the depth of the confined aquifer.

Temperature and flow rate time series records do not vary together over the long term, as they do over short period tidal oscillations. We interpret this to mean the system has at least two mixing fluid sources, perhaps that of the confined aquifer at depth and the colder overlying sediment layer, whose relative contributions vary in time. With higher resolution chemical time series, it may be conceivable to use chemistry to tell us about whether the hydrogeologic response to a tectonic deformation event is due to permeability, dynamic strain, or volumetric strain. For example, imagine if a dynamic strain causes liquifaction of the surface sediments. One might expect to see a higher relative fluid contribution from shallow sources than at previous times. Conversely, imagine if a rupture occurs at depth. The resulting volumetric strain field decays with distance from the fault, i.e. lower volumetric strain closer to the seafloor

surface, so one might expect a lower relative fluid contribution from the sediment to that from the confined aquifer following the rupture.

In the Nootka transform fault-Cascadia subduction zone triple junction study [Chapter 3] was primarily an instrument test. The OTIS meter served as the seafloor platform for other hydrologic instruments, a central data logger, and acoustic modem. Data acoustically transmitted from this seafloor hydrologic node to a surface buoy was then relayed via satellite to the desktop for near real-time viewing. Although the acoustic modem arrived at the last minute, allowing for only a single simple test, the successful data transfer from the seafloor hydronode was a major technical achievement. It is not surprising the scientific results from the hydronode didn't match the caliber of the technical results as the placement of the buoy mooring earlier in the year was at some distance from any promising looking hydrologic seeps.

A small spatial array of chemical aqueous transport (CAT) meters was also deployed in a seep area nearby. Four roughly-correlating discrete flow events were recorded in the time series. The hypothesis that these regional flow transients resulted from volumetric strain coincident with seismic deformation, and likely concurrent aseismic deformation as well, was developed from comparisons of flow rate records with onshore and offshore seismometer records. Without the temporal accuracy and resolution of the OTIS, these correlations were not as crisp as is needed to form any strong mechanistic conclusions from the data. Even if we can assume events are responding to tectonic deformation derived from volumetric strain, determination of dislocation parameters is ominously more difficult because the triple junction area is

complicated with conjugate fault sets and the location of the instrumented seep site with respect to the structure is unknown.

The Costa Rica hydro-tectonic study is the best illustration of the possible power of hydrogeologic measurements at the SWI to infer tectonic deformation. CAT meters were deployed in a grid with 15 km spacing over the subduction zone margin during the experiment in 2000. Three flow events at the frontal prism were observed to correlate over a 30 km along strike distance. The flow-rate time series of these 22-day flow excursions have very distinct properties, namely two subpeaks of the same sign, i.e. both upflow, or both downflow. Furthermore, co-deployed Ocean Bottom Seismometers (OBS) recorded low frequency noise throughout the 22-day duration of transient hydrogeologic events. It is therefore reasonable to assume that the events are significant and potentially of tectonic origin. Using a sophisticated FEM, I show that these unique records can be explained in terms of an aseismic dislocation that propagates both up and down dip under the instruments from an initiation location between the instruments.

Developing a FEM to compare predicted and observed flow rates is relatively straight forward for this Costa Rica subduction zone study because the two potential additional degrees of freedom are constrained. 1) Unlike the unknown exact depth of overpressured confined aquifer driving flow at the instrumented seep site in Monterey Bay, the CAT meter instruments were deployed on the ambient seabed, and thus simply responded to the near seafloor pressure gradient. 2) Unlike the unknown fault location in the Nootka study, it is safe to say the deformation occurs somewhere on the decollement, the detachment surface that is relatively well constrained through seismic imaging.

Before applying the modeling technique, I first need to justify that the flow-rate transients were a result of volumetric strain caused by the deformation rather than an alternative mechanism for pressure change in response to deformation. If the flow transients are aseismic, as suggested by the OBS data, it is reasonable to believe that neither permeability changes, nor dynamic strain in association with shaking, are the likely cause of flow rate transients. The assumption is then made that the tectonic mechanism for flow rate generation is near surface volumetric strain associated with a propagating aseismic dislocation along the decollement. With these criteria met, I developed a poro-elastic model to determine if a propagating aseismic dislocation along the decollement could indeed generate the unique flow rate time series observed at the three near-trench CAT meters.

The poro-elastic FEM is fully coupled, i.e. pore fluid diffusion is allowed to occur throughout the deformation part of the numerical simulation, and designed to approximate the geometry and material properties of the Costa Rica subduction zone margin. The resulting predicted flow rate patterns at the ambient seabed SWI are unique due to the additional superimposed free boundary surface flexure signature upon the four-quadrant pattern strain lobe signature. Result from slow-slip simulations showed fundementally different patterns are observed dependent on whether the dislocations propagate updip or downdip. The two subpeaks of accelerated fluid outflow though the SWI result from updip migration of the dislocation tip, and double-peaked inflow events occur during downdip migration.

The pattern of the SWI flow rate observed on the frontal prism of the subduction zone at one CAT meter site can almost exactly be reproduced with a dislocation slowly

propagating downdip from a shallow, near-trench, initiation location. The other unique patterns in flow rate time series could similarly be matched, but using different propagating dislocation parameters. Matching the unique hydrologic records at all three instrument locations requires that the slow-slip dislocation simultaneously migrates updip and downdip. The simplest explanation could be that the dislocation intiated sub-parallel to the trench and propogated both updip and downdip under the CAT meters.

In conclusion, even though the shallow subduction zone plate interface has velocity-strengthening hydrous saturated sediments, stable sliding does not occur on the decollement at all times as is commonly believed in the literature. Instead, the shallow plate interface appears to experience coupling, perhaps related to basement topography in the normally faulted incoming crust, which results in stick-slip behavior and episodic slip events. North of the Nicoya peninsula, the Nicaragua subduction zone, with slightly denser normal faulting on the incoming plate, is capable of generating very dangerous tsunamis from episodic slip on the shallow subduction thrust. The importance for our understanding of the faulting mechanisms in shallow regions of subduction faults is clear from the standpoint of hazard assessment and prediction.

Future work

Given this proof of concept that transients in flow rate at the SWI have a unique time series pattern that can indicate the type, sudden or slow, and if slow, the propagation direction, of the causal dislocation, I recommend continued monitoring at the SWI at subduction margins with instrumentation that combines the benefits of the OTIS meter and CAT meter. The relative ease of modeling SWI measurements from

Costa Rica instruments placed on the ambient seabed as opposed to a seep, and the convenience of not having to search on the seafloor for a seep site with sufficient flow rates for the OTIS meter detection limit, calls for development of this OTIS-CAT meter. Another instrument that could be deployed at the SWI for making hydrologic measurements is a pore pressure profiler. Like the future OTIS-CAT meter, a pore pressure profiler also has the potential to capture small changes in volumetric strain coincident with tectonic deformation events at high temporal resolution and accuracy (Tryon, M.D. personal correspondence).

Model predictions of SWI flow patterns resulting from propagating and sudden slip, suggest that future deployments of hydrogeologic instruments at subduction zones would ideally have closer spacing near the trench axis. Interpretation of hydrogeologic transients recorded with flow rate or pore pressure SWI instrumentation requires that future deployments also include an array of offshore seismometers. As explained in the introduction chapter, before advancing to the modeling stage to interpret flow rate transients, it is necessary to first constrain whether hydrologic events are responding to a tectonic event, and whether the tectonic related mechanism for driving flow is volumetric strain or not. This can be accomplished through comparison of hydrogeologic responses and the record of seismic activity. Ideally, the network of seismometers would allow for location and focal mechanism determination of each seismic event in the offshore environment, but the size of data sets, and time involved to accomplish this is too much to ask. Finally, long-term monitoring is necessary to capture a number of events with the suite of offshore instruments and the evolution of these events within the interseismic period of the earthquake cycle. Linking

instrumentation to a seafloor observatory cable providing power from and communication with an onshore station will make this a possible feat. Models used to infer deformation from an single period of hydrogeologic transience may need to be three dimensional to account for along strike differences in dislocation propagation direction, location, and extent. However, considering the abundant data sets recovered with real-time observatory networks, the simplified model that has been completed in this study is crucial for making a first attempt at interpreting each of many potential deformation events.

The chemistry of fluids has occasionally been observed to exhibit changes prior to earthquake events in onshore studies. As a last recommendation, it would be insightful to also record fluid chemistry in these offshore margin environments with high temporal accuracy. Could fluid chemistry indicate a change in permeability of a fault structure with a bridging of microfractures, a phenomenon that Byerlee [1993] proposes could potentially precede rupture along a fault? Although no consistent patterns in chemical precursors have been discovered to date in onshore studies near large strike-slip faults at transform margins, i.e. the San Andreas Fault zone, that does not preclude the possibility that the chemical measurements in the little-studied offshore subduction zone margins have a more repeatable and predictable pattern associated with faulting events.

References

Byerlee, J. (1993), Model for Episodic Flow of High-Pressure Water in Fault Zones before Earthquakes, *Geology*, *21*, 303-306.